PROJECTILE PENETRATION OF THIN ALUMINIUM PLATE

by

GILES CHRISTOPHER PEARSON

Submitted to the University of Cape Town
in fulfilment of the requirements for the
degree of Doctor of Philosophy

May 1978

ACKNOWLEDGEMENTS

This thesis was supported by the Council for Scientific and Industrial Research (C.S.I.R.), Pretoria, Republic of South Africa.

The project was carried out in the Department of Mechanical Engineering, University of Cape Town, under the supervision of Professor R.K. Dutkiewicz and Professor J.B. Martin whose guidance and encouragement is gratefully acknowledged.

The author would also like to thank Mr. W.K. Bettesworth and his workshop staff for their assistance with the construction of the apparatus.

PREFACE

The study of thin plate penetration has long been hampered by the lack of experimental data and that which has been reported is concerned mainly with displacement-time records of the projectile and target responses to impact.

In the present study two new techniques have been developed to monitor the penetration process. The first records a specific particle deceleration in the projectile during penetration from which the forces of impact can be derived and the second records the growth of the projectile-target contact area. Whereas data obtained from the first method can only describe the projectile's response to impact, it is possible by means of the second method to interrelate the projectile and target responses. The combination of these two techniques therefore provides a powerful tool by which thin plate impacts can be studied.

To understand the nature of the experimental results which have been obtained, an empirical model of thin plate penetration has been developed. This analysis is based on the assumption that on impact, the target responds as a thin rigid plastic membrane and has been found to model the penetration process reasonably well for D/H ratios greater than 10.

FRONTISPIECE: A sectional view of a typical thin plate during penetration and the two special projectiles and range of heads which were used to monitor the process

TABLE OF CONTENTS

TABLE OF CONTENTS (continued)

TABLE OF CONTENTS (continued)

NOMENCLATURE

For quick access to the nomenclature a fold-out version in included after the appendices.

E	energy
E_{IZ}	inner zone energy
E_{oz}	outer zone energy
D	projectile diameter
l	projectile length
L	cone height of projectile head
d	sensor distance from projectile tail
X	projectile rigid body transverse displacement
u	projectile particle transverse displacement
x	co-ordinate measured from projectile tail
V_o	projectile striking velocity
V	instantaneous projectile velocity
V_f	projectile post-penetration velocity
V^*	unspecified intermediate velocity where $0 < V^* < V_o$
U	Laplace transform of u
U^*	dummy variable
W	dummy variable
H	undeformed target plate thickness
T	deformed target plate thickness
R	radial location of plastic deformation front

r_o	radial location of inner-outer zone boundary
r_o^*	inner-outer zone boundary radius at which indentation transforms to petalling or conic deformation
r	radial co-ordinate
S	inner zone location parameter measured from the petal tip along the projectile cone surface
S'	radial location corresponding to S
Y	tensile yield stress of target material
ρ	target mass density
C_p	plastic deformation wave velocity
M_r	radial bending moment in target
M_t	tangential bending moment in target
M_o	plastic moment of target
P_o	static punching force of target
N_r	membrane force
F	instantaneous penetration force
F^*	maximum value of the penetration force
X_I	indentation transverse displacement
X_I^*	indentation-conic deformation transformation displacement
X_c	transverse displacement due to conic deformation
X_r	inner zone transverse displacement during petalling
X_s	transverse shear separation displacement
X_ϕ	transverse displacement during the terminal phase of petalling
X_d	outer zone transverse displacement

X_{do}	outer zone transverse displacement at the inner-outer zone boundary
C	constant
K_A	slope of empirical 'A' function
K_I	indentation constant
K_P	petalling constant
A	area
e_{IN}	input voltage
e_{out}	output voltage
B	magnetic field intensity
t	time
K_v	projectile transducer transfer constant
K_d	differentiator transfer constant
K_I'	integrator transfer constant

θ	angle between the deformed and undeformed target
θ_o	plate angle at the inner-outer zone boundary
α	projectile semi-cone angle
μ	coefficient of friction between the target and projectile
λ	complex variable
ε	membrane strain in the generator direction
ε_H	membrane hoop strain
ε_N	membrane normal or thickness strain
σ	membrane stress in the generator direction
σ_p	interfacial compressive stress
σ_p^*	the mean pressure of resistance of the target material

σ_s	shear stress
σ_s^*	target shear stress at which inner zone separation occurs
ϕ	petal rotation in terminal petalling
ω	circular frequency

CHAPTER 1

A SURVEY OF THIN PLATE PENETRATION THEORIES

1.1 INTRODUCTION

The impact of projectiles on thin metallic plates is accompanied by a variety of phenomena, the nature of which is determined primarily by the strength, ductility and hardness of the colliding bodies and the shape and momentum of the projectile. Due to the concentrated type of loading on the target plate, these phenomena fall naturally into two classes, namely those related to the immediate projectile/target contact and those to the propagation of transients beyond this region. For convenience, the regions in which these phenomena occur are termed the Inner and Outer Zones respectively.

Thin plate impacts involving projectiles with a small initial momentum produce no permanent deformation in either the Inner or Outer Zones and responses of this kind have been adequately described using pure elastic theory (1).* For more severe impacts, brittle targets respond by shattering, whereas ductile targets experience a local plastic

* Reference number

deformation in the Inner Zone while responding elastically in the Outer Zone. When more severe impacts occur, ductile plates respond by deforming plastically in both the Inner and Outer Zones and in the limit, Inner Zone failure permits the passage of the projectile through the target. This region of thin plate impact is in itself quite large, extending from the low speed thin plate penetrations, which are the subject of the present thesis, through the ballistic range(2,3,4,5,6,7) and up to the most severe impacts which occur in the hypervelocity range (8)

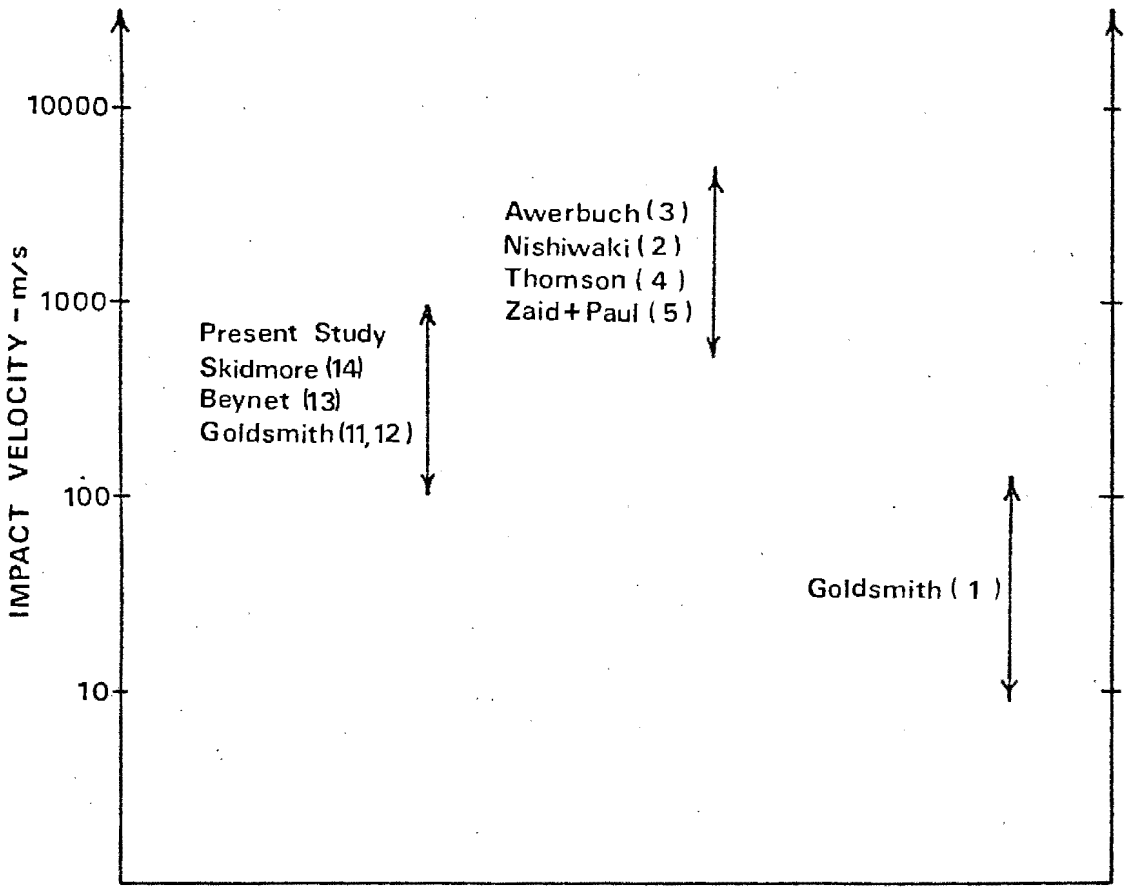

Fig. 1.1 Summary of the relevant penetration theories and their position in the velocity spectrum

The vast spectrum of phenomena encountered in thin plate impact and perforation cannot be encompassed by a single comprehensive analysis. Instead, theories have been formulated to describe specific types of response and are therefore limited to a narrow range of collision conditions. Penetration studies relevant to the present work are summarised in Fig. 1.1 . Although these studies cover a wide range of impact conditions, all have been found to have a bearing on the present work.

Due to the complex nature of thin plate penetration, many simplifying assumptions must be made when describing these processes analytically. The most common assumption made, is with regard to the relative importance of the Inner and Outer Zone responses in a particular impact situation, since a considerable simplification is possible, if one of these can be disregarded. By choosing suitable projectile/target configurations, it is possible to highlight certain aspects of penetration and overlook others. Most work done in the field has adopted this stratagem and the following discussion will deal with Inner and Outer Zone penetration theories separately.

Penetration solutions based on the Inner Zone response are quite different from those attempting to model Outer Zone behavior, the difference being due to the presence of the projectile/target contact stresses in the former.

These stresses generally reach the target material flow stress and the resulting deformation is largely governed by the geometry of the projectile head. Outer Zone deformation on the other hand, is not predetermined in this way, but is governed by the dynamic response of the region to transients passing through it.

1.2 INNER ZONE THEORIES

Several early thin plate penetration theories are based on work done by Taylor (9), who investigated the mechanism of radial hole expansion in thin plastic plates. He found that the energy required to expand a pin-hole to a diameter D, in a plate of thickness H, could be fairly well described by the equation:

$$E = \pi D^2 HY/8 \quad \ldots\ldots\ldots\ldots\ldots\ldots\ldots\ldots \quad 1.1$$

Thomson (4) used this result in conjunction with some dynamic considerations to formulate a projectile penetration theory. His work is based on the assumptions of negligible Outer Zone deformation, a constant projectile velocity during penetration and a sufficiently ductile target material which could undergo the prescribed deformation shown in Fig. 1.2 without cracking.

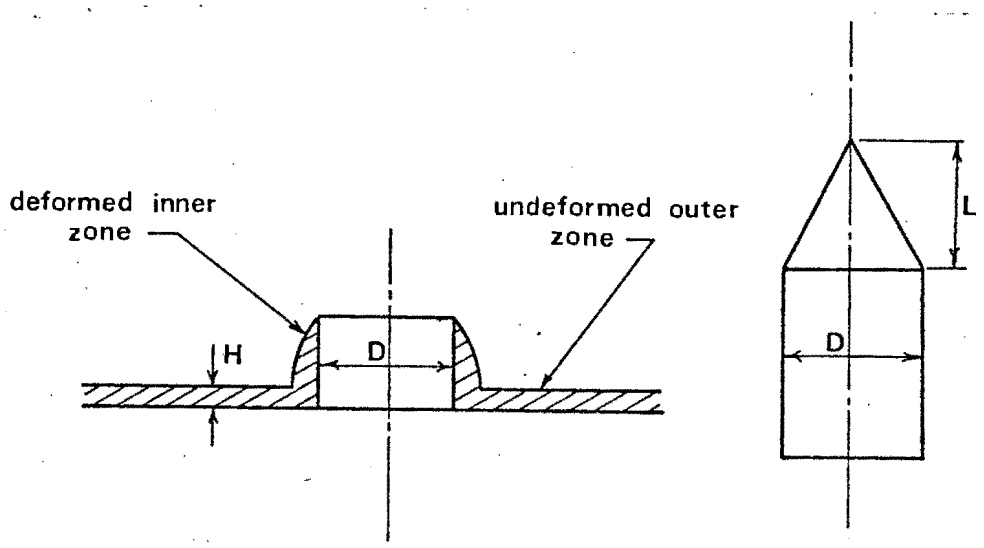

Fig. 1.2 Thomson's deformation model

The projectile energy required to penetrate the target is given by Thomson's theory as:

$$E = \pi D^2 HY/4 \left[Y/2 + \rho(V^* D/2L)^2 \right] \quad \ldots\ldots\ldots \quad 1.2$$

and the force-time history as:

$$F = 4\pi H\rho(V^* \tan\alpha)t \quad \ldots\ldots\ldots\ldots\ldots\ldots \quad 1.3$$

These equations are derived specifically for a cylindro-conical projectile of cone height (L).

* Using Thomson's Inner Zone model with a few minor modifications, Brown (10) extended it by including a specified Outer Zone response. He assumed that the Outer Zone deformed into a conical shape and added an extra term

* This model has been included in the Inner Zone penetration discussion, as it represents a simple extension of Thomson's work.

to the penetration energy equation giving:

$$E = [\pi D^2 HY/8\ (1+2\ \langle K^2-1\rangle\ \log K)]/1-(\pi D^2 H\rho \langle V^*/V_o\rangle^2 /M)[(k+3)(K-1)+12\langle 1+(D/2L)^2\rangle] \quad \ldots\ 1.4$$

where K = 2R/D must be found empirically (see Fig. 1.3)

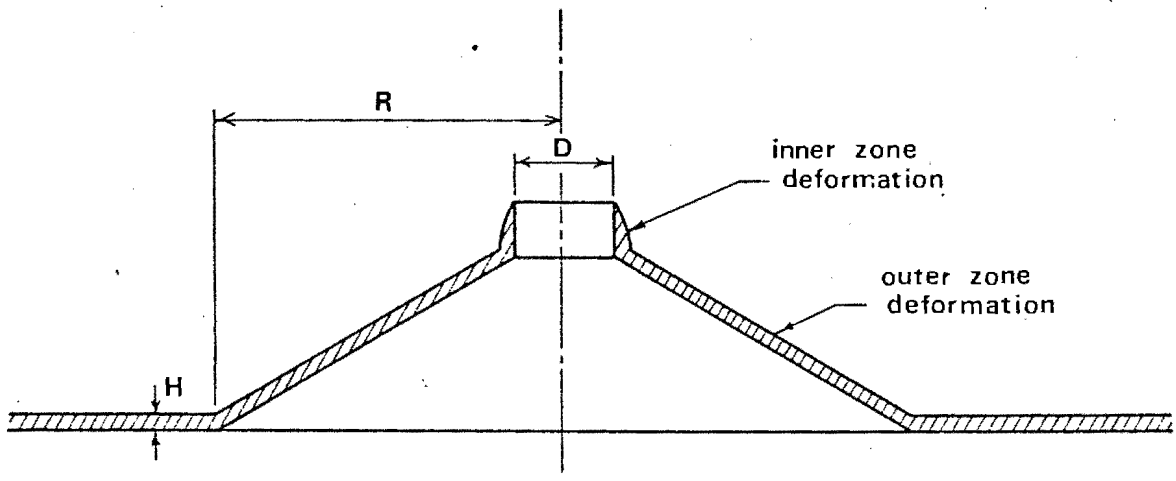

Fig. 1.3 Brown's deformation model

For high speed perforation and when D/H ratios are large, the physical strength of a target becomes of secondary importance and resistance can be assumed to be due entirely to target inertia. Zaid and Paul (5), using this assumption and neglecting Outer Zone response, calculated the velocity drop experienced by a cylindro-conical projectile during high speed perforation as:

$$\Delta V = \pi D^2 H\rho V_o \sin\alpha/4M \quad \ldots\ 1.5$$

and the force-displacement history to be:

$$F = 2\pi\rho H V_o^2 \times \tan^2\alpha \sin\alpha \quad \ldots\ 1.6$$

(where $0<X<L$)

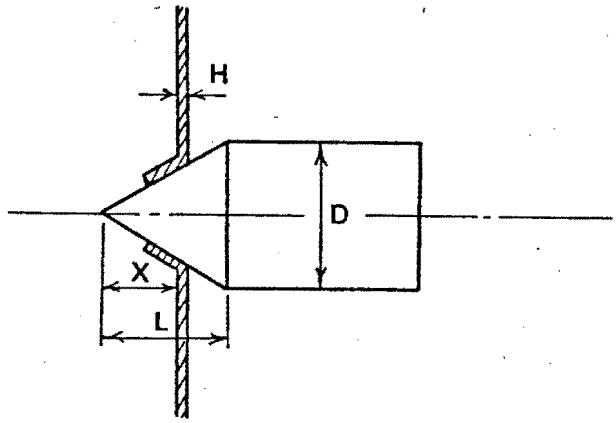

Fig. 1.4 Zaid and Paul's deformation model

Most simple penetration theories disregard the Outer Zone response either by considering high speed perforation conditions, when transients have little time to affect the Outer Zone, or by studying relatively thick plate impacts (ie. small D/H ratios). In this case, the contact forces developed are insufficiently large to cause significant Outer Zone deformation. Impacts of this type have been studied by Nishiwaki (2), Awerbuch and Bodner (3) and Goldsmith and Finnegan (11).

Nishiwaki, using the concept of a static punching force P_o , to represent the target material strength, computed the drop in velocity experienced by a projectile during each of the three stages of penetration shown in Fig. 1.5

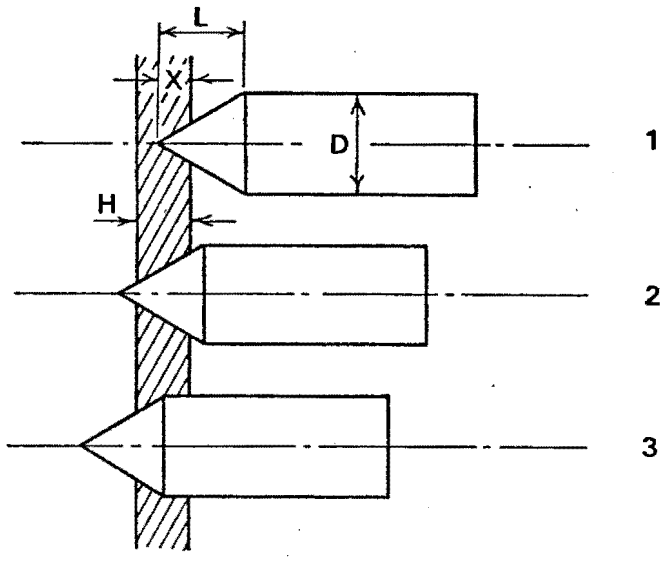

Fig. 1.5 Nishiwaki's deformation model

The final velocity of the projectile at the end of the third stage (V_1) was found to be given by the equation:

$$V_1^2 = e^k[(V_o^2 - P_o/\rho Sin^2\alpha)(e^k - 1)] \quad \ldots\ldots\ldots\ldots 1.7$$

and the force-displacement history by:

$$F = -\pi X^2 \tan^2\alpha [P_o + \rho V_o^2 \, Sin^2\alpha] e^{-\kappa x^3} \quad \ldots\ldots\ldots\ldots 1.8$$

where

$$K = \pi D^2 H \rho Sin^2\alpha / 2M \text{ and } 0 < X < L$$

In the penetration model developed by Awerbuch, Bodner, Goldsmith and Finnegan, penetration is effected by shearing a plug from the target plate, rather than by displacing target material radially, as envisaged by the Nishiwaki model.

The penetration in this case is also considered in

three stages, as shown in Fig. 1.6

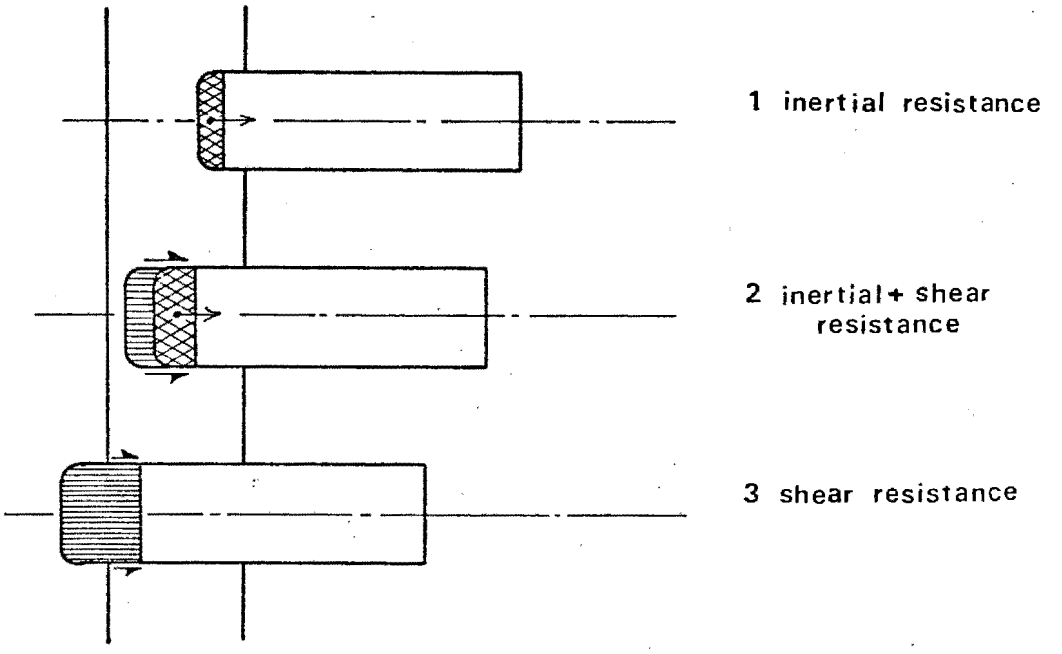

Fig. 1.6 Awerbuch's deformation model

During the first stage, target resistance is assumed to be due only to the compressive contact stress and Inner Zone inertia effects. As the penetration proceeds into the second stage, an additional shear stress develops in the plug of target material ahead of the projectile. The second stage is terminated when the plug formation reaches the distal surface of the target plate and in the final stage, resistance is due only to the shear stress. Unlike the theory due to Nishiwaki, the three stages must be considered separately and the overall theory

cannot be represented by a single relationship.

1.3 OUTER ZONE THEORIES

When severe Outer Zone deformations occur during a penetration, the energy associated with this process cannot be neglected, as was the case in the previous section. In the following theories, Inner Zone deformation is generally overlooked and the Outer Zone response is assumed to account for all the penetration energy.

The simplest conceivable Outer Zone deformation pattern is that of a cone and as previously mentioned, was suggested by Brown (10). The energy associated with this deformation is given as:

$$E = \pi HY \left[R^2 - (D/2)^2\right] \ln(\mathrm{Sec}\theta) \quad \ldots\ldots\ldots\ldots\ldots\ldots \quad 1.9$$

Refining this approach, Calder (12) assumed a more realistic target profile described by the empirical relationship:

$$X_d / X_{do} = e^{-r} \quad \ldots\ldots\ldots\ldots\ldots\ldots\ldots\ldots\ldots\ldots \quad 1.10$$

and by including work hardening effects predicted the penetration energy to be:

$$E = \left[\pi \beta H / 64(1-\nu+\nu^2)^{\frac{1}{2}}\right]\left[X_{do}^4 + 16\sigma_y X_{do}^2 / \beta\right] \quad \ldots\ldots\ldots \quad 1.11$$

where

β = linear work hardening parameter

σ_y = initial yield stress

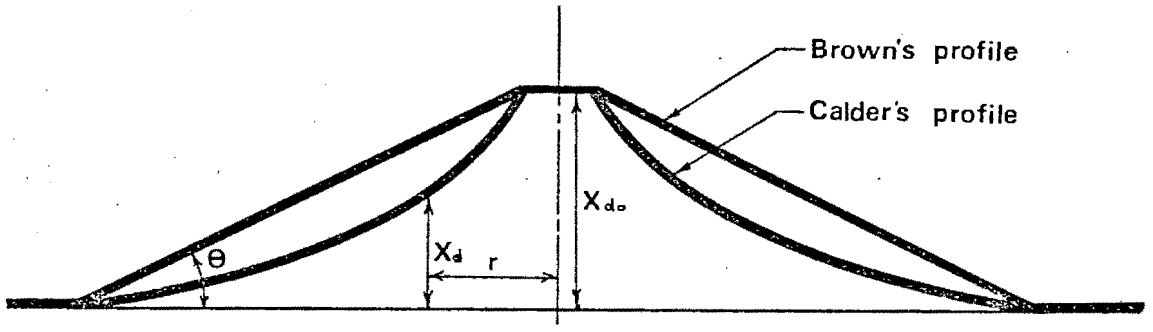

Fig. 1.7 Brown and Calder's Outer Zone deformation patterns

To determine Outer Zone profiles analytically, it is necessary to consider the dynamic response of the Outer Zone, the governing relationships usually taking the form of partial differential equations. In their general form these equations are usually insoluble, but by neglecting certain terms and choosing suitable boundary conditions, solutions have been found.

Beynet, Plunkett (13), Latheby and Skidmore (14) investigated the impact of flat ended projectiles with

thin target plates, since this shape of projectile head requires no Inner Zone analysis and provides simple boundary conditions for the Outer Zone solution. As radial plate motion is negligibly small, Outer Zone response can be well approximated by the transverse dynamic equation of axis-symmetric motion, given by (15) as:

$$\rho H \frac{\partial^2 X_d}{\partial t^2} = \frac{1}{r} \frac{\partial}{\partial r} \left[M_r + \frac{\partial M_r}{\partial r} r - M_t + r N_r \frac{\partial X_d}{\partial r} \right] \quad \ldots\ldots\ldots\ldots \quad 1.12$$

By neglecting the bending moment contribution and assuming a pure plastic memebrane response, this equation reduces to:

$$\rho H \frac{\partial^2 X_d}{\partial t^2} = \frac{1}{r} \frac{\partial}{\partial r} \left[r N_r \frac{\partial X_d}{\partial r} \right] \quad \ldots\ldots\ldots\ldots\ldots\ldots\ldots\ldots \quad 1.13$$

which can be solved numerically to determine target plate profiles as a function of time.

Instead of limiting the solution to purely transverse motion, Craggs (16), assuming constant velocity penetration, used the kinematic relation:

$$\frac{D\theta}{Dt} = - \cos\theta \left[\frac{\partial v_t}{\partial r} \cos\theta + \frac{\partial u_t}{\partial r} \sin\theta \right] \quad \ldots\ldots\ldots\ldots\ldots \quad 1.14$$

(where u_t and v_t are the transverse and radial velocity components respectively) to describe the mode of deformation and together with dynamic equations, discussed various types

of cylindro-conical impact. Unfortunately the numerical solution required of this method is not carried out and predicted Outer Zone responses are not presented.

By assuming membrane stresses to be of secondary importance, Calder, Kelly and Goldsmith (17) used purely bending moment-curvature relationships to describe Outer Zone equilibrium. Their governing equation for a visco-plastic plate is given as:

$$\nabla^4 V + \left[3\sqrt{3}\gamma\rho/2HM_o\right] \frac{\partial V}{\partial t} = 0 \quad \ldots\ldots\ldots\ldots\ldots\ldots \quad 1.14$$

which can be solved in the Laplace transform space. Inversion of this solution is accomplished analytically for the singular point at the plate centre giving its velocity-time history as:

$$V = \left[V_o - P/Mb^2\right] e^{b^2 t} \operatorname{erfc}\left(bt^{\frac{1}{2}}\right) + P/Mb^2\left[1 - 2b\,(t/\pi)^{\frac{1}{2}}\right] \quad \ldots\ldots\ldots \quad 1.15$$

(where M_o is the plastic moment,

$P = 4\pi M_o/\sqrt{3}$, $b = 16\rho/\delta^2 M$ and $\delta^4 = 3\sqrt{3}\gamma\rho/2HM_o$)

but numerical methods must be used for the remainder of the Outer Zone region. For strain rate sensitive materials, predicted permanent plate deflections are in good agreement with experimental results, but poor agreement is obtained for strain rate insensitive materials, such as aluminium. Discrepancies are assumed to be due to the neglect of membrane effects.

1.4 SUMMARY

The literature survey presented is not exhaustive, but gives an idea of the types of theory which have been proposed to describe thin plate penetration. It is evident from this survey that the complex nature of the problem requires the use of many simplifying assumptions, which are often unrealistic and limit the applicability of a particular theory to a narrow range of impact velocities and projectile/target configurations. Thin plate impact must necessarily involve both the Inner and Outer Zones to a greater or lesser extent and the theories revised in this chapter, which neglect the response of either one of these zones, must be regarded as limiting cases of the general impact condition.

It is evident from the literature survey that a broader approach to the problem of thin plate penetration must be developed, if a more realistic penetration model is to be constructed. This is the object of the present research. To gain insight into the Inner and Outer Zone mechanisms and an understanding of their inter-relationships, an experimental technique was developed to monitor force-time histories during penetration and with the aid of this data, it has been possible to analyse the penetration process more closely.

The study has been carried out on a range of cylindro-

conical projectiles (of varying cone angle) which produce a variety of Inner Zone responses and by investigating the limiting case of penetration, namely containment, these Inner Zone responses occur in conjunction with the most severe Outer Zone deformations. The impacts investigated are therefore not specifically Inner Zone or Outer Zone situations, but rather cover the spectrum of impact conditions, which to date has received little attention.

CHAPTER 2

AN EMPIRICAL APPROACH TO THIN PLATE PENETRATION

2.1 INTRODUCTION

Most penetration studies are concerned with the response of either the target or the projectile. The present study however requires a knowledge of both responses. From an energy point of view only the target response is of interest, since the projectile's elastic response is essentially conservative. The importance of projectile elastic behavior stems from the experimental technique used to record projectile particle motion during impact. To be able to predict the overall projectile response, the elastic behavior of the projectile must be analysed. Before projectile and target responses can be inter-related therefore, each must be analysed separately. The present chapter describes the form of these analyses and detailed accounts of the target and projectile models are presented in Chap. 3 and Chap. 4.

2.2 TARGET ANALYSIS

Thin plate penetration essentially involves the conversion of projectile kinetic energy into target de-

deformations and the description and understanding of this process is the object of the target analysis. The analysis has been approached from the point of view of an ideal 'rigid' projectile being subjected to a decelerating force at its interface with the target. If this contact force (F) and the projectile displacement (X) can be predicted as a function of time, then these variables are related by the energy expression:

$$E = \int F dX \qquad \ldots\ldots\ldots\ldots\ldots\ldots\ldots\ldots \quad 2.1$$

To model penetration, equation 2.1 is incorporated in a forward integration technique which for each time increment requires a knowledge of both F and X. If the projectile can be assumed to behave as a 'rigid' body, this force and displacement are determined solely by the target's response to impact and the projectile's original momentum. Fig. 2.1 shows a typical target profile at some stage during penetration.

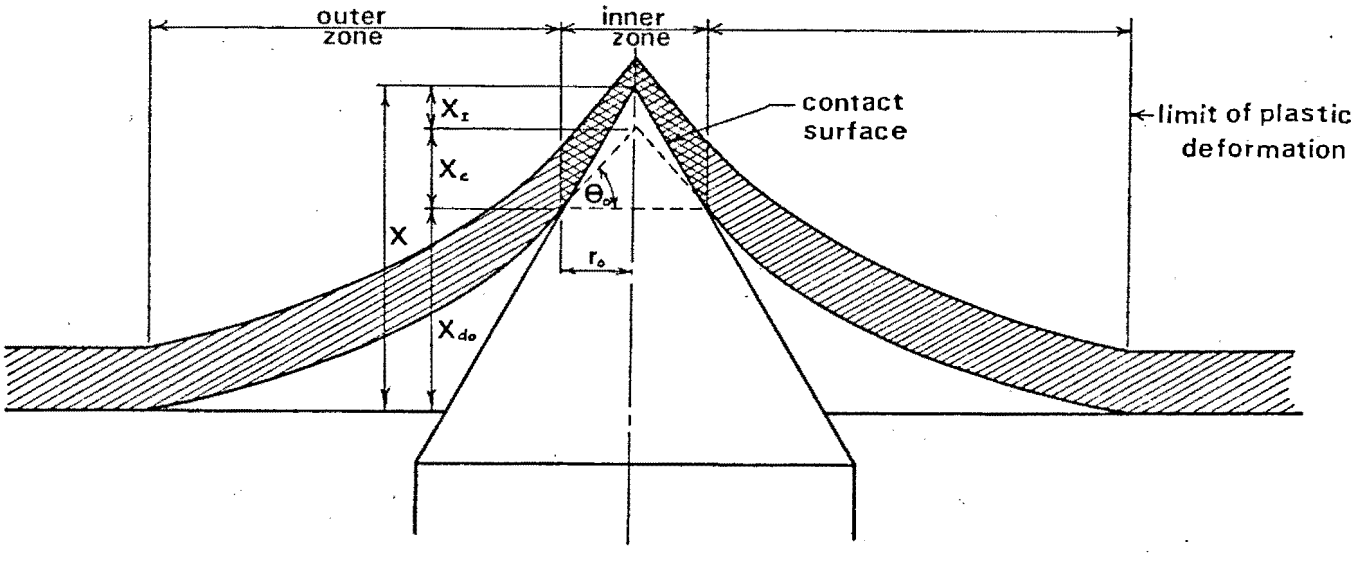

Fig. 2.1 A typical deformed target profile

The previously defined Inner and Outer Zones are clearly shown in this diagram. They are separated by a cylindrical surface drawn concentric with the projectile's axis and of a radius equal to that of the current contact area. Due to the presence of the contact stress in the Inner Zone, the deformation pattern in this region is completely different from that in the Outer Zone and two separate sub-analyses are carried out to determine the behavior of each zone. From these analyses, it is possible to deduce values for the various transverse plate displacements (X_I, X_c, X_{do}) and the penetration resisting force (F) for each time increment. Since there is no direct relationship between these displacements, a trial and error solution is used (involving common parameters) until the expression

$$X = X_c + X_I + X_{do} \quad \ldots\ldots\ldots\ldots\ldots\ldots\ldots \quad 2.2$$

is satisfied. If the procedure is carried out for each time increment in the penetration, a force-displacement history can be established, which then leads to a knowledge of the penetration energy distribution through the use of equation 2.1 . The flow diagram for this procedure is shown in Fig. 2.2

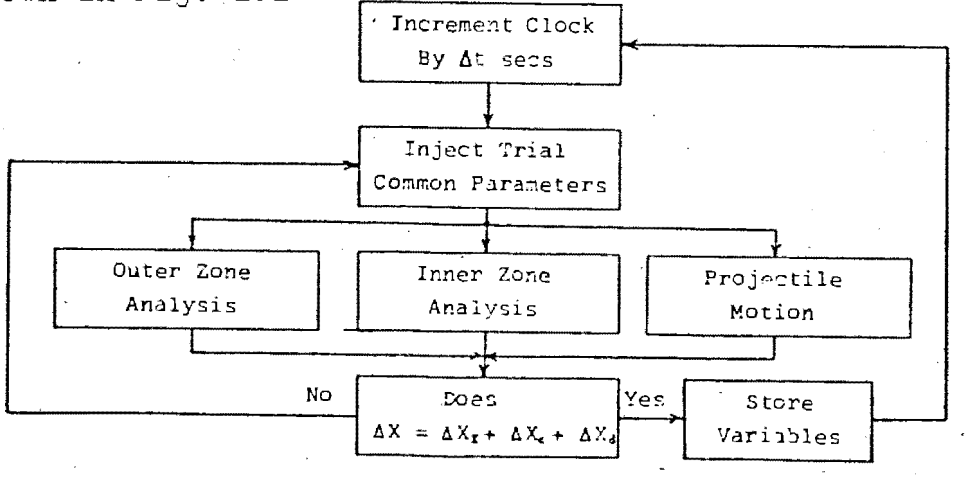

Fig. 2.2 Overall flow diagram for target solution

The "common parameters" previously referred to, which relate the Inner and Outer Zone analyses are actually r_o , the Inner-Outer Zone boundary location and θ_o , the plate slope at this boundary. The transverse plate displacements (X_c, X_I, X_{do}) as well as the penetration force (F) can all be expressed in terms of these two variables and when the correct values of r_o and θ_o are found, equation 2.2 will be satisfied. The penetration problem is thus reduced to finding the correct values of r_o and θ_o for each time increment.

Although the Inner and Outer Zone responses are analysed separately, the method used in each sub-analysis is basically the same. This method centres around the establishment of a representative mode of deformation for each region. Once this is known, the deformed plate profile, plastic strain and local deformation (such as plate thinning) can also be found. This information is sufficient to derive the required parameters (F and X).

A solution of this type is only possible through the use of a high speed computer. The entire analysis was written in Fortran V code and run on a UNIVAC computer.

2.3 PROJECTILE ANALYSIS

The experimentally derived force-time histories of penetration which play a central role in this thesis, can-

not be obtained directly. The system developed to monitor projectile motion, actually records a particular particle acceleration during impact and the projectile's elastic response must be analysed to derive force-time histories from this data.

A typical recorded trace of particle acceleration at a particular location in the projectile is shown diagrammatically in Fig. 2.3

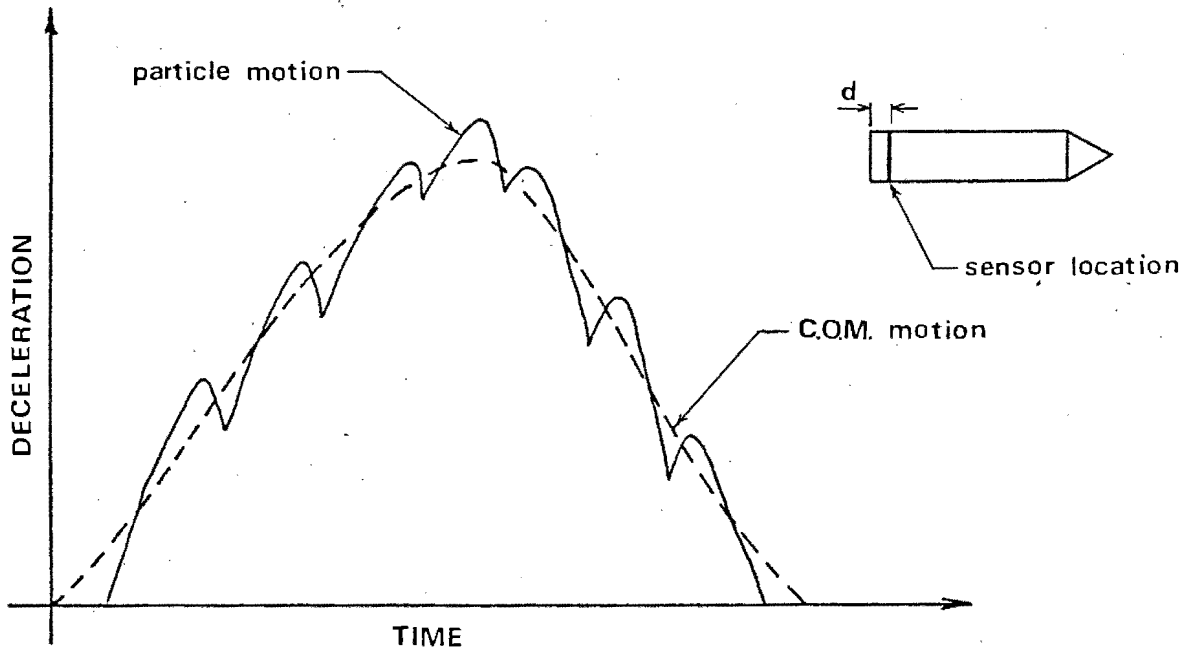

Fig. 2.3 A typical trace of a projectile particle acceleration on impact

Particle motion in the projectile can be considered to be composed of two superimposed motions, ie. a bulk motion, which is common to all particles and a local motion

due to the elastic stress wave phenomenon. Bulk motion can also be regarded as the motion of the projectile's centre of mass, or as the equivalent rigid body response to impact. The projectile analysis enables these two superimposed motions to be separated, so that from the combined acceleration at a particular location in the projectile, the acceleration of the centre of mass ($\ddot{X}_{cm}$) may be deduced. Once this is known, the resisting force (F) acting on the projectile nose, can be found from the relation:

$$F = M\ddot{X}_{cm} \quad \ldots\ldots\ldots\ldots\ldots\ldots\ldots\ldots \quad 2.3$$

This procedure is an extension of a method developed by Masket and Irwin (18). Whereas these researchers were concerned with particle motion in the tail surface of a projectile, the present analysis generalises their result so that particle motion at any location in the projectile can be related to the motion of the centre of mass.

2.4 THE OVERALL ANALYSIS

The inter-relationship of the various sub-analyses is shown in Fig. 2.4. Whereas the projectile analysis is a straight-forward elastic stress wave problem, the target analysis deals with a wide range of diverse pheno-

mena and is considered in a number of separate sub-analyses.

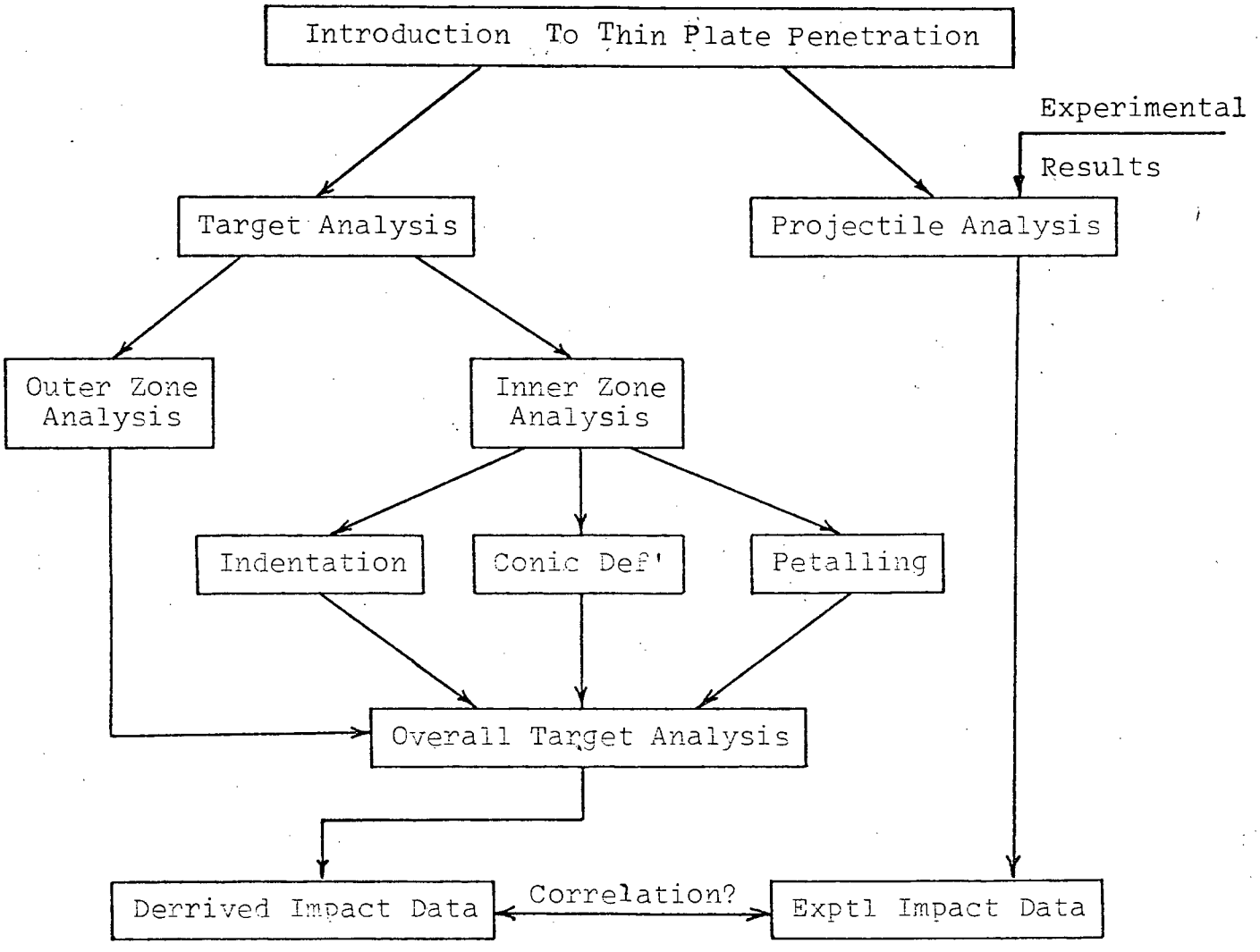

Fig. 2.4 Format of the overall penetration analysis

CHAPTER 3

TARGET ANALYSIS

3.1 THE OUTER ZONE MODEL

In the present work, Outer Zone deformations are extremely large, with central deflections being of the order of ten times the plate thickness. Under these conditions the elastic contribution to transverse plate displacement is negligibly small and Outer Zone response has been described solely by a thin rigid plastic membrane model. The type of deformation under consideration is shown in Fig. 3.1.

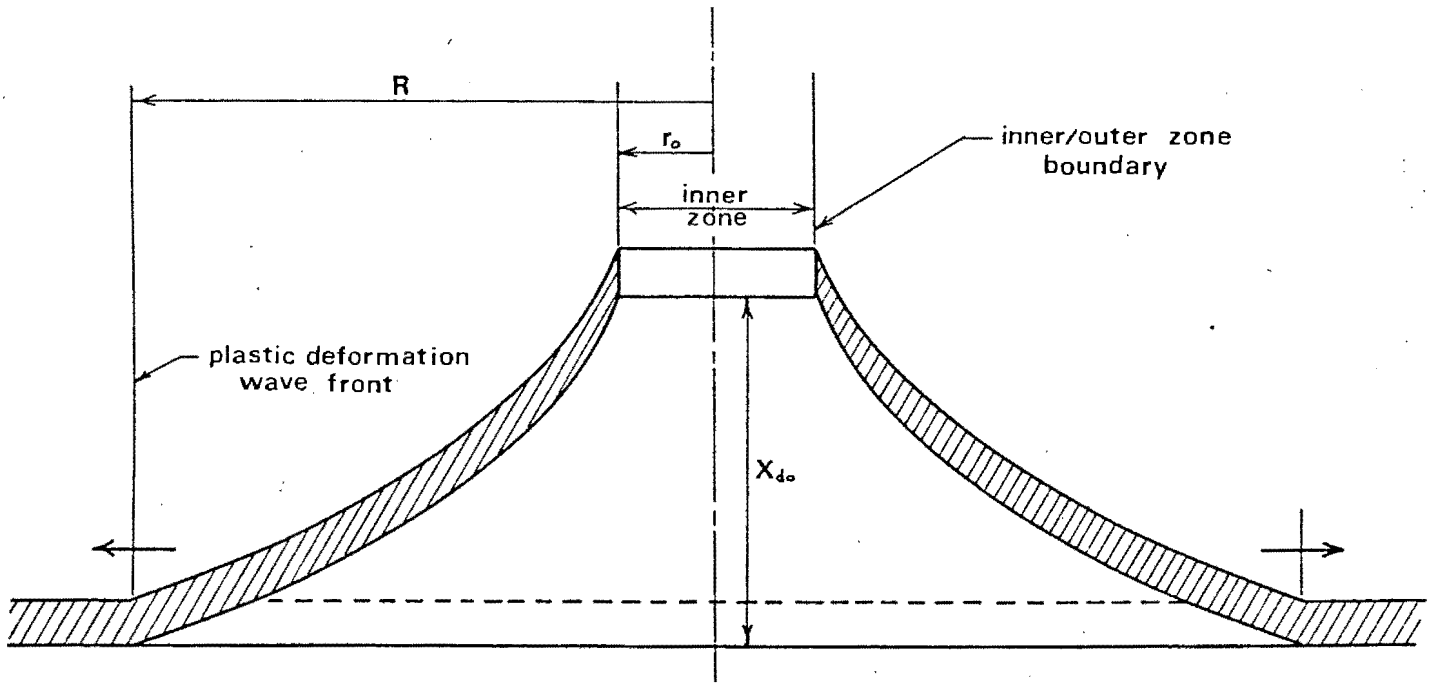

Fig. 3.1 Outer Zone deformation pattern

An approximate equation of motion for this region of the target can be derived from the general dynamic equation for transverse motion of thin plates, which was discussed in Chap. 1 and for simple boundary conditions several numerical solutions have been found to this equation. In the present study however, the Inner-Outer boundary conditions are complex and directly related to the failure mechanisms in the Inner Zone. For this reason a different approach to the problem was adopted.

The relevant features of the Outer Zone deformation are shown in Fig. 3.1. They are:

(1) An outer limit to the Outer Zone defined by a plastic wave front which has been found to propagate radially at a near constant velocity (C_p) (1) (13) given by:

$$C_p = \sqrt{Y/\rho} \quad \ldots\ldots\ldots\ldots\ldots\ldots\ldots \quad 3.1$$

(2) An inner limit to the Outer Zone (the Inner-Outer Zone boundary at r_o) which also expands radially during penetration up to a maximum value of $r_o = D/2$.

(3) A characteristically shaped region of target material lying between these two limits.

A description of these three features is sufficient to locate the Inner-Outer Zone boundary in the transverse direction (X_{do}) at any time during the penetration. This is the main object of the Outer Zone analysis.

If a plastic deformation wave of constant radial velocity is assumed, then the outer limit location (R) at time (t) is simply given by:

$$R = C_p t \quad \ldots\ldots\ldots\ldots\ldots\ldots\ldots\ldots \quad 3.2$$

Locating the radial position of the inner limit is a more complex problem and involves the overall analysis described in Sect. 2.2. This analysis simultaneously takes into account the responses of the Inner Zone, Outer Zone and projectile. If the inner limit can be located in this manner it only remains to define the curved target plate profile between the inner and outer limits. An approximate shape function for the region can be found as follows.

Equation 1.13 was derived for thin plates undergoing a purely transverse deformation. This model is a good approximation of the actual process since radial deformations have been found (12) (19) to account for as little as 5% of the total deformation. Fig. 3.2 shows a typical annular element in the Outer Zone undergoing a purely transverse displacement.

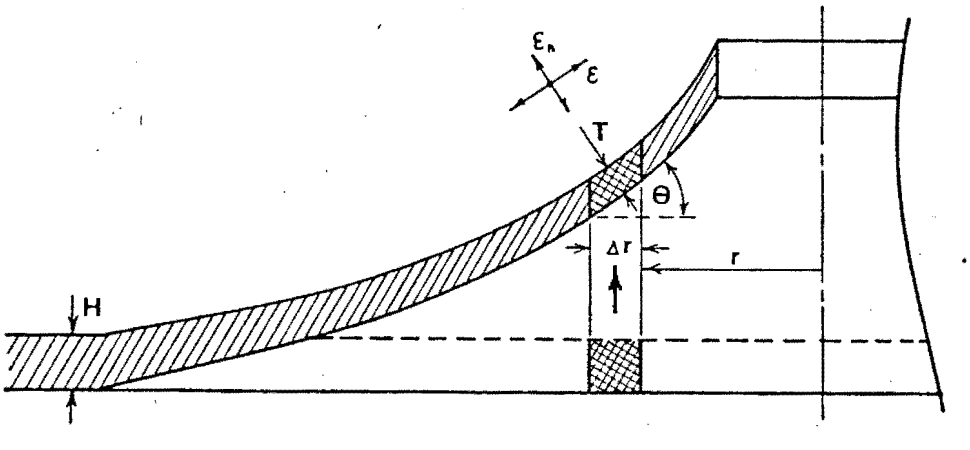

Fig. 3.2 Strain and deformation in the Outer Zone

If the plastic deformation that occurs, can be considered to take place at constant volume (20), then the effective target thickness (T) at a radial location (r) is given by:

$$H\Delta r = T\,\Delta r / \mathrm{Cos}\theta \quad \ldots\ldots\ldots\ldots\ldots\ldots\ldots\ldots \quad 3.3$$

or $$T = H\mathrm{Cos}\theta \quad \ldots\ldots\ldots\ldots\ldots\ldots\ldots\ldots \quad 3.4$$

Since radial deformation is neglected, strain in the Outer Zone is only in the membrane and thickness directions. In terms of the natural principle Outer Zone strains, the deformation at constant volume condition can be written as:

$$\epsilon + \epsilon_N + \overset{o}{\epsilon_H} = 0 \quad \ldots\ldots\ldots\ldots\ldots\ldots\ldots\ldots \quad 3.5$$

and expressing these in terms of the plate slope θ gives:

$$\epsilon_N = \ln(\mathrm{Cos}\theta) \quad \ldots\ldots\ldots\ldots\ldots\ldots\ldots\ldots \quad 3.6$$

$$\epsilon = \ln(\mathrm{Sec}\theta) \quad \ldots\ldots\ldots\ldots\ldots\ldots\ldots\ldots \quad 3.7$$

These expressions will be used later to calculate Outer Zone deformation energy.

With a knowledge of the mode of Outer Zone deformation it is now possible to determine a profile shape function by considering the forces acting on the region. These are shown in Fig. 3.3

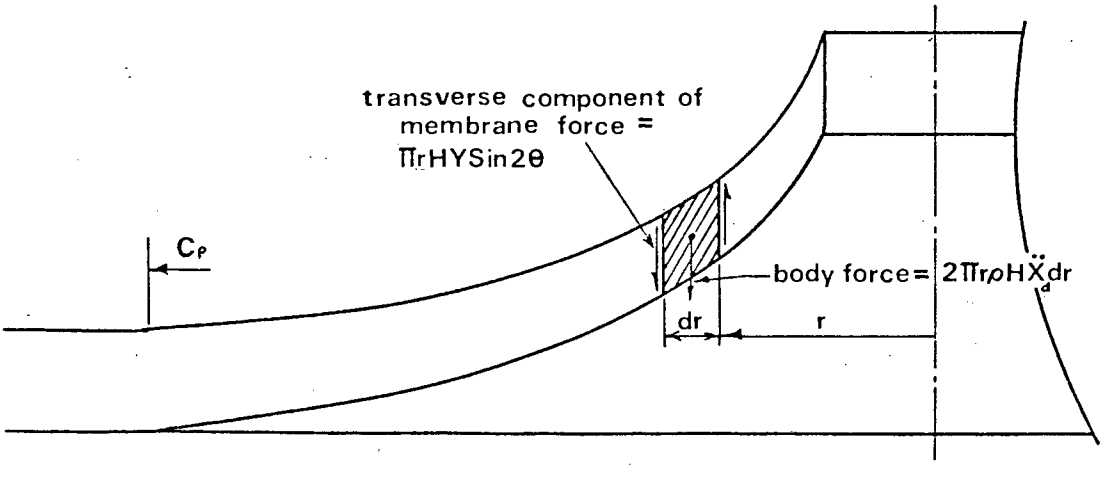

Fig. 3.3 Forces acting on the Outer Zone

The transverse dynamic equation for these forces is

$$2\pi r dr \rho H \ddot{x} = \pi r H Y \sin 2\theta - \pi H Y (r+dr) \sin 2(\theta+d\theta) \quad \ldots\ldots\ldots\ldots 3.8$$

which reduces to:

$$\frac{\rho H}{Y} \frac{\partial^2 X_d}{\partial t^2} = \frac{1}{r} \frac{\partial}{\partial r} \left[(r/2) \sin 2\theta \right] \quad \ldots\ldots\ldots\ldots\ldots\ldots 3.9$$

This equation differs from equation 1.13 only in its description of plate slope and thickness.

In the present work an approximate shape function is derived from this equation by neglecting the contribution of the body force. This is not a serious ommission in the present context since target density is low and impacts occur at relatively low velocities. Equation 3.9 therefore reduces to:

$$\frac{\partial}{\partial r} \left[(r/2) \sin 2\theta \right] = 0 \quad \ldots\ldots\ldots\ldots\ldots\ldots 3.10$$

and integrating this expression with respect to r and approximating the term $\frac{1}{2}\sin 2\theta$ by simply θ gives:

$$r\theta = C \quad \ldots\ldots\ldots\ldots\ldots\ldots 3.11$$

This shape function actually describes a quasi-static membrane response between the prescribed limits and has been found to approximate the actual deformation reasonably well. (Note that a true quasi-static response would not be limited by plastic wave behavior). Equation 3.11 can be written in terms of the boundary parameters r_o and θ_o

simply as:

$$r\theta = r_o \theta_o \quad \ldots\ldots\ldots\ldots\ldots\ldots\ldots\ldots \quad 3.12$$

With a knowledge of the inner and outer limits of the Outer Zone as well as a description of the plate profile between these limits, it is now possible to locate the transverse position of the Inner-Outer Zone boundary (X_{do}) at any time during the penetration. In general, transverse displacements in the Outer Zone (X_d) are given by:

$$X_d = \int_r^R \theta dr \quad \ldots\ldots\ldots\ldots\ldots\ldots\ldots\ldots \quad 3.13$$

and by using equation 3.12 to express θ in terms of the boundary parameters, equation 3.13 becomes:

$$X_d = \int_r^R (r_o \theta_o / r) dr \quad \ldots\ldots\ldots\ldots\ldots\ldots \quad 3.14$$

which evaluated at the Inner-Outer Zone boundary gives:

$$X_{do} = r_o \theta_o \ln(R/r_o) \quad \ldots\ldots\ldots\ldots\ldots\ldots \quad 3.15$$

In addition to this the transverse component of the membrane force at the Inner-Outer Zone boundary must equal the penetration force at any time during the penetration (if Inner Zone body forces are neglected). Thus:

$$F = 2\pi r_o T Y \sin\theta_o \quad \ldots\ldots\ldots\ldots\ldots\ldots \quad 3.16$$

and expressing the deformed plate thickness T in terms of equation 3.4 gives:

$$F = \pi r_o H Y \sin 2\theta_o \quad \ldots\ldots\ldots\ldots\ldots\ldots \quad 3.17$$

As a means of cross-checking energy balances it has proved instructive to calculate Outer Zone deformation

energies as the penetration proceeds. This can be done as follows:

If a body undergoes a natural plastic strain ϵ at a constant yield stress Y, then the energy required to produce this deformation per unit volume of material is given by:

$$dE = Y\epsilon \quad \ldots\ldots\ldots\ldots\ldots\ldots\ldots\ldots \quad 3.18$$

Since membrane strain in the Outer Zone is given by equation 3.7 as

$$\epsilon = \ln(\mathrm{Sec}\Theta) \quad \ldots\ldots\ldots\ldots\ldots\ldots \quad 3.7$$

which in terms of the boundary parameters r_o and Θ_o can be written as:

$$\epsilon = \ln[\mathrm{Sec}(r_o\Theta_o/r)] \quad \ldots\ldots\ldots\ldots\ldots \quad 3.19$$

equation 3.17 can be evaluated for the entire Outer Zone region by integrating over its volume. Thus:

$$E_{oz} = 2\pi HY \int_{r_o}^{R} r \ln [\mathrm{Sec}(r_o\Theta_o/r)]dr \quad \ldots\ldots \quad 3.20$$

Once r_o and Θ_o have been determined at a particular time during the penetration, the Outer Zone deformation energy can therefore be found by solving equation 3.19 numerically.

3.2 INNER ZONE MODELS

3.2.1 INTRODUCTION

The Inner Zone is defined as the target material lying

within a cylindrical surface drawn concentric with the projectile axis and of a radius equal to the current projectile/target contact area. The main feature which distinguishes Inner Zone behavior from that in the Outer Zone is the presence of the interfacial contact stress in the former. This stress is the origin of the entire plate deformation and the present section deals with its distribution and effect in the immediate target vicinity.

The most important parameter determining Inner Zone response, is the shape of the impacting projectile head. (In the present study, shape is simply defined by the semi-cone angle α). Sharp projectiles (small α) pierce the target material easily and penetrate by what is termed the petalling process. This process is characterised by radial cracks in the Inner Zone material, which give rise to petal formation. Blunter or more obtuse projectiles (large α) are not sufficiently pointed to pierce the target plate and a completely different kind of penetration results. Here the Inner Zone material is plastically deformed over the projectile's conical head, in what is termed the conic deformation process. The fundamental difference between petalling and conic deformation lies in the radial crack formation in the former and because of this, the two penetration modes are considered separately in the following analysis.

A third mode of penetration, namely indentation, also

plays an important role in the dynamics of the Inner Zone. Due to the pointed nature of the projectile tip, the initial interfacial contact stress is exceedingly high, resulting in plastic flow of the target material. This indentation is common to the early stages of both the petalling and conic deformation modes of penetration. As the penetration proceeds through the indentation phase, obtuse projectiles are able to relieve the high plastic flow stress, so that indentation ceases. This leads to the conic deformation mode of penetration. If however the projectile is too acute to relieve the flow stress, it will continue to indent until the distal surface of the target is reached. Once this has happened, penetration in the petalling mode will follow. An analysis of the indentation phase is therefore able to predict which mode of penetration will take place. The three principle modes of Inner Zone response are diagramatically shown in Fig. 3.5 and each will be dealt with separately in the following sections.

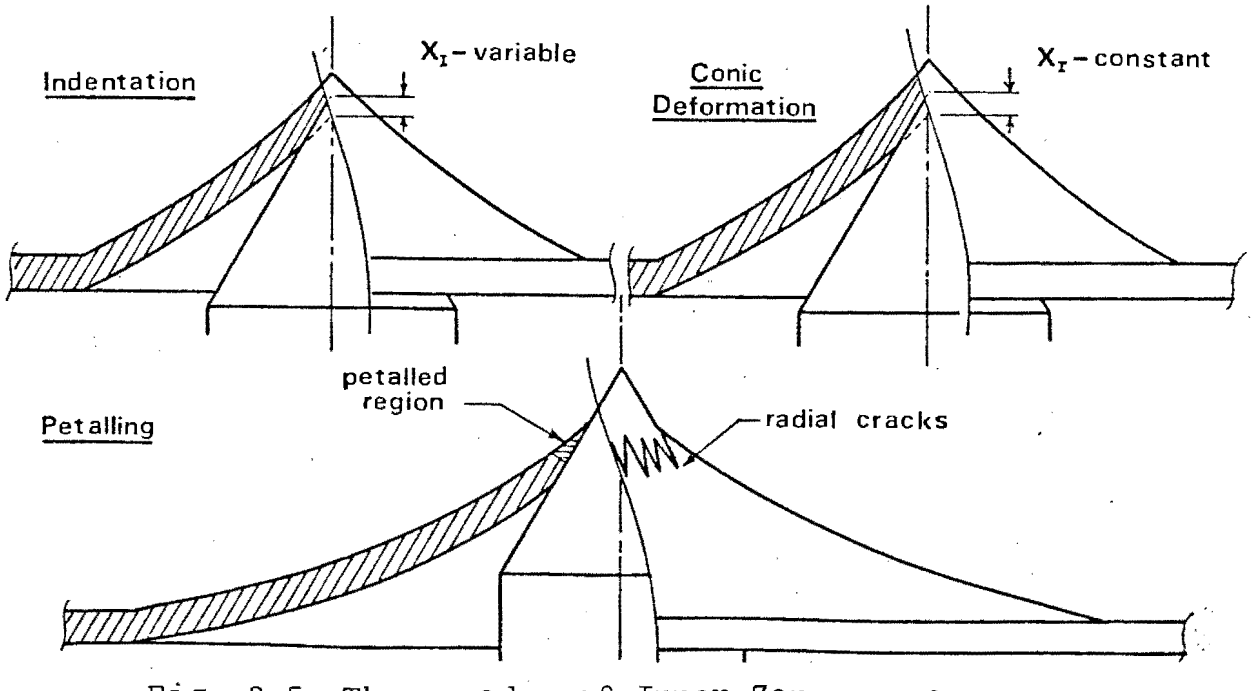

Fig. 3.5 Three modes of Inner Zone response

Whereas the Outer Zone analysis provides a knowledge of lateral motion of the Inner-Outer Zone boundary (X_{do}), as well as the penetration force for each time increment in the penetration, the Inner Zone analysis must describe lateral projectile motion relative to the Inner-Outer Zone boundary (X_I X_c X_r)and also provide a relationship between the boundary parameters r_o and θ_o which is necessary for the trial and error procedure used in the overall solution.

3.2.2 INDENTATION

During indentation and conic deformation, the target material remains physically continuous over the point of impact. The Inner Zone deformation pattern during this type of penetration is therefore considered to be similar to the Outer Zone deformation pattern, with modifications being introduced by the projectile/target contact stress. Fig. 3.6 illustrates this idea and shows the Inner Zone profile as a linear extension of the Outer Zone with a superimposed deformation due to the projectile indentation. An exact description of Inner Zone strain and local deformation is not necessary to describe its response to impact. Since the relevant stresses in this region act over the contact surface and the Inner-Outer Zone boundary surface, a description of these surfaces and the stresses acting on them is sufficient to yield a solution.

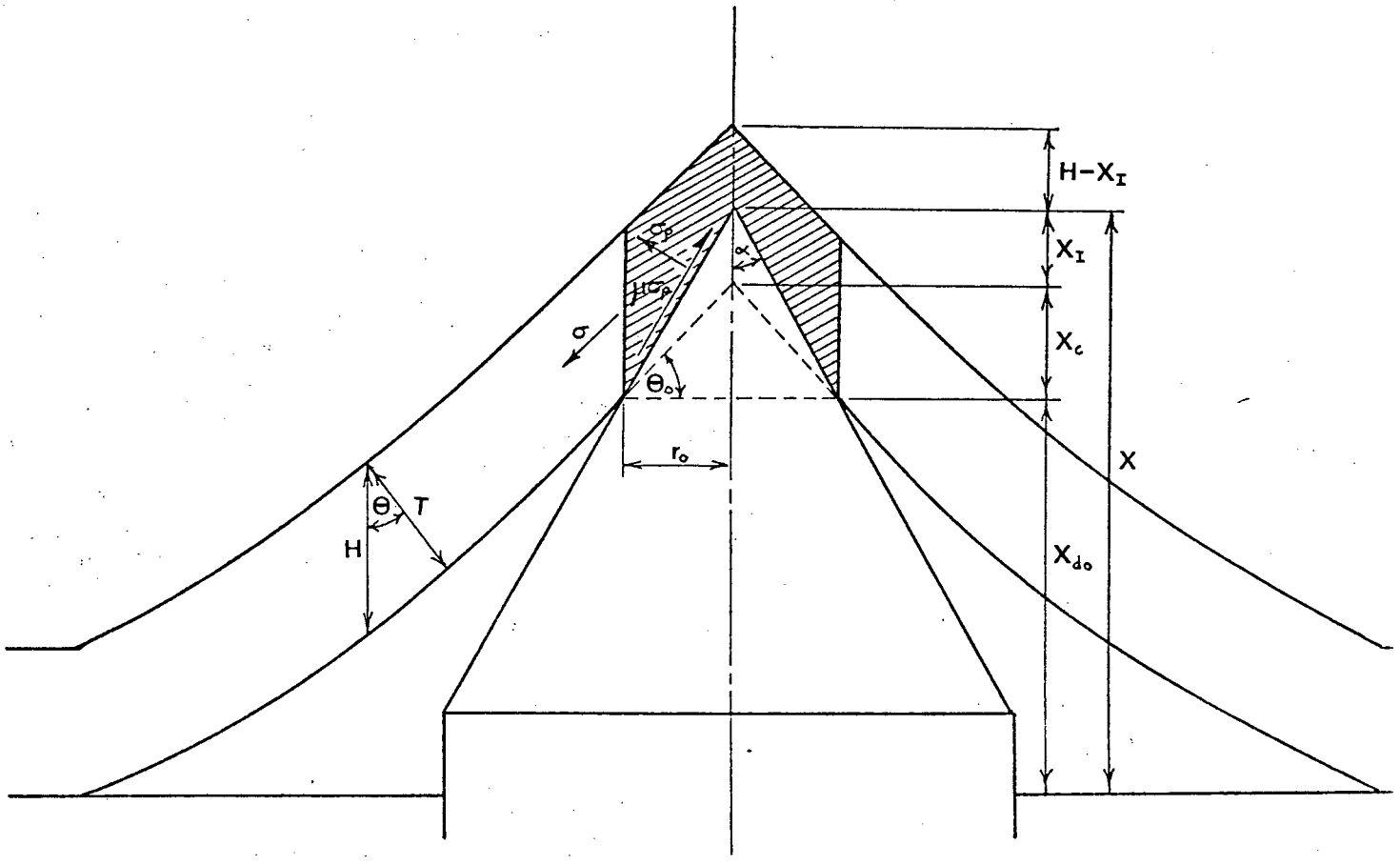

Fig. 3.6 The indentation deformation pattern

Projectile displacement in the Inner Zone is described by two separate mechanisms namely, X_I - the indentation displacement and X_c - the conic deformation displacement. X_I is the true indentation due to flow of the target material and X_c can be regarded as an apparent indentation due to the plate dishing phenomenon. Note in Fig. 3.6 that the maximum value X_I can have, is H - the undeformed target plate thickness. Both X_I and X_c are geometrically related to the boundary parameters r_o and Θ_o by the expressions:

$$X_I = r_o(\text{Cot}\alpha - \tan\theta_o) \quad \ldots\ldots\ldots\ldots\ldots\ldots \quad 3.21$$

$$X_c = r_o(\tan\theta_o) \quad \ldots\ldots\ldots\ldots\ldots\ldots\ldots \quad 3.22$$

In addition to these displacement expressions the Inner Zone analysis must also provide a relationship between r_o and θ_o. This is derived by considering the dynamics of identation.

The stresses acting on the Inner Zone during indentation are shown in Fig. 3.6. They are σ_p - the interfacial compressive stress, which is equal to σ_p^* - the mean pressure of resistance of the target material, $\mu\sigma_p$ - the frictional shear stress acting along the target/projectile interface and σ - the membrane stress which has reached a value of Y. If these stresses can be assumed constant over the surfaces on which they act and Inner Zone body forces are small enough to neglect, then the dynamic equation for lateral motion is given by:

$$\pi r_o \, HY \text{Sin}2\theta_o = \pi r_o^2 \, \sigma_p^*(1 + \mu\text{Cot}\alpha) \quad \ldots\ldots\ldots \quad 3.23$$

which simplified gives:

$$r_o = [HY/\sigma_p^* K_I] \, \text{Sin}2\theta_o \quad \ldots\ldots\ldots\ldots\ldots\ldots \quad 3.24$$

In equation 3.24 the term K_I - known as the indentation constant is introduced, where: $K_I = (1 + \mu\text{Cot}\alpha)$. This constant is dependant on the projectile semi-cone angle and the coefficient of friction between the target and projectile. Equation 3.24 is the $r_o - \theta_o$ relationship for indentation. To use it however, requires a value for

the mean pressure of resistance σ_p^*.

In the present context, the mean pressure of resistance is the target/projectile interfacial compressive stress, which is just sufficient to cause plastic flow in the target material. Its value is a function of the prevailing membrane, hoop and frictional stresses and is found here empirically, by considering the indentation-conic deformation transition point.

An expression relating σ_p (a variable) to X_I, r_o and α can be found by eliminating θ_o from equation 3.24 by means of equation 3.21. Equation 3.21 gives:

$$\tan\theta_o = \cot\alpha - X_I/r_o \quad \text{hence:}$$

$$\sin 2\theta_o = 2(\cot\alpha - X_I/r_o)/(1 + \cot\alpha - X_I/r_o)$$

Substituting this expression into equation 3.24 and writing σ_p^* as σ_p gives:

$$\sigma_p = (Y/K_I)[r_o(2H\cot\alpha) - 2HX_I]/[r_o^2(1 + \cot^2\alpha) - r_o(2X_I\cot\alpha) + X_I] \quad \ldots\ldots\ldots\ldots\ldots 3.25$$

Now consider the case of conic deformation where the projectile indents at a constant stress σ_p^* up to the limiting depth X_I^*. At this point σ_p will start to fall below the critical value σ_p^* and will continue to do so for the remainder of the penetration. By substituting this particular value of X_I^* into equation 3.25, a σ_p/r_o relationship results. The form of this function is shown

in Fig. 3.7.

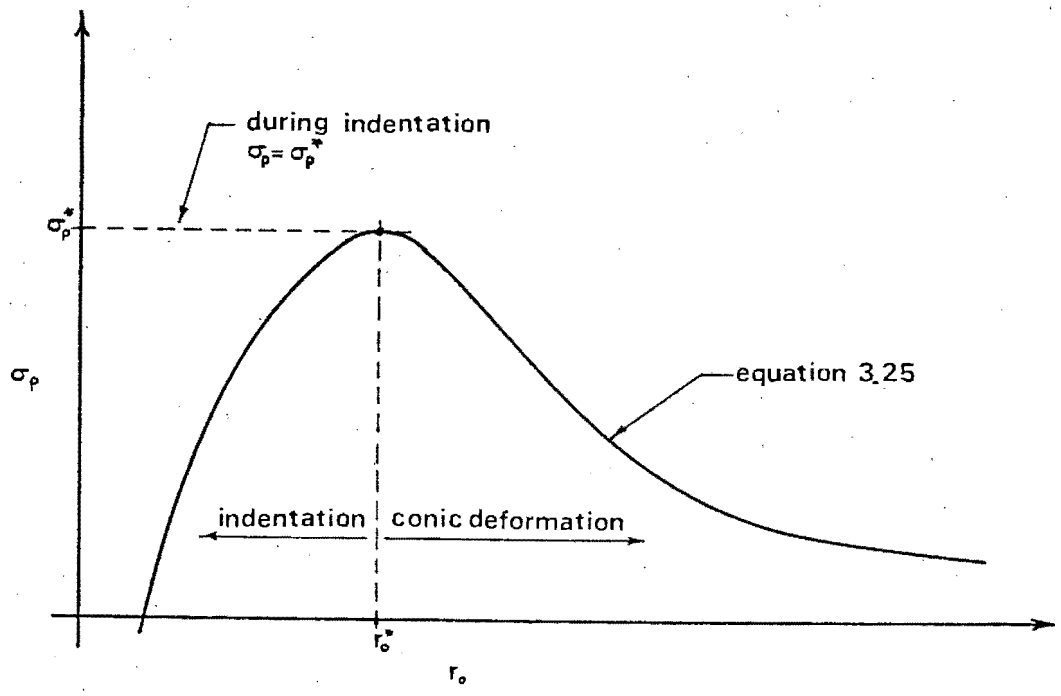

Fig. 3.7 The σ_p / r_o relationship

The σ_p / r_o function is valid only after the turning point at r_o^* since before this value X_I is not a constant. Before r_o^*, $\sigma_p = \sigma_p^*$. This is shown in Fig. 3.7 by the horizontal dashed line. Clearly, if the values of r_o^*, X_I and α are known at the turning point (r_o^*), then the maximal value of σ_p must equal σ_p^*.

Of these parameters, r_o^* can be determined by differentiating equation 3.25 with respect to r_o and equating the result to zero. If it were possible, the remaining two parameters α and X_I^* could be obtained by estimating the indentation depth in ejected target caps. However since this is impractical an alternative procedure has been adopted.

It has been found that the limiting case of conic deformation, (i.e. when $X_I^* = H$ and the projectile just manages to indent to the distal surface of the target plate) requires the greatest amount of penetration energy. By plotting E-α curves such as those shown in Fig. 6.9 it is possible to find the values of α which correspond to this condition.

Substituting these values back into equation 3.26 gives a value for the mean pressure of resistance which can then be used in equation 3.24 to find the required $r_o - \theta_o$ relationship.

For acute angled projectiles, no limiting indentation depth is reached and instead the projectile tip passes through the plate, in what could be described as a radial expansion process. This process is terminated when the hoop strain in the target becomes excessive and radial cracks form in the Inner Zone material to relieve it. This marks the beginning of petalling.

To find a value of σ_p^* which can be used to describe this process, experimental $r_o - \theta_o$ traces such as those shown in Fig. 6.4 have been used. By substituting values of r_o

and θ_o from these traces into equation 3.24 it is possible to calculate a value for σ_p^*

Figs. 3.7a,b show the target displacements which take place during the indentation phase of petalling and conic deformation. Note the minor role played by the Outer Zone (X_{do}) during petalling indentation and asmototic trend of X_I in the conic deformation indentation phase.

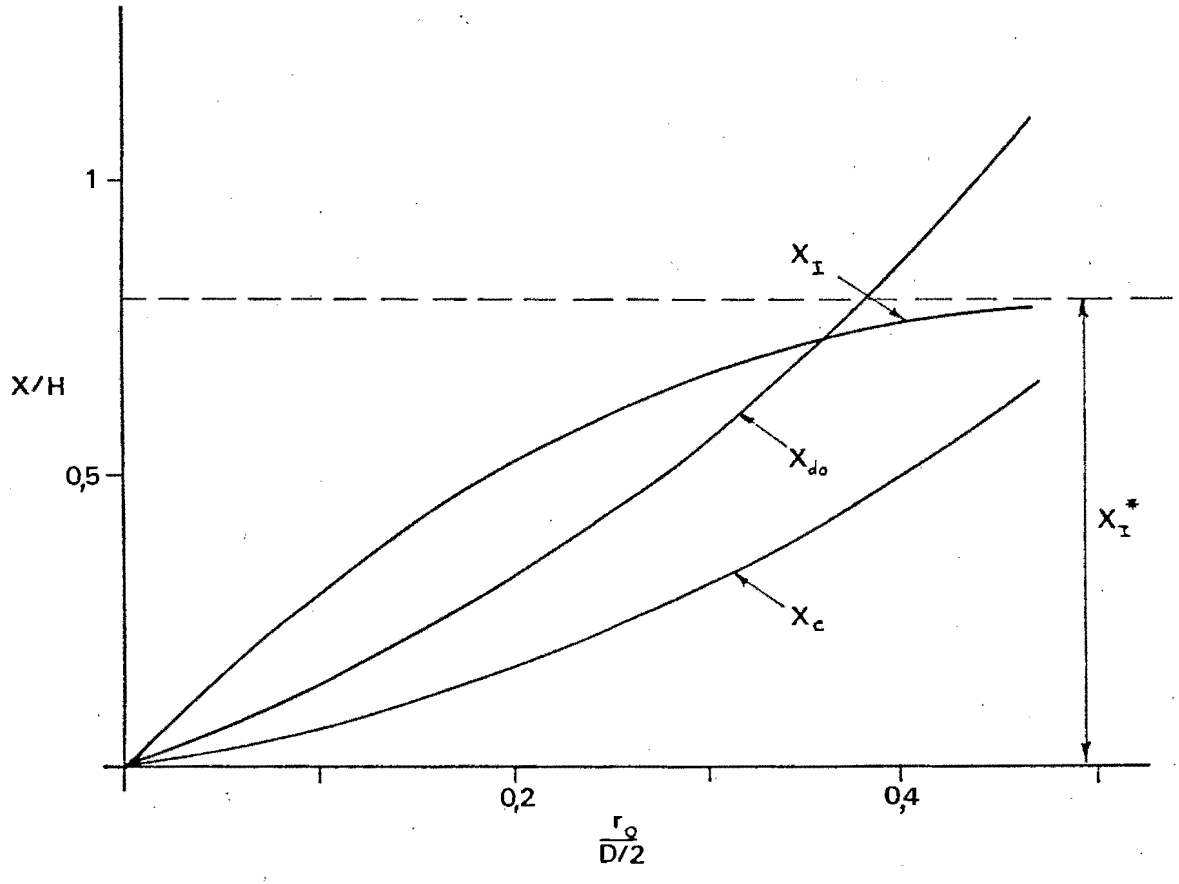

Fig. 3.7a Target displacements during a typical indentation which leads to conic deformation

Fig. 3.7b Target displacements during a typical indentation which leads to petalling

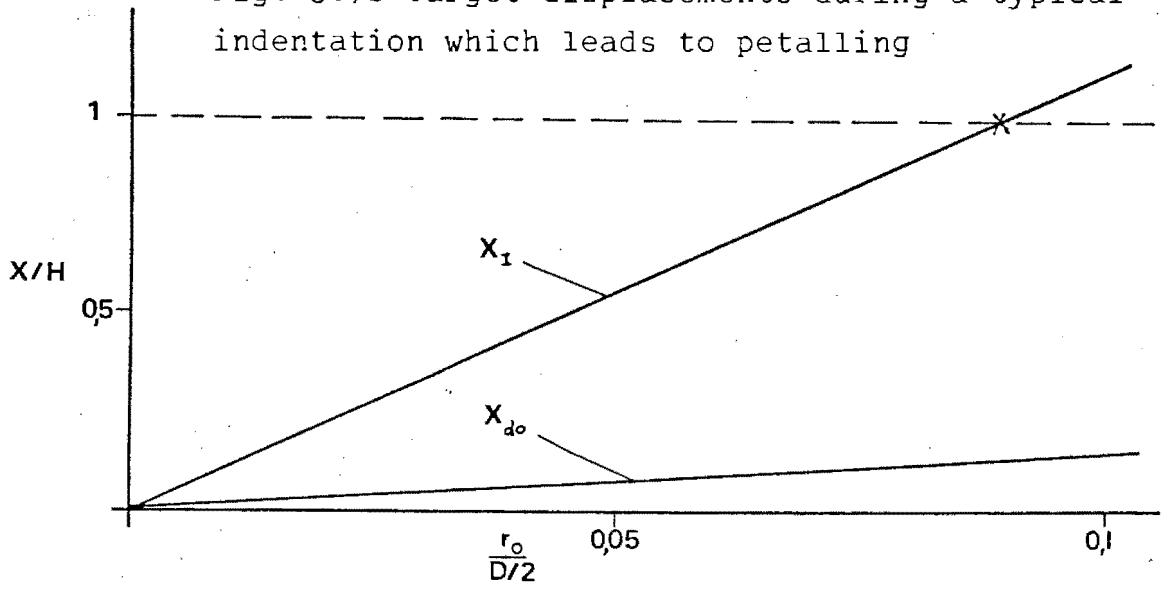

3.2.3 CONIC DEFORMATION

Since the projectile's conical surface is finite, a discontinuity exists at the projectile circumference ie. at $r_o = D/2$. Because of this, both the conic deformation and petalling modes of penetration must be considered in two phases ie. an initial phase when $r_o < D/2$ and a terminal phase when $r_o = D/2$.

The initial phase of conic deformation is closely analogous to indentation, the only difference being that the contact stress is no longer constant at its upper limit σ_p^* but is now a variable where $\sigma_p < \sigma_p^*$. The functional form of σ_p (with respect to r_o) during the initial phase of conic deformation is shown in Fig. 3.7.

Projectile displacement in the Inner Zone during the

initial phase of conic deformation is due solely to the conic deformation mechanism (X_c), since the indentation mechanism (X_I) ceases when σ_p falls below the value of σ_p^* . Thus equation 3.22 gives:

$$X_c = r_o \tan\theta_o \quad \ldots\ldots\ldots\ldots\ldots\ldots\ldots\ldots \quad 3.22$$

The r_o/θ_o relationship for this phase of conic deformation can be found from equation 3.21. This equation was derived for indentation but applies to conic deformation when the variable X_I is set to the constant value of X_I^* . This is the indentation depth reached, when the indentation-conic deformation transition occurs. The relationship is therefore given by:

$$r_o = X_I^*/(\mathrm{Cot}\alpha - \tan\theta_o) \quad \ldots\ldots\ldots\ldots\ldots \quad 3.27$$

A typical r_o/θ_o trace for a penetration which proceeds from indentation to conic deformation is shown in Fig. 3.7a. The indentation section of this trace is given by equation 3.24 and transforms smoothly into the conic deformation mode (equation 3.27) when $X_I \rightarrow X_I^*$.

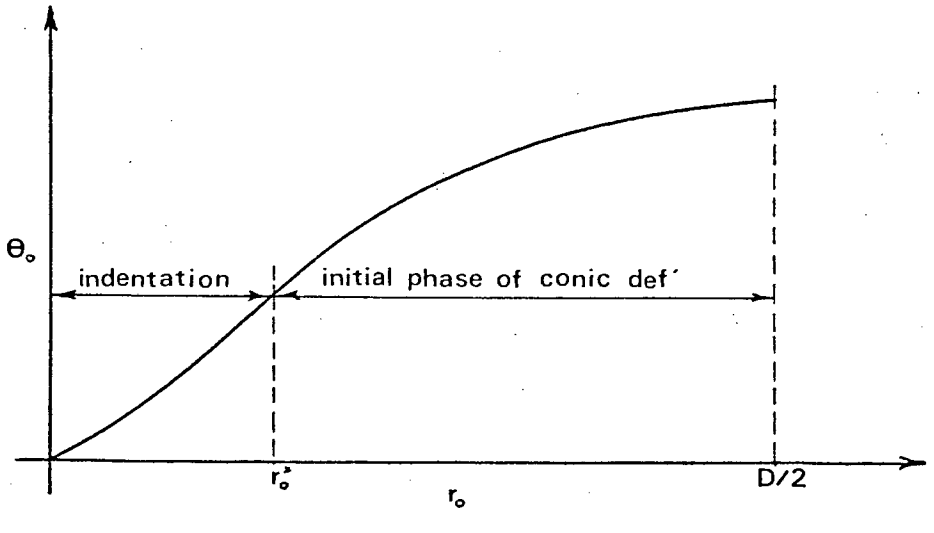

Fig. 3.7a The indentation-conic deformation trace

The terminal phase of conic deformation begins when the projectile/target contact surface reaches its limit at $r_o = D/2$ and is accompanied by significant changes in the deformation pattern.

Firstly the r_o/θ_o relationship derived for the initial phase is no longer valid, since r_o is now a constant and the two parameters are independant of one another. As far as lateral projectile displacements are concerned, the static nature of the Inner-Outer Zone boundary during the terminal phase means that the conic deformation displacement mechanism (X_c) no longer exists. This leaves the Outer Zone dishing mechanism (X_{do}) as the sole projectile displacement mechanism, until shear failure occurs at the Inner-Outer Zone boundary and a shear displacement mechanism (X_s) is introduced.

The most significant change in the deformation pattern is the development of a discontinuity in the plate slope, at the Inner-Outer Zone boundary (see Fig. 3.8). This discontinuity gives rise to a direct shear stress across the plate (σ_s), of magnitude:

$$\sigma_s = Y(\mathrm{Sin}\theta_o - \mathrm{Cos}\alpha) \quad \ldots\ldots\ldots\ldots\ldots\ldots \quad 3.28$$

and leads to the eventual shear failure at the Inner-Outer Zone boundary.

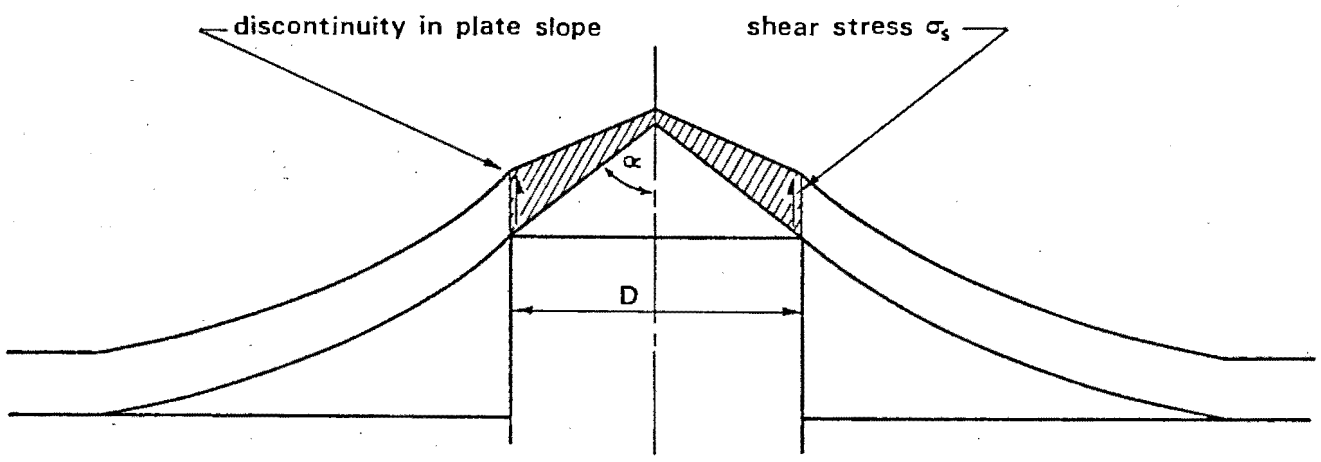

Fig. 3.8 The terminal phase of conical deformation

When σ_s reaches a critical value σ_s^* separation between the Inner and Outer Zone begins. The Inner Zone moves with the projectile at its current velocity, while the Outer Zone is considered to remain fixed in the profile assumed at the time of shear failure initiation. If F* is the target resisting force when shear failure starts, then, as the separation of the Inner Zone (X_s) proceeds, this force is reduced in proportion to the remaining effective target thickness, so that during separation:

$$F = F^*[(H - X_s / H)] \quad \ldots\ldots\ldots\ldots\ldots\ldots \quad 3.29$$

When $X_s = H$, penetration in the conic deformation mode is complete.

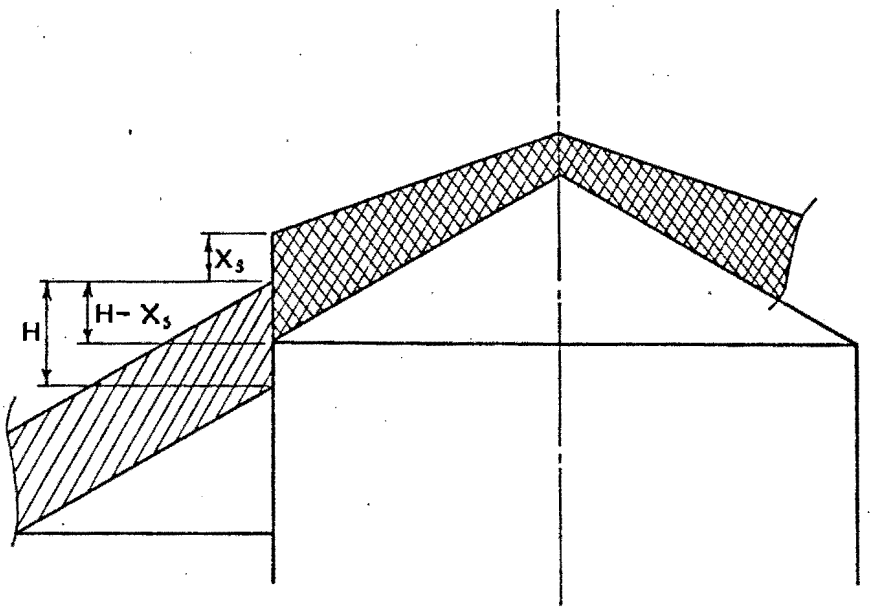

Fig. 3.9 Inner Zone separation

3.2.4 PETALLING

3.2.4.1 INTRODUCTION TO THE PETALLING PROCESS

During the conic deformation process, the target material remains continuous over the point of impact, and a similar deformation pattern to that in the Outer Zone, is assumed to apply ie. membrane strain (ϵ) is large and hoop strain (ϵ_H) is negligibly small. During petalling however, the reverse is true. Here the hoop strain predominates and the membrane strain is negligibly small.

The reason for this difference is that during petalling there is a large relative motion between the projectile and the target material in contact with it. In conic de-

formation, relative motion of this kind occurs only for a short period during indentation (X_I) and in the terminal phase when the Inner Zone is sheared from the target plate (X_S). In the petalling process however, the initial relative motion in the indentation phase (X_I), persists throughout the penetration (Note X_I is termed X_r when $X_I > H$). This relative motion has a radial component due to the conical form of the projectile head and is directly responsible for the large hoop strain and subsequent radial fracture.

The Inner Zone radial fracture pattern develops along with the penetration and critically determines the amount of Inner Zone material involved in the petalling process. Since the overall target response depends on the amount of intact Inner Zone material, the entire penetration process is very sensitive to the radial fracture mechanism.

The manner in which the petalling process propagates is shown schematically in Fig. 3.10.

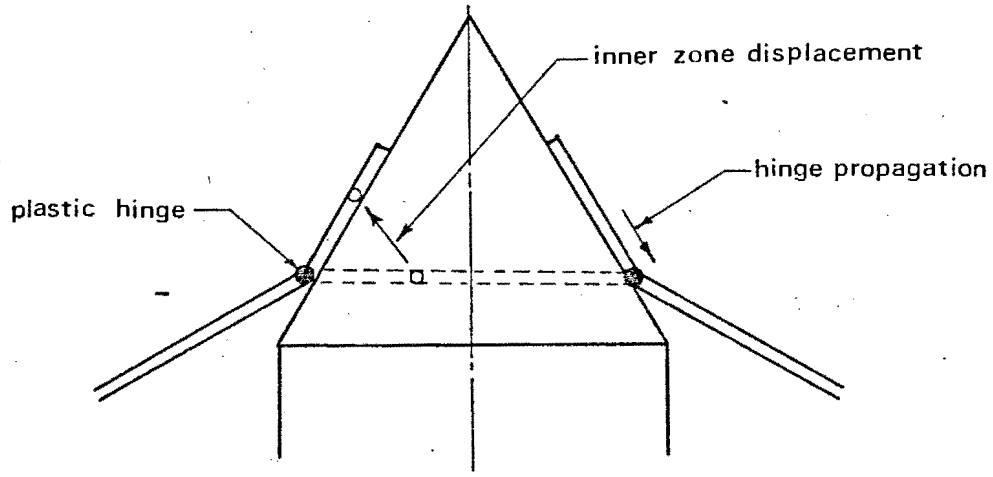

Fig. 3.10 Petalling deformation and particle trajectories

Target material in the Inner Zone is in contact with the projectile cone surface (by definition) and a discontinuity in the plate slope occurs at the Inner-Outer Zone boundary. The plastic hinge which develops at this location moves down the projectile's conical surface as the penetration proceeds and in doing so transfers target material from the Outer Zone to the Inner Zone region. To accomodate this proposed deformation, Inner Zone material undergoes both a lateral and radial displacement, in contrast to the purely lateral motion experienced by the Outer Zone.

Plastic deformation in the Inner Zone can be assumed to take place at constant volume in which case the principle strains ϵ, ϵ_H and ϵ_N are related by equation 3.5, namely:

$$\epsilon + \epsilon_H + \epsilon_N = 0 \quad \ldots\ldots\ldots\ldots\ldots\ldots\ldots\ldots \quad 3.5$$

Since strain along the petal length (ϵ) has been found to be negligibly small, equation 3.5 simplifies to:

$$\epsilon_H = -\epsilon_N \quad \ldots\ldots\ldots\ldots\ldots\ldots\ldots\ldots \quad 3.30$$

To relate these strains to the Inner Zone deformation, consider a typical annular element in this region. Fig. 3.11 shows the cross-section of such an element in the deformed and undeformed positions.

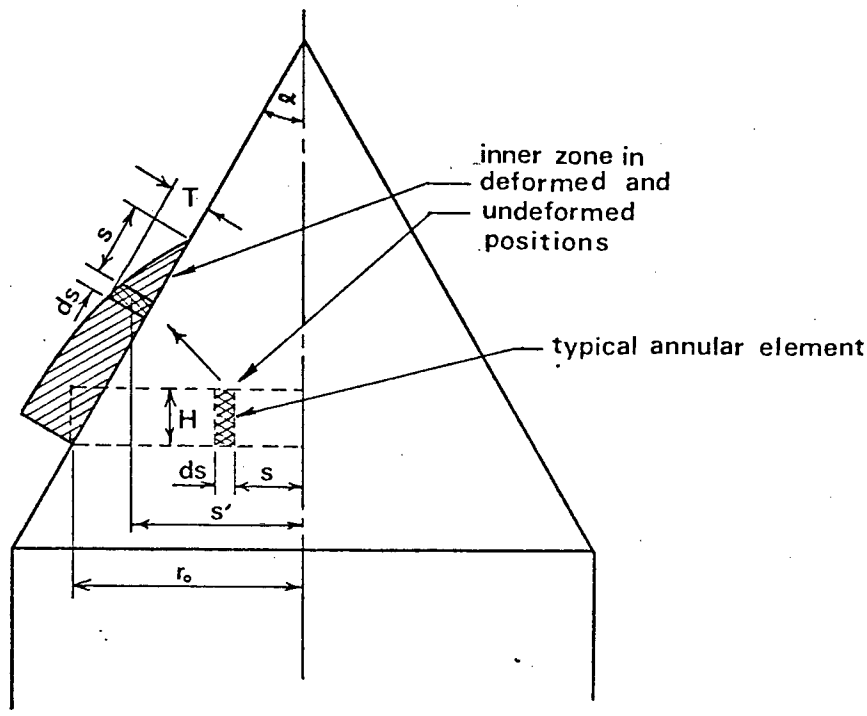

Fig. 3.11 Strain-deformation compatibility

For the deformation at constant volume condition to hold, the cross-sectional area of the element must change so that:

$$HSdS = TS'dS \quad \ldots\ldots\ldots\ldots\ldots\ldots\ldots \quad 3.31$$

and since S' is given by:

$$S' = r_o(1 - \mathrm{Sin}\alpha) + S\mathrm{Sin}\alpha \quad \ldots\ldots\ldots\ldots \quad 3.32$$

equation 3.31 can be written as:

$$T = HS/[r_o(1 - \mathrm{Sin}\alpha) + S\mathrm{Sin}\alpha] \quad \ldots\ldots\ldots \quad 3.33$$

The Inner Zone is therefore subject to a hoop and thickness strain of equal magnitude given by:

$$\epsilon_H = -\epsilon_N = \ln [r_o/S(1 - \sin\alpha) + \sin\alpha] \quad \ldots\ldots\ldots \quad 3.34$$

The distribution of this strain throughout the Inner Zone is shown in Fig. 3.12

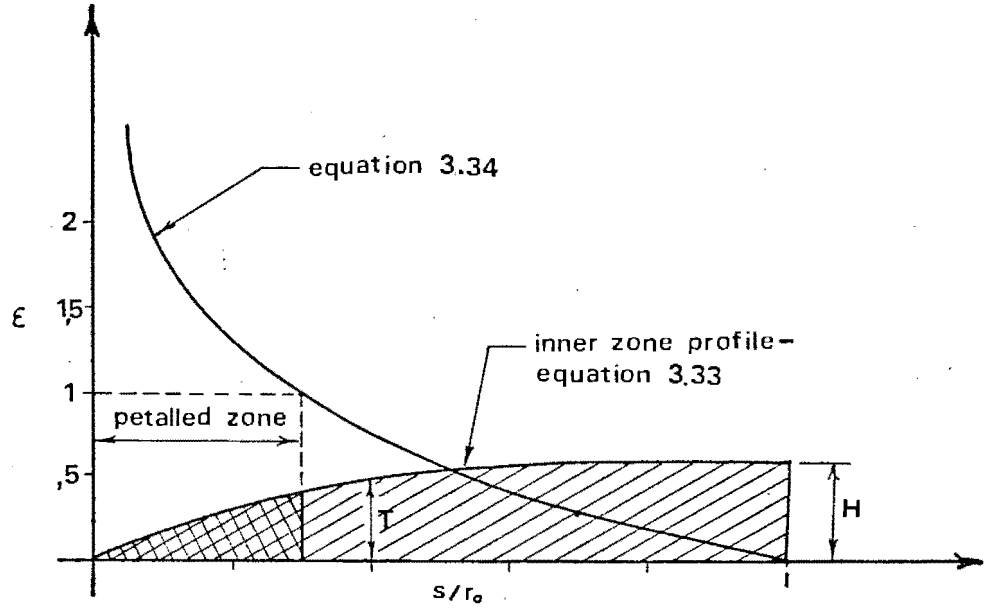

Fig. 3.12 Strain distribution in the Inner Zone during petalling

From this diagram it can be seen that strain is large near the point of impact (tending to infinity at the point of impact) and falls rapidly to zero at the Inner-Outer Zone boundary. As no material is infinitly ductile, radial cracks form at the centre of impact to accomodate the excessive hoop strain. These cracks advance radially as the penetration proceeds and in doing so, divide the Inner Zone into a petalled and an intact region. Of these regions,

only the intact can offer resistance to penetration (if body forces are overlooked).

Target resistance during petalling arises out of the hoop straining and bending of the intact region and to identify the separate contribution of each mechanism requires an accurate physical description of this region. To date, attempts to do this have been unsuccessful, but will be discussed later in Chap. 7 . To circumvent this problem the following empirical approach has been adopted.

3.2.4.2 AN EMPIRICAL MODEL OF PETALLING

As was the case with indentation and conic deformation, the Inner Zone analysis for petalling must be able to describe projectile displacements in the Inner Zone as well as provide an r_o/θ_o relationship for the overall analysis.

Projectile displacement in the Inner Zone during petalling is due solely to the relative motion between the projectile and target material in contact with it (X_r), since the conic deformation component (X_c) does not exist in petalling due to the discontinuity in plate slope at the Inner-Outer Zone boundary. Projectile Inner Zone displacement is therefore given by:

$$X_r = r_o \mathrm{Cot}\alpha \quad \ldots\ldots\ldots\ldots\ldots\ldots\ldots\ldots \quad 3.35$$

For indentation and conic deformation, r_o/θ_o relationships were derived by considering Inner Zone dynamics. The same procedure is used for petalling except that instead of attempting to ascertain the individual contribution of bending and hoop straining of the intact region of the Inner Zone, to the dynamic equation, these components are replaced by the concept of an equivalent annular ring of target material which is subject solely to a hoop strain. This idea is shown graphically in Fig. 3.13

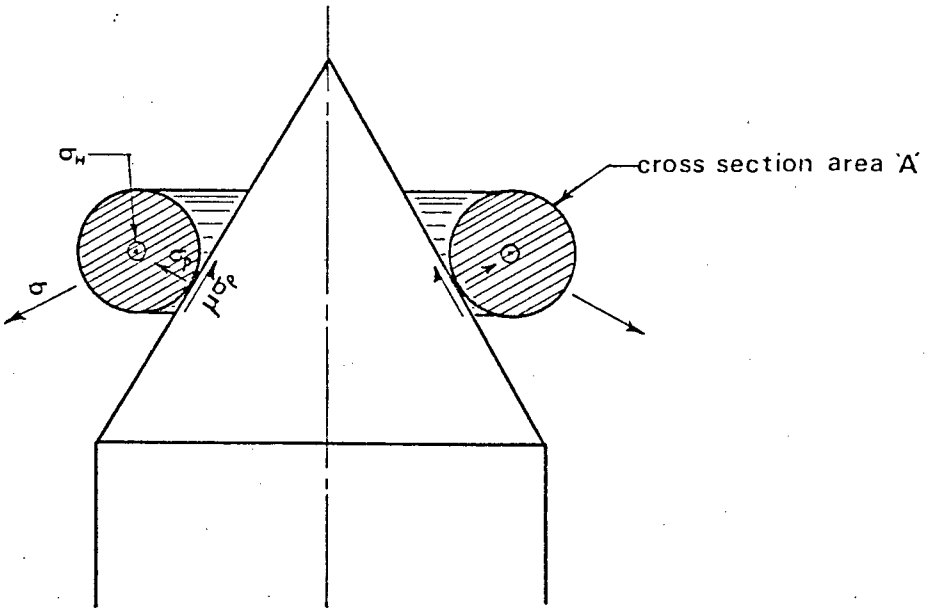

Fig. 3.13 Stresses acting on the equivalent annular ring

During penetration, the annular ring moves down the projectile's conical face. As this happens, the cross-

sectional area A varies, since new Inner Zone material is continually being incorporated from the Outer Zone by the radial expansion of the Inner-Outer Zone boundary and by current Inner Zone material being rendered inactive by the advance of the petalled region.

If the stresses shown in Fig. 3.13 are assumed constant over the surfaces on which they act, and σ and σ_H have attained a value of Y, then eliminating σ_p from the radial and transverse dynamic equations yields the relationship:

$$A = r_o H \left[\text{Cos}\ \theta_o + (\pi/4) K_p\ \text{Sin}2\theta_o\right] \quad \ldots\ldots\ldots\ldots \quad 3.36$$

where $K_p = (1 - \mu \tan\alpha)/(\mu + \tan\alpha)$

Equation 3.36 expresses the manner in which the effective cross-sectional area (A) must change along with the boundary parameters r_o and θ_o, during the petalling process.

If a second equation could be derived expressing the equivalent area A in terms of its bending and hoop strain components, a simultaneous solution with equation 3.36 would result in the required r_o/θ_o relationship. The active element approach does not attempt this however, but uses a <u>linear approximation</u> - independent of θ_o, to represent the A function. This is written as:

$$A = A_F - K_A H (D/2 - r_o) \quad \ldots\ldots\ldots\ldots\ldots\ldots \quad 3.37$$

where the constants A_F and K_A are found empirically from projectile force-displacement histories. Substituting

this expression for A into equation 3.36 results in the following r_o/θ_o relationship for petalling.

$$r_o = [A_F - K_A HD/2]/H[\cos^2\theta_o + (\pi/4)K_P \sin 2\theta_o - K_A] \quad .. \quad 3.38$$

This solution is shown graphically in Fig. 3.14

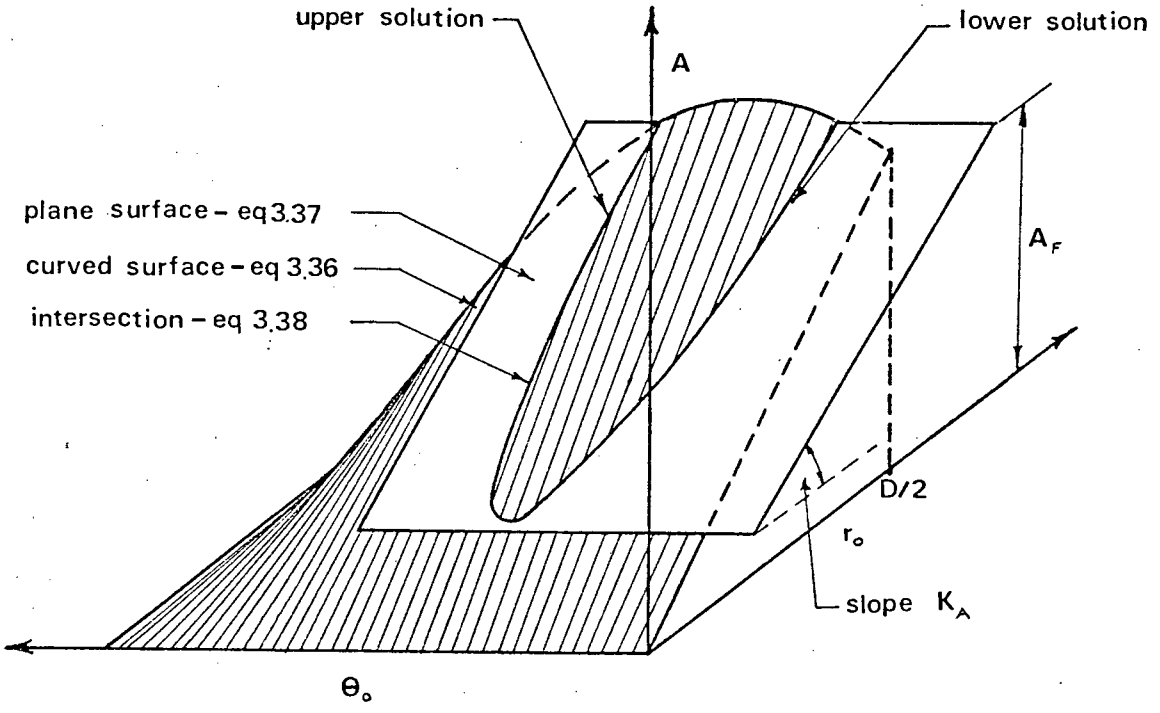

Fig. 3.14 Graphical representation of the petalling r_o/θ_o relationship

Equation 3.38 suggests that two types of r_o/θ_o relationships are possible for petalling, namely an upper solution and a lower solution. These are shown in Fig. 3.15

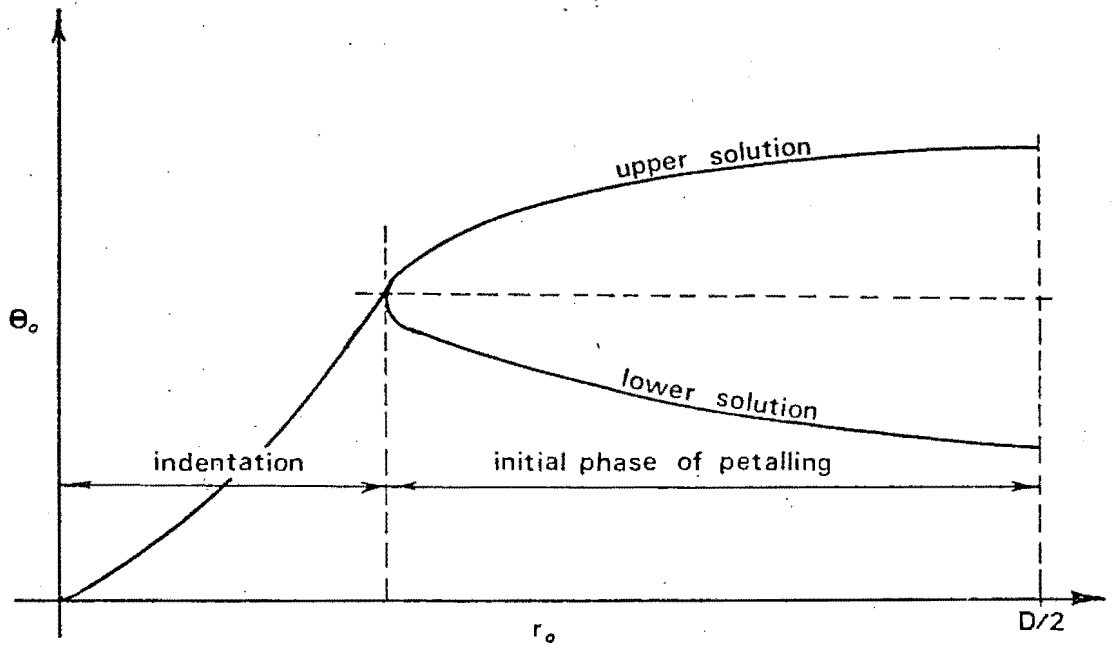

Fig. 3.15 Petalling r_o/θ_o relationships

The lower solution has been found to approximate petalling behaviour while the upper solution shows characteristics similar to those of the conic deformation r_o-θ_o trace (see Fig. 3.7 a). In the present study however, only the lower solution has been utilised.

As was the case in conic deformation, a change in the Inner Zone response occurs when the Inner-Outer Zone boundary reaches the projectile boundary ie. at $r_o = D/2$.

To terminate the petalling process it is necessary to rotate the Inner Zone through an angle of α (see Fig. 3.16), thus enabling the projectile to pass through the target plate.

This rotation causes further hoop strain in the intact region of the Inner Zone which extends the petalling radial cracks. The mechanisms involved in the terminal phase are the same as those in the initial phase, but the analysis derived for the latter is no longer applicable since the boundary parameters (r_o and θ_o) are now independent of one another.

For simplicity, the hoop strain mechanism in the terminal phase is combined with the bending mechanism to form an equivalent bending process. In this simplistic model target resistance is reduced from its value at the end of the initial phase (F*) by the rotation of the Inner Zone. Thus:

$$F = F^*\sin\phi/\sin\alpha \quad \ldots\ldots\ldots\ldots\ldots\ldots\ldots\ldots \quad 3.39$$

This model is shown diagramatically in Fig. 3.16

Projectile displacement during the terminal phase is due solely to the rotation mechanism of the Inner Zone (X_ϕ). This is given by:

$$X_\phi = H(\alpha - \phi)/2 \quad \ldots\ldots\ldots\ldots\ldots\ldots\ldots\ldots \quad 3.40$$

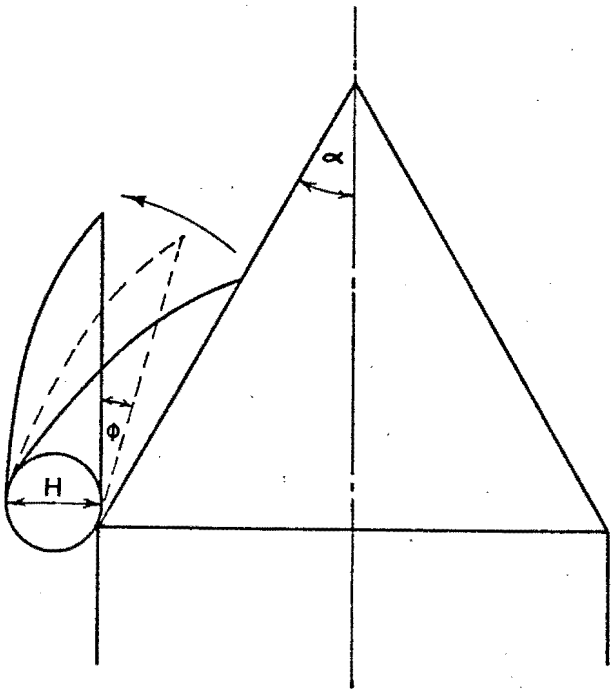

Fig. 3.16 The terminal phase of petalling

3.3 THE OVERALL TARGET MODEL

In the forward integration solution, the penetration period is broken down into sufficiently small intervals to enable constant conditions to be assumed during each time increment. The quantities calculated in the previous sections ie. (X_1 , X_c , X_d , X_r and F) can all be regarded as the mean values of these variables, calculated for each time increment.

Under the action of a constant force (F), projectile motion during each time increment is assumed to be that of a rigid body undergoing constant deceleration. Starting with an initial velocity (V_o) the projectile proceeds to

interact with the target and during the penetration this velocity is constantly reduced, until either the projectile is brought to rest, or the target is perforated, in which case the projectile will proceed with a residual velocity.

Central to the target analysis are the boundary parameters r_o and θ_o . These parameters are related by the expressions derrived in the various Inner Zone analyses. The time dependence of these variables can only be found by means of the overall solution however, which simultaneously takes into account, the responses of the projectile, the Outer Zone and the Inner Zone.

The overall analysis is best summarised by means of a flow diagram. This is shown in Fig. 3.16. The trial and error procedure used in each of the sub-analyses, is also shown in Fig. 3.17.

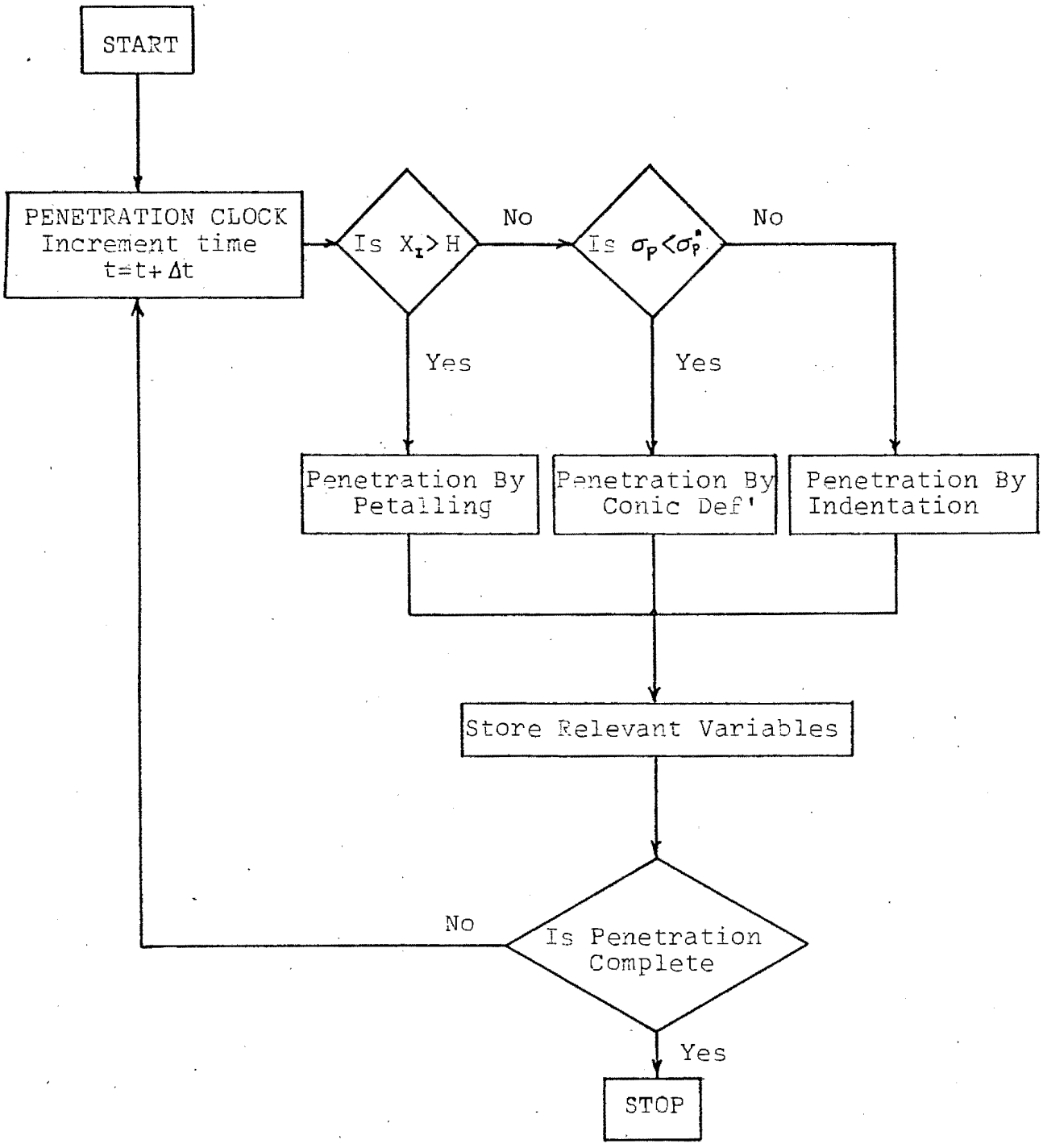

Fig. 3.17 Flow diagram for overall analysis

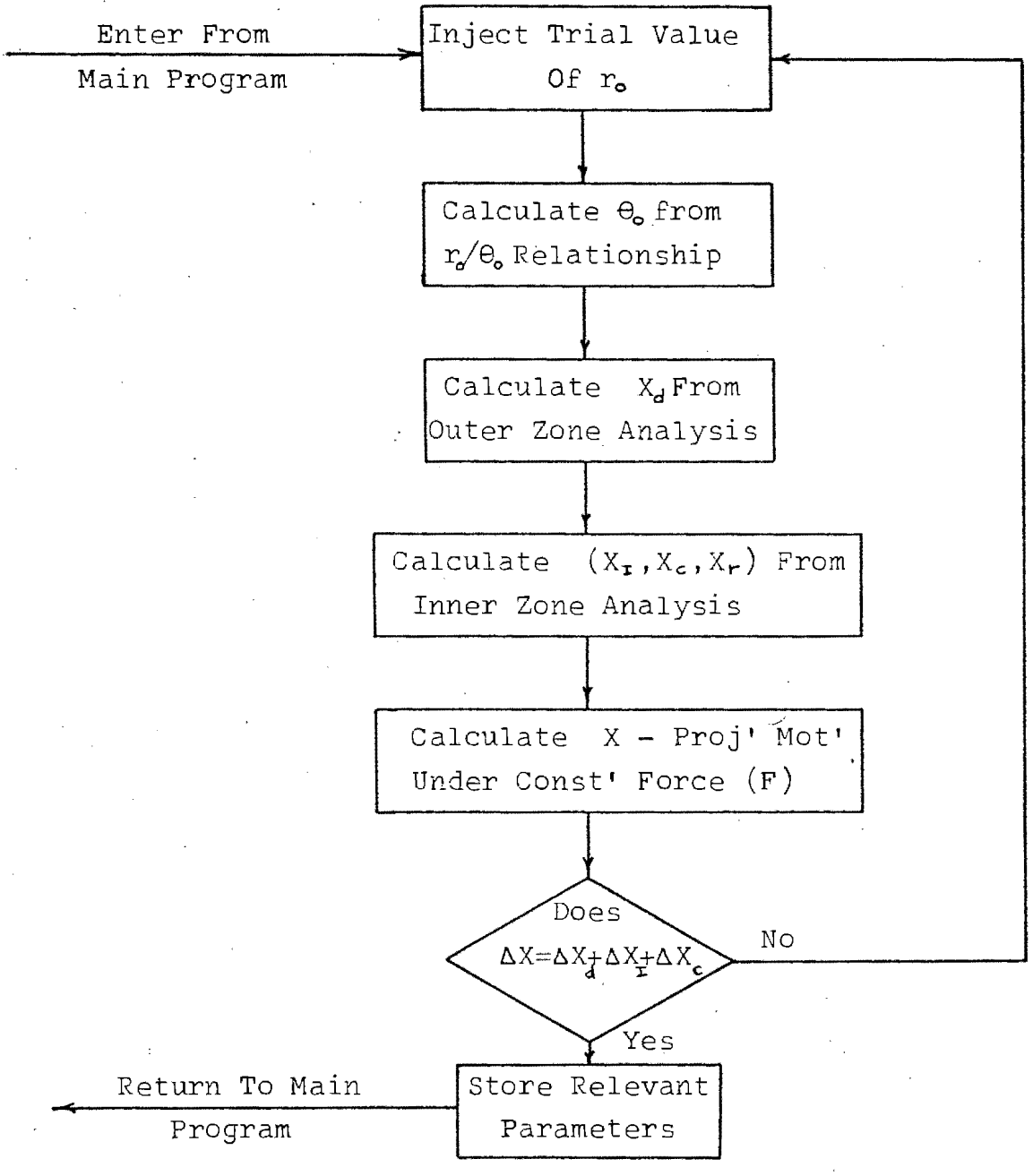

Fig. 3.18 Flow diagram for sub-analyses

CHAPTER 4

PROJECTILE ANALYSIS

The type of projectile used in this study is cylindro-conical in shape and of a composite construction - the head being stainless steel and the body nylon. To simplify the following analysis this composite projectile structure has been modelled as a flat ended isotropic bar of equivalent length (see App. (D)). The conditions at impact for such a projectile are shown in Fig. 4.1

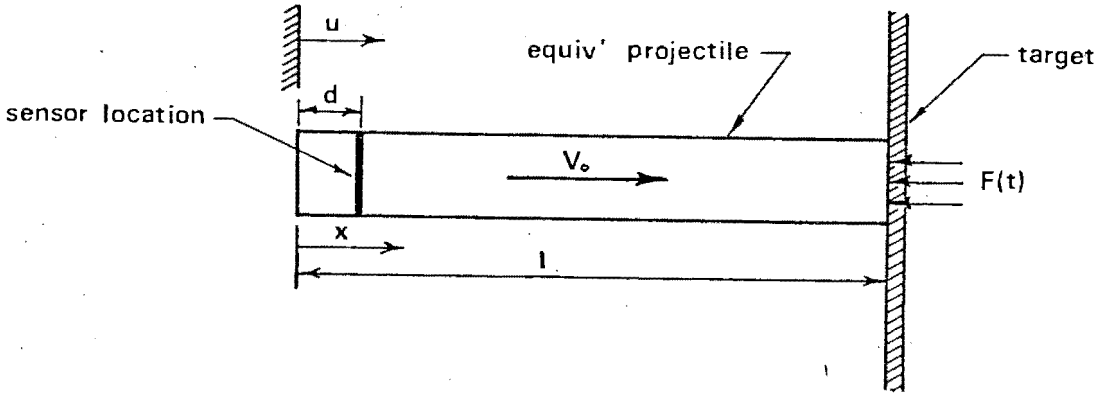

Fig. 4.1 The equivalent projectile at impact

At time t=o the projectile travelling at an initial velocity V_o is acted on by a force function F(t) at its head, causing a stress wave to be propagated along its length. This stress wave is reflected at the tail of the

projectile and consequently travels to and fro in the body of the projectile throughout the penetration. The decelerating force at the projectile head is transmitted to each particle in the projectile by means of these stress waves, so that their common initial velocity V_o is progressively reduced as the projectile is brought to rest. This one-dimensional stress wave behavior is described in general by the equation:

$$\frac{\partial^2 u}{\partial t^2}(x,t) = c^2 \frac{\partial^2 u(x,t)}{\partial x^2} \quad \text{.....} \quad 4.1$$

where $c^2 = E/\rho$ and $u = u(x,t)$ is the displacement of position x in the projectile at time t, relative to laboratory co-ordinates. The boundary conditions for this particular penetration problem are as follows:

at time $t = 0$, $u = 0$ and $\left.\frac{\partial u}{\partial t}\right|_{t=o} = V_o$

at position $x = 0$, $\left.\frac{\partial u}{\partial x}\right|_{x=o} = 0$

$x = \ell$, $\left.\frac{\partial u}{\partial x}\right|_{x=\ell} = \frac{F(t)}{AE}$

Taking the Laplace Transform $U = \mathcal{L}(u)$ of equation 4.1 gives:

$$\lambda^2 U - \lambda U(x,0) - \left.\frac{\partial U}{\partial t}\right|_{x,o} = c^2 \frac{d^2 U}{\partial x^2}$$

$$\frac{d^2 U}{dx^2} = \frac{\lambda^2}{c^2} U - \frac{V_o}{c^2} \quad \text{.....} \quad 4.2$$

Where λ is a complex variable

The standard solution for equation 4.2 is:

$$U = a \cosh\left(\frac{\lambda}{c}x\right) + b \sinh\left(\frac{\lambda}{c}x\right) + \frac{V_o}{\lambda^2} \quad \text{.....} \quad 4.3$$

Differentiating W.R.T.x yields:

$$\frac{dU}{dx} = \frac{\lambda a}{c}\,\mathrm{Sinh}\left(\frac{\lambda}{c}x\right) + \frac{\lambda b}{c}\,\mathrm{Cosh}\left(\frac{\lambda}{c}x\right) \qquad \text{.....} \quad 4.4$$

The boundary conditions at the tail are:

$$\left.\frac{dU}{dx}\right|_{x=o} = \mathcal{L}\left(\left.\frac{\partial u}{\partial x}\right|_{x=o}\right) = 0 \qquad \therefore\ b = 0$$

The boundary conditions at the nose are:

$$\left.\frac{dU}{dx}\right|_{x=\ell} = \frac{\bar{F}(\lambda)}{AE} \quad \text{where } \bar{F}(\lambda) \equiv \mathcal{L}(F(t) \equiv \int_o^\infty e^{-\lambda t}F(t)dt$$

$$\therefore\ \frac{\bar{F}(\lambda)}{AE} = \frac{\lambda a}{c}\,\mathrm{Sinh}\left(\frac{\lambda \ell}{c}\right) \qquad \text{or } a = \frac{c}{AE}\,\frac{\bar{F}(\lambda)}{\mathrm{Sinh}(\lambda\ell/c)}$$

Substituting the values of a and b back into 4.3 yields:

$$U = \frac{c}{AE} \cdot F(\lambda)\,\frac{\mathrm{Cosh}(\lambda x/c)}{\lambda\ \mathrm{Sinh}(\lambda\ell/c)} + \frac{V_o}{\lambda^2}$$

Taking the inverse transform gives:

$$u(x,t) = \frac{1}{2\pi i}\int_{\gamma-i\infty}^{\gamma+i\infty} e^{\lambda t}\left[\frac{V_o}{\lambda^2} + \frac{c}{AE}\,\bar{F}(\lambda)\,\frac{\mathrm{Cosh}\ (\lambda x/c)}{\lambda\ \mathrm{Sinh}(\lambda\ell/c)}\right] d\lambda \quad \text{.....} \quad 4.5$$

This general expression for particle motion will now be used to prove the final result which is stated as:

The displacement, velocity and deceleration of the centre of mass at any instant t may be computed from the average of the displacement, velocity and deceleration respectively, of a point on the projectile a distance d from the base, by the equation:

$$\frac{c}{\ell}\int_{t-(\ell+d)/c}^{t+(\ell-d)/c} W(d,t)dt = W_{cm}(t) + W_{cm}\left(t - \frac{2d}{c}\right) \qquad \text{.....} \quad 4.6$$

Where W = displacement, velocity or deceleration.

The proof of 4.6 is as follows:

$$\text{Let } U^* = c/\ell \int_{t'-\ell/c}^{t'+\ell/c} u(d,t)dt$$

Now the solution for u (x,t) was found in 4.5. Substituting this solution into the above relationship and setting x = d ⟶

$$U^* = \frac{1}{2\pi i}\frac{c}{\ell}\int_{\Upsilon-i\infty}^{\Upsilon+i\infty}\int_{t'-\ell/c}^{t'+\ell/c} e^{\lambda t}dt\left[\frac{V_o}{\lambda^2} + \frac{c}{AE}\,\bar{F}(\lambda)\frac{\text{Cosh }(\lambda d/c)}{\lambda\ \text{Sinh}(\lambda\ell/c)}\right]d\lambda$$

evaluating the inner integral ⟶

$$U^* = \frac{1}{2\pi i}\,\frac{c}{\ell}\int_{\Upsilon-i\infty}^{\Upsilon+i\infty} e^{\lambda t'}\frac{(e^{\lambda\ell/c} - e^{-\lambda\ell/c})}{\lambda}\left[\frac{V_o}{\lambda^2} + \frac{c}{AE}\,\frac{\bar{F}(\lambda)\ \text{Cosh }(\lambda d/c)}{\lambda\ \text{Sinh}(\lambda\ell/c)}\right]d\lambda$$

$$\text{or}\quad U^* = \frac{1}{2\pi i}\int_{\Upsilon-i\infty}^{\Upsilon+i\infty}\left[\frac{c}{\ell}\cdot\frac{e^{\lambda t'}}{\lambda^3}\cdot 2\,\text{Sinh}\left(\frac{\lambda\ell}{c}\right)V_o + \frac{e^{\lambda t'}c^2}{AE\ell}\,\bar{F}(\lambda).\frac{2\text{Cosh}(\lambda d/c)}{\lambda^2}\right]d\lambda$$

A B

Now A can be simplified by Cauchy's 2nd integral formula since

$$\frac{1}{2\pi i}\int_{\Upsilon-i\infty}^{\Upsilon+i\infty}\frac{e^{\lambda t'}}{\lambda^3}\,\text{Sinh}\left(\frac{\lambda\ell}{c}\right)V_o\,d\lambda = V_o\ t'\ell/c$$

B can be rewritten as follows, by expanding Cosh λd/c

$$B = \frac{1}{2\pi i}\int_{\Upsilon-i\infty}^{\Upsilon+i\infty}\frac{2}{M}\,F(\lambda)\left[\frac{e^{\lambda(t'+d/c)} + e^{\lambda(t'-d/c)}}{2\lambda^2}\right]d\lambda$$

$$\text{Where } \frac{c^2}{AE\ell} = \frac{1}{M}$$

By writing $T = t + d/c$ the exponential part of the integral can be rewritten as:

$$\int_{-\infty}^{T}\int_{-\infty}^{T} e^{\lambda t}\,dt\,dT + \int_{-\infty}^{T-2d/c}\int_{-\infty}^{T} e^{\lambda t}\,dt\,dT$$

Recombining $U^* = A + B$ ⟶

$$U^* = 2V_o t' + \frac{1}{2\pi i}\int_{-\infty}^{T}\int_{-\infty}^{T}\int_{\gamma-i\infty}^{\gamma+i\infty} \frac{1}{M}\,\bar{F}(\lambda)e^{\lambda t}\,d\lambda\,dt\,dT \quad +$$

$$\frac{1}{2\pi i}\int_{(-\infty)}^{(T-2d/c)}\int_{(-\infty)}^{(T)}\int_{(\gamma-i\infty)}^{(\gamma+i\infty)} \frac{1}{M}\,\bar{F}(\lambda)e^{\lambda t}\,d\lambda\,dt\,dT$$

or

$$U^* = 2V_o t' + \underbrace{\frac{1}{M}\int_{-\infty}^{T}\int_{-\infty}^{T} F(t)\,dt\,dT}_{C} + \underbrace{\frac{1}{M}\int_{-\infty}^{T-2d/c}\int_{-\infty}^{T} F(t)\,dt\,dT}_{D} \qquad \ldots\ldots\ldots 4.7$$

Expressing $F(t)$ in terms of the motion of the centre of mass ⟶

$$F(t) = M\ddot{X}_{cm}(t)$$

$$\therefore \int_{-\infty}^{T} \ddot{X}_{cm}(t)\,dt = V_{cm}(T) - \cancel{V_{cm}(-\infty)}^{\,V_o} = \frac{1}{M}\int_{-\infty}^{T} F(t)\,dt$$

$$\text{and } V_{cm}(T) = V_o + \frac{1}{M}\int_{-\infty}^{T} F(t)\,dt \qquad \ldots\ldots\ldots 4.8$$

Integrating 4.8 ⟶

$$\int_{-\infty}^{T} V_{cm}(T)\,dT = \int_{-\infty}^{T} V_o\,dT + \frac{1}{M}\int_{-\infty}^{T}\int_{-\infty}^{T} F(t)\,dt\,dT$$

Evaluating the integral gives the displacement relationship

$$u_{cm}(t) = V_o t + \frac{1}{M} \int_{-\infty}^{T} \int_{-\infty}^{T} F(t)dtdT \quad \ldots\ldots\ldots\ldots\ldots\ldots \quad 4.9$$

4.9 gives an expression for term C in expression 4.7.

Also from 4.8 ⟶

$$\frac{1}{M} \int_{-\infty}^{T} F(t)dt = \frac{\delta u_{cm}(T)}{\delta t} - V_o$$

$$\therefore \frac{1}{M} \int_{-\infty}^{T-2d/c} \int_{-\infty}^{T} F(t)dtdT = \int_{-\infty}^{T-2d/c} \frac{\delta u_{cm}(T)dt}{\delta t} - \int_{-\infty}^{T-2d/c} V_o$$

Which gives for term D in 4.7 ⟶

$$u_{cm}(T-2d/c) - V_o(T-2d/c) - V_o(-\infty)^{0}$$

Rewriting 4.7 using the above substitutions gives:

$$U^* = 2V_o(T-d/c) + [u_{cm}(T)-V_o(T)]+[u_{cm}(T-2d/c) - V_o(T-2d/c)]$$

simplifying ⟶

$$U^* = u_{cm}(T) + u_{cm}(T-2d/c)$$

As defined

$$U^* = c/\ell \int_{T-\frac{(\ell+d)}{c}}^{T+(\ell-d)/c} u(d,t)dt = u_{cm}(T) + u_{cm}(T-\frac{2d}{c})$$

Q.E.D

The above can be verified for velocity and acceleration.

CHAPTER 5

EXPERIMENTAL METHOD

5.1 INTRODUCTION AND BACKGROUND TO MONITORING TECHNIQUES

To carry out an experimental study of penetration it is necessary, in addition to monitoring the actual penetration process, to be able to launch the projectile at reproducible velocities and to absorb any excess kinetic energy which may remain after penetration. Since the main concern of this thesis is to observe the penetration process however, the present chapter will deal only with the monitoring aspect of penetration and details of ancilliary equipment can be found in App. A and B.

Whereas most previous work in the field has neglected either Inner or Outer Zone response to permit a tractable solution, the present work considers both reponses and for this reason requires a knowledge of both projectile and target motion. Equation 2.2 describes the interaction of the projectile and target motions and can be written as:

$$X = X_{oz} + X_{iz} \quad \ldots\ldots\ldots\ldots\ldots\ldots\ldots\ldots\ldots\ldots \quad 2.2$$

To use this equation at least two of the variables must be known.

The projectile monitoring system, in addition to producing penetration force-time histories, also provides projectile displacement-time data which can be used in equation 2.2. Of

the remaining two variables (X_{oz}, X_{Iz}), the latter has been chosen to represent target response. This paramater is monitored indirectly by recording Inner Zone radial expansion ($r_o(t)$) which is directly related to $X_{Iz}(t)$ by the expression:

$$X_{Iz} = r_o \cot\alpha \quad \ldots\ldots\ldots\ldots\ldots\ldots\ldots\ldots \quad 3.35$$

In addition to monitoring projectile motion and target Inner Zone expansion, a third independent method has also been developed to monitor transverse motion of the Outer Zone at one specific location. Information gained from this method is used for cross-checking purposes. These three techniques will be dealt with separately in the following sections.

Penetration in general is characterised by high rates of loading and short durations. To monitor such rapidly occuring events, limitations are imposed by the relatively slow reponse times of most phenomena commonly employed in measuring techniques. Two phenomena which have sufficiently fast response times however, are light and electricity and these have been employed by researchers over the past seventy years, primarily to record displacement-time histories of the target and projectile.

The earliest attempts to record dynamic penetration phenomena were made at the turn of the century using photographic techniques. The first quantitative results to be obtained by this means were reported by Masket (18) in 1946. He obtained a displacement-time history of a projectile's tail surface during penetration, in the form of a photographic streak record. Fig. 5.1 shows the

schematic layout of this apparatus.

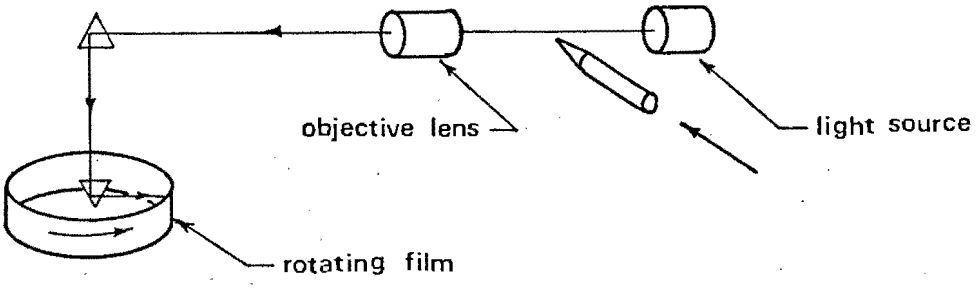

Fig. 5.1 Masket's apparatus

In 1955 Bluhm (21) used an electrical method to monitor the displacement-time history of particle motion in an impacted projectile. He did this by strain-gauging a projectile, mounting it rigidly and firing targets at it. By inverting the problem in this manner, he neatly circumvented the problem of recording data from a moving projectile, though changing the boundary conditions somewhat.

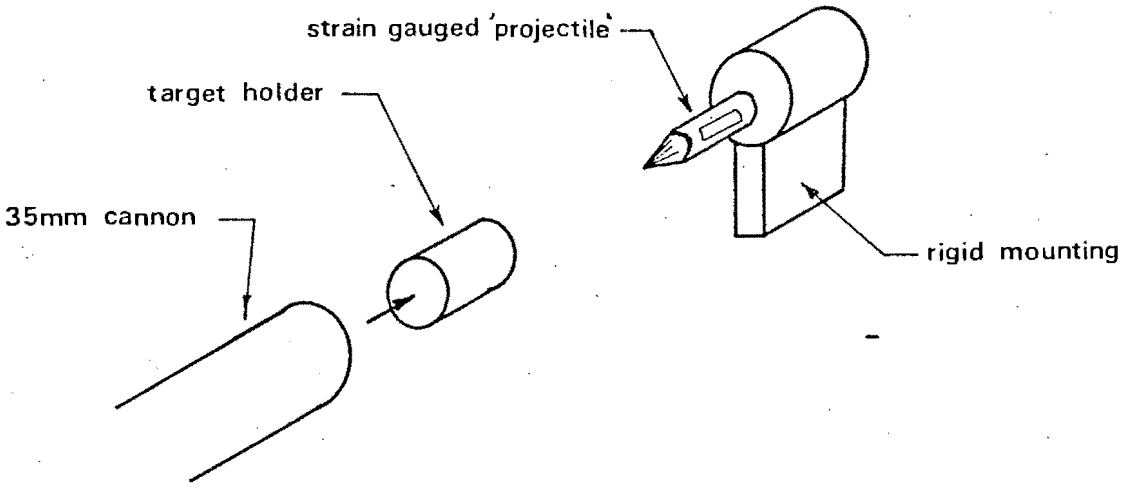

Fig. 5.2 Bluhm's apparatus

Recent work by Goldsmith et. al. (12), Skidmore (14) and Beynet (13) has involved the use of commercially available high speed cameras. These investigations recorded the changing target profile during penetration - Goldsmith and Skidmore photographing this directly and Beynet using a Moiré fringe technique. In addition to this, Goldsmith (12) monitored target strains by means of radial and tangential strain gauges as well as lateral plate displacement using dynamic displacement gauges.

The most recently reported electrical method to monitor projectile displacement directly, is due to Wingrove (22). Here the displacement of the projectile tail surface is monitored by means of the change in capacitance between the moving projectile and a fixed co-axial electrode. The idea is shown schematically in Fig. 5.3

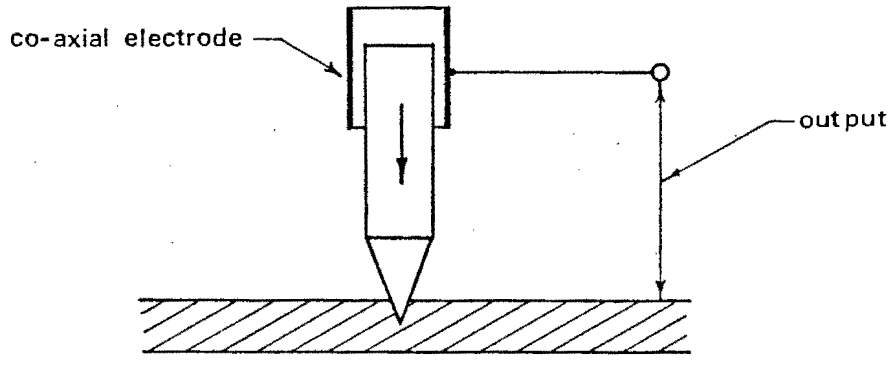

Fig. 5.3 Wingrove's apparatus

Common to all these methods is the fact that the

recorded data is in the form of a displacement-time history of the penetration process. To derive force-time information about the penetration however, requires a knowledge of the second derivative of projectile displacement with respect to time. Several methods have been devised to do this.

The most obvious method of obtaining the higher derrivatives of projectile displacement is by numerically differentiating projectile-time data (1,18). To obtain results of any value however, extremely accurate primary data is required, as the numerical differentiation process grossly amplifies any errors that are present. To avoid this problem, Goldsmith (12) used a different procedure. He prescribed the functional form of the projectile deceleration-time trace, integrated it twice to produce a displacement-time expression with unknown coefficients and then fitted it to his experiemental displacement-time data. This enabled the required coefficients to be found, and by reversing the procedure, the deceleration-time and hence force-time histories could be obtained. It should be noted that the final result, obtained in this manner, is only as accurate as the prescribed deceleration-time function.

The experimental method used in this thesis, was developed specifically to overcome the problem of ob-

taining higher derivatives of projectile displacement. There are three possible procedures which can be used to obtain the required derivatives. If X is the projectile displacement, these procedures can be represented as:

1. $X \rightarrow \dot{X} \rightarrow \ddot{X}$ ..... Classical approach
2. $X \leftarrow \dot{X} \leftarrow \ddot{X}$ ..... Ideal approach
3. $X \leftarrow \dot{X} \rightarrow \ddot{X}$ ..... Alternative approach

When higher derivatives can be obtained as primary data (2 and 3) it is a simple matter to obtain the required lower derivatives by an integration process. This technique does not require extremely accurate primary data as was the case with the numerical differentiation procedure.

Two monitoring techniques were considered for the present study each utilising a natural phenomena directly related to the higher derivatives of projectile displacement. The first shown in Fig. 5.4 utilises the piezo-electric effect of a quartz crystal, activated by the body force of a small mass attached to it. On striking the target, the local projectile particle deceleration at the tail surface could theoretically be monitored by this device, thus giving the penetration data directly in the form of the highest derivative required ($\ddot{X}$).

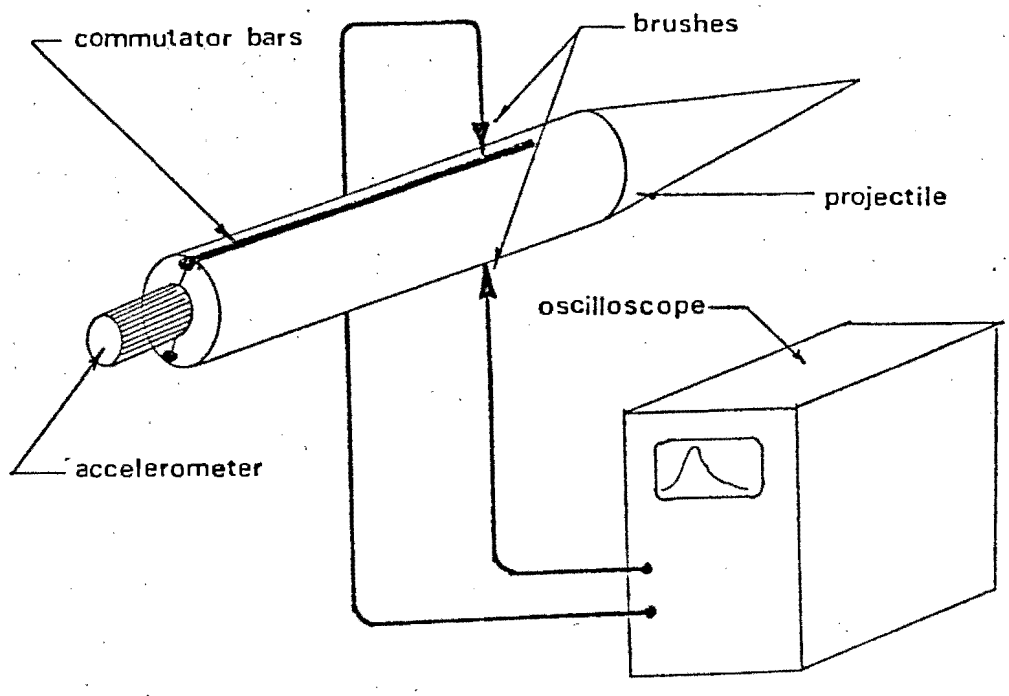

Fig. 5.4 Piezo-electric accelerometer method

The second method shown in Fig. 5.5 utilises the electro-magnetic induction phenomenon, namely, that when an electrical conductor of length l cuts a magnetic field of intensity B, perpendicularly, at a velocity V, an electrical potential is developed across the ends of the conductor, which is directly proportional to the velocity of the conductor and the strength of the magnetic field ie.

$$e = BlV \quad \ldots\ldots\ldots\ldots\ldots\ldots\ldots \quad 5.1$$

If the quantities B and l are held constant, then the voltage developed in the conductor is directly proportional to its velocity. The system shown in Fig. 5.5 utilising

this phenomenon, could thus monitor the first derivative of displacement ($\dot{X}$).

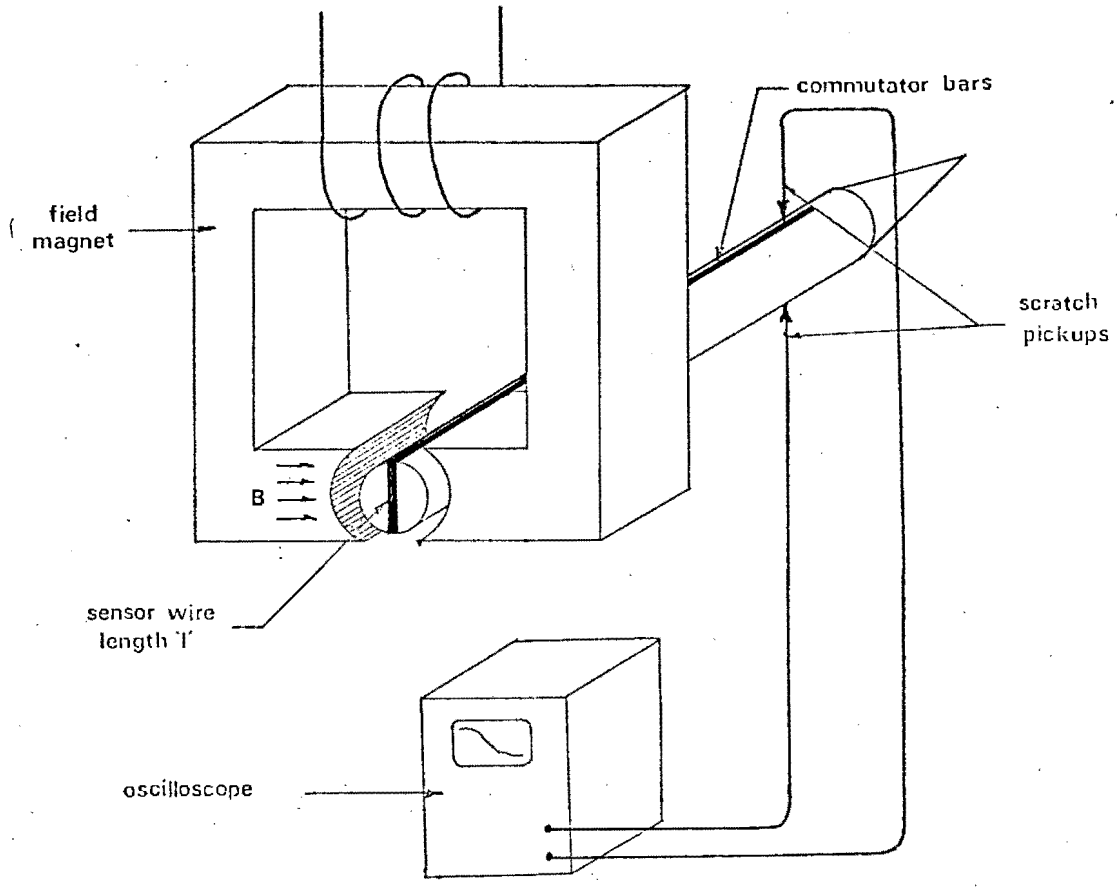

Fig. 5.5 Electro-magnetic induction method

Since the accelerometer method produces the second de rivative of displacement with respect to time as primary data, this method would appear, at first sight, to have an advantage over the velocity transducer method. In practice however, the accelerometer method is difficult to realise. The output signal obtained from a typical piezo-electric transducer is small and to successfully transmit such a signal through the proposed commutator bars would be virtually impossible.

The velocity transducer method on the other hand, is capable of generating a substantial signal and is robust and simple. In addition, the output signal can simultaneously be integrated and differentiated electronically to produce primary data which is directly proportional to a specific particle displacement, velocity and acceleration in the projectile. This method was adopted for the present research program and the following section gives a detailed account of the practical aspects of its construction.

5.2 THE PROJECTILE MONITORING APPARATUS

To facilitate description, the apparatus will be discussed under the following sub-headings:

5.2.1 The field magnet and mounting

5.2.2 The pickup section

5.2.3 The projectile

5.2.4 The approach velocity measuring system

5.2.5 Signal processing instruments

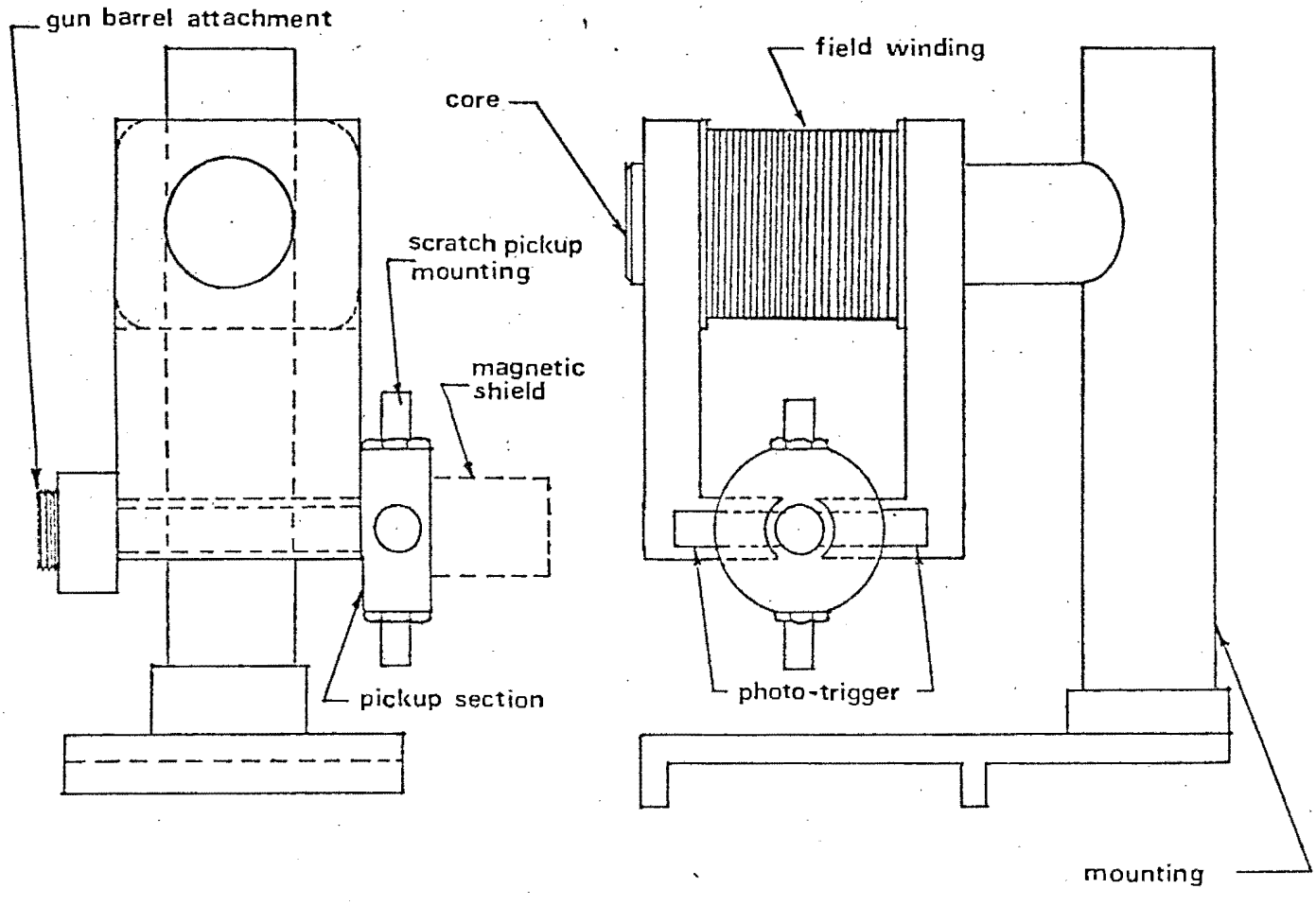

Fig. 5.6 General assembly

5.2.1 FIELD MAGNET AND MOUNTING

An electromagnet of 2 800 turns of 0,1 mm diameter copper wire is used to generate the magnetic field. The

latter is conducted via a soft iron core and pole pieces, to produce a uniform field in the pickup section. Using a variable d.c. voltage supply, the magnetic field strength in the air gap can be varied from zero to 1 Wb/m^2 .

The electromagnet is mounted using brass and austenitic stainless steel fittings to prevent magnetic leakage to the steel bed of the gun. The clamping arrangement has 3 degrees of freedom to facilitate the alignment of the pickup section and the pole pieces, with the gun barrel.

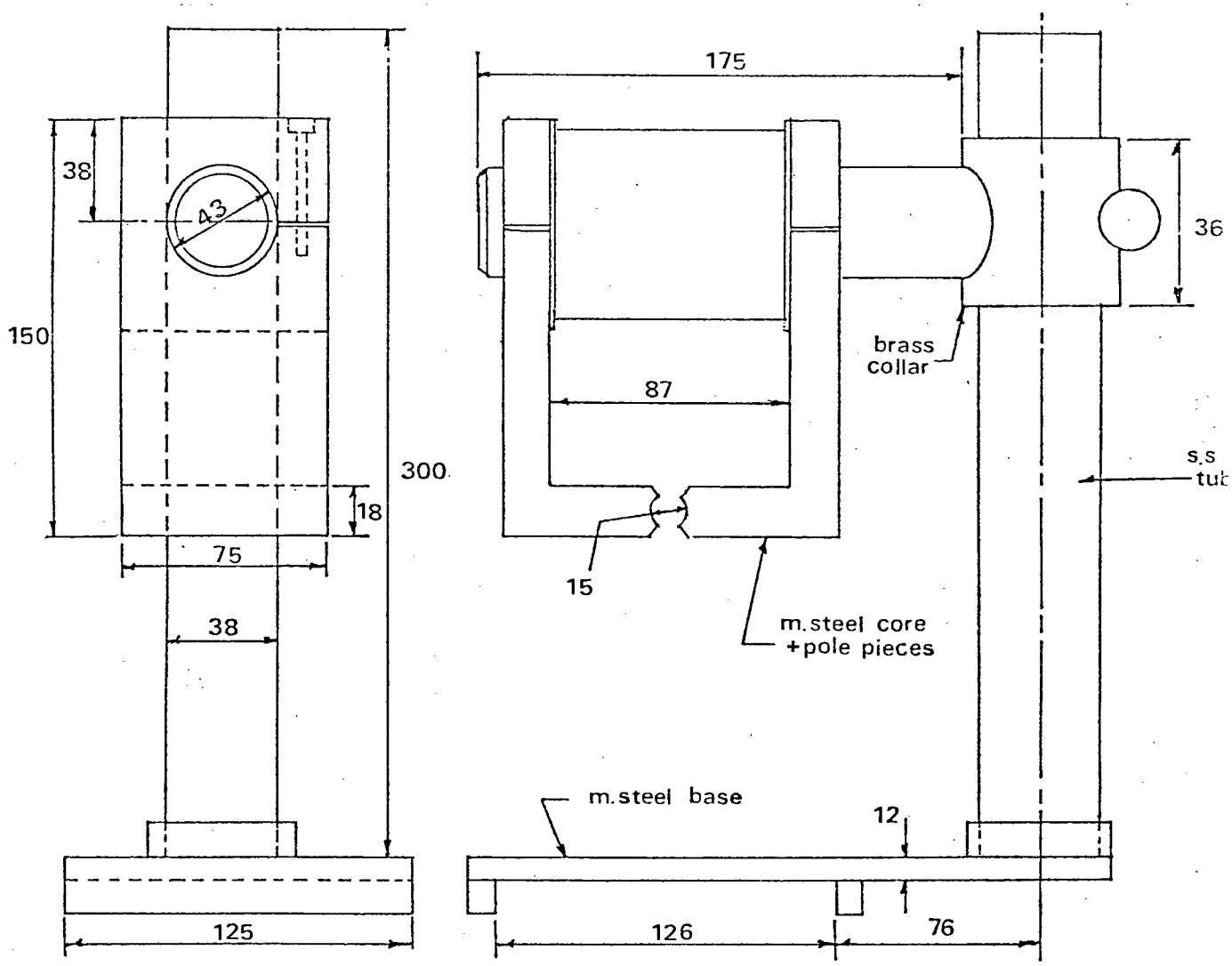

Fig. 5.7 Field magnet and mounting

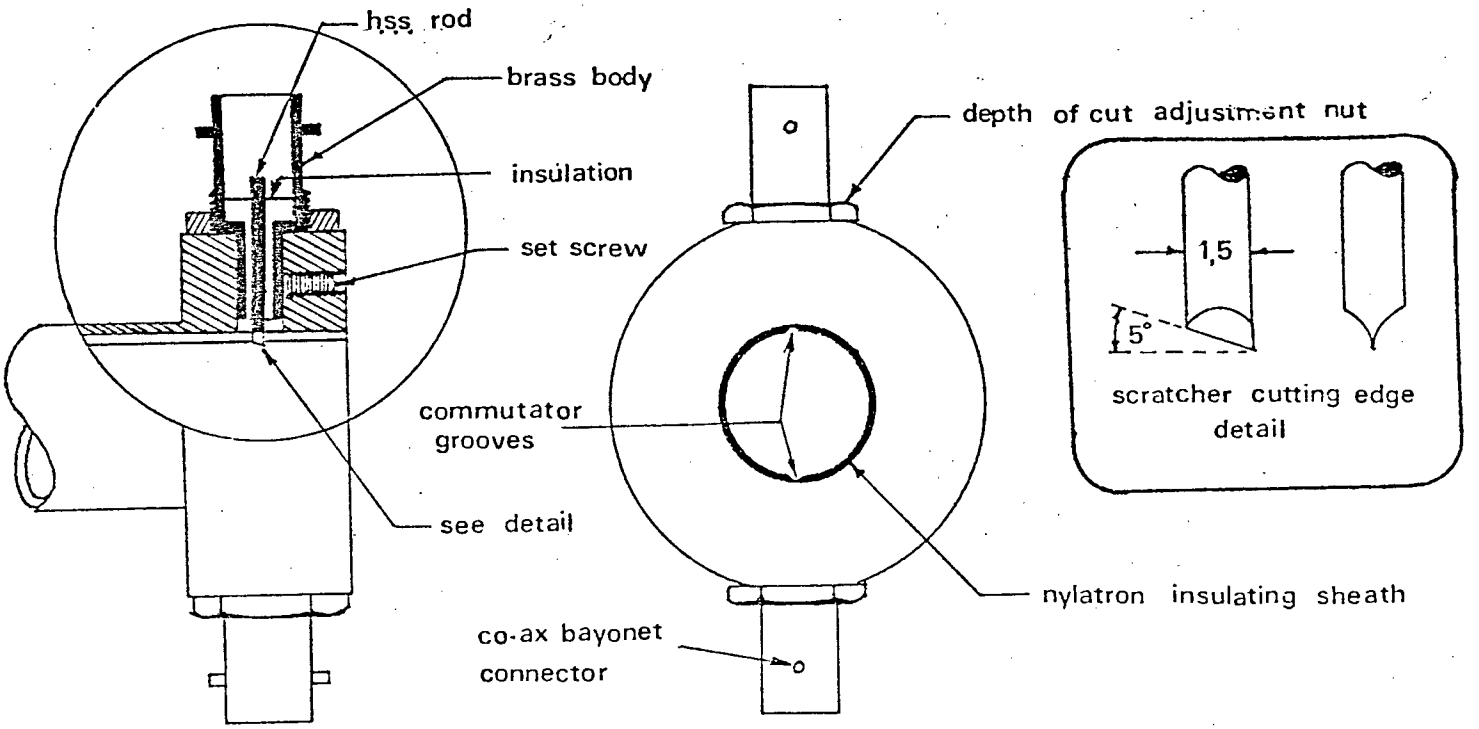

Fig. 5.8 Pickup section

5.2.2 THE PICKUP SECTION

The function of this section is to guide the projectile in the correct orientation, through the magnetic field. The walls of the guide-tube are of brass and minimally thick to prevent magnetic field distortion and attenuation. The inner wall of the guide-tube is lined with an insulating plastic (nylatron G.S.) to prevent electrical shorting of the projectile's commutator strips. These strips also act to guide the projectile as they travel along the axial grooves

in the barrel and pickup section (see Fig. 5.8).

Fig. 5.9 shows the factors which determine the position and size of the various components. The projectile length has been kept to a minimum to keep the sensing conductor as close to the impacting surface as possible.

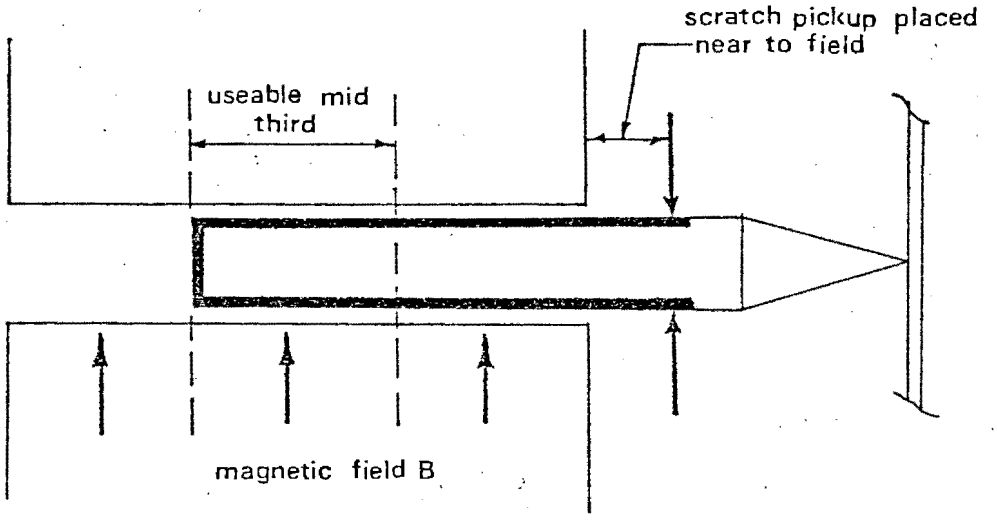

Fig. 5.9 Factors determining the transducer's linear range

The scratch pickups are situated at the target end of the pickup section as close to the magnetic field as possible. Details of their construction are shown in Fig. 5.10. A scratch pickup consists of a 1 mm diameter high-speed steel rod, ground at the contact end to form a wedge-shaped cutting point. The rod is insulated from the brass body of the pickup section and the latter effectively shields the electrical signal from outside electrical noise. Connection to the recording apparatus is made

via heavy duty shielded cable.

Initially the cutting point was ground with positive rake so that the passing commutator strips were actually "machined". This arrangement however, did not produce a uniform contact pressure, and the swarf produced often shorted out the signal to earth if it came into contact with the brass body of the pickup section. The present "negative rake" configuration gives a good uniform contact pressure and the cutting point tends to forge a groove through the commutator material leaving no swarf. The points hold their edge and are still sharp after more than two hundred shots.

Depth of cut is regulated by means of the adjustment nut shown in Fig. 5.10. This is done by inserting a 12,5 mm plug into the barrel and lowering the scratch pickups until they just make contact with the plug. Since the commutator groove is 0,1 mm deep, when the projectile passes with the pickups adjusted as above, a 0,1 mm deep groove is cut along the commutator strip.

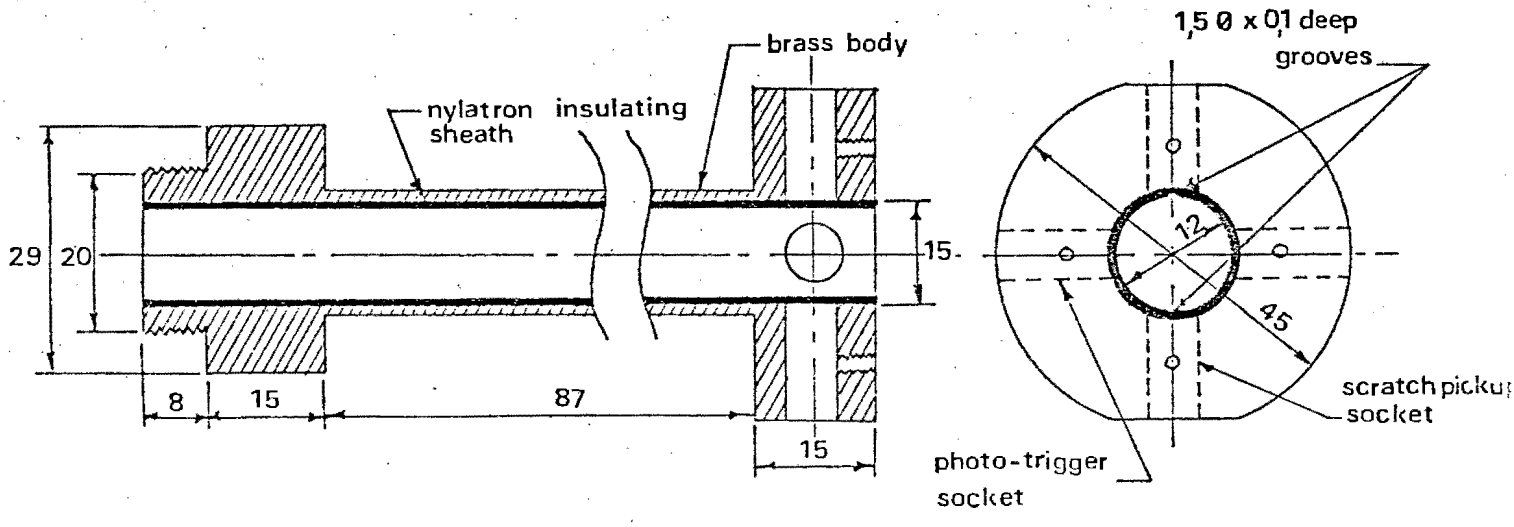

Fig. 5.10 Scratch pickup detail

5.2.3 THE PROJECTILE

Two configurations were tried. The first shown in Fig. 5.11 is appealing in its simplicity, but as its output voltage is limited at low velocities, noise associated with the scratch pickups, becomes too significant.

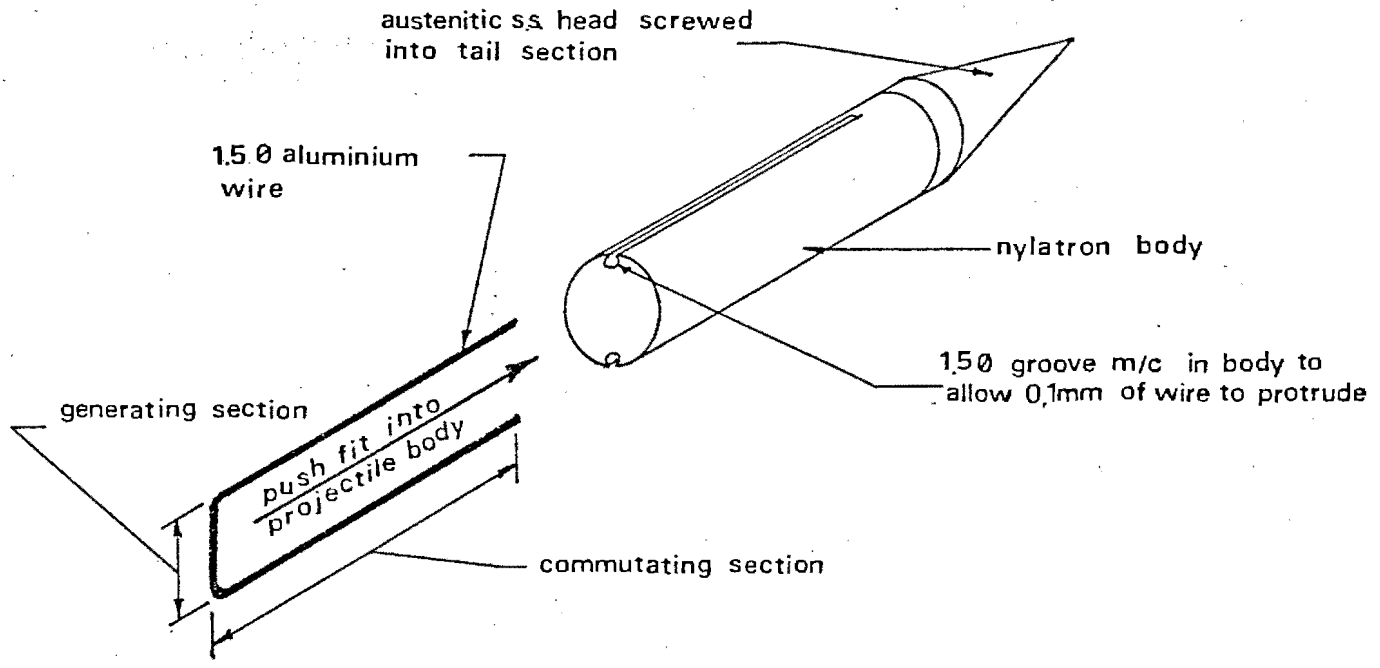

Fig. 5.11 Projectile Mk 1

After experimenting with the Mk 1 projectile it was realised that a far larger singal/noise ratio is required if electronic differentiation is to be attempted. With an upper bound on the magnetic field strength due to saturation of the iron pole pieces, the only alternative was to effectively increase the number of generating con-

ductors and connect them together in series. This was accomplished by winding a coil of wire on the projectile body as shown in Fig. 5.12

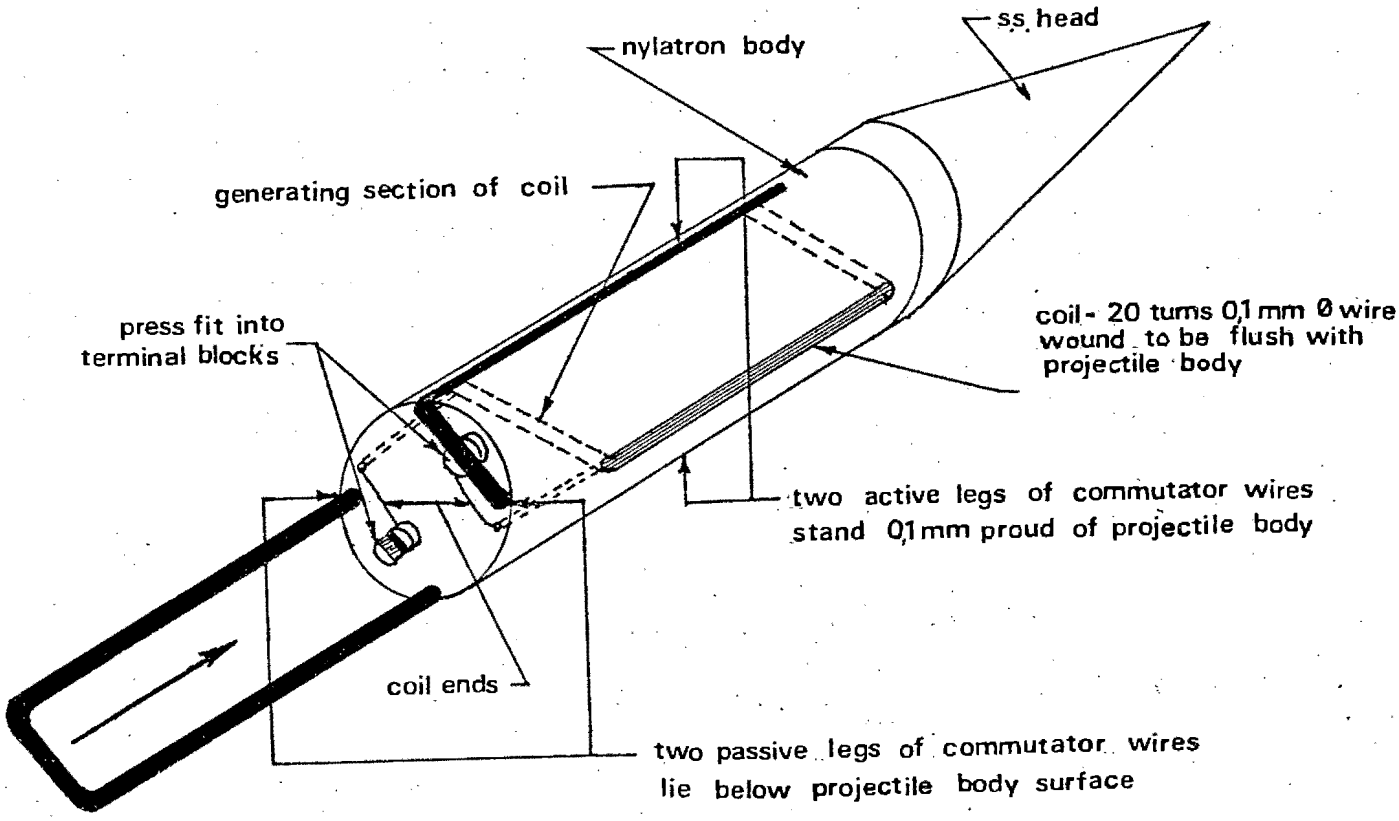

Fig. 5.12 Projectile Mk 11

As with the Mk 1 projectile, U shaped aluminium wire commutators were used. This was done to keep the "mass

balance" of wire the same on either side of the projectile, as the large decelerations encountered (200,000 m/s^2) would rip an assymetrical configuration apart. The arrangement was also economical on wire, since after each shot the wire U would be turned around to present the unscratched leg as a commutator. Initially, copper wire was used, but later abandoned as its high density to strength ratio caused the wire to fail continually at the high deceleration rates encountered.

The use of a coil of 20 turns of wire increased the output twenty-fold so that on the average, the present output signal is in the order of one volt. It will be appreciated that additional precautions had to be taken using a coil. Firstly, if a coil is passed through a magnetic field the net flux cutting the coil is zero and hence no e.m.f. is generated. If one section of the coil can be effectively shielded from the field, e.m.f. will again be generated. In the Mk 11 configuration, the forward diametral section of the coil is allowed to leave the uniform magnetic field and passes through a magnetic shield during the critical part of the penetration measurement. This leaves the rear diametral section of the coil as the sole e.m.f. generator.

By using a coil to generate an e.m.f., added problems of distortion and phase lag due to self-inductance were an-

ticipated. The following calculations show however that for the given coil and expected rates of change of voltage, the back e.m.f. induced by the coil are insignificant.

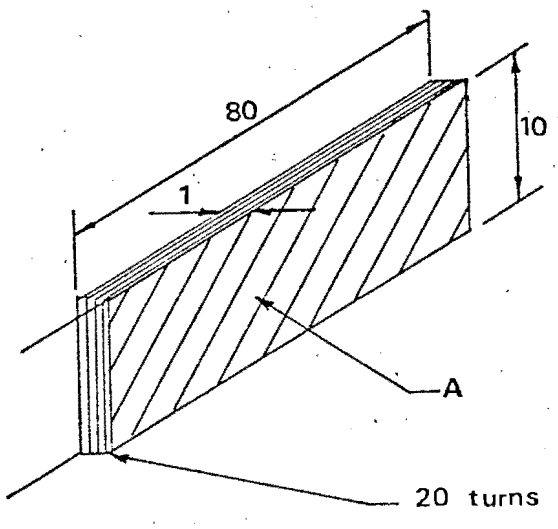

Where:
A = area of coil
d = coil depth=1mm
n = no of turns
$\mu = 4\pi \times 10^{-7}$

Fig. 5.13 Coil configuration

For a coil the self inductance is given by

$$L = (n^2 \mu A)/d \quad \ldots\ldots\ldots\ldots\ldots\ldots \quad 5.2$$

Substituting the coil dimensions into this equation gives:

$$L = 4{,}02 \times 10^{-4} \text{ Henry}$$

From a typical voltage-time trace the maximum slope can estimated to be approximately

$2,5 \times 10^{3}$ V/S. This signal is fed to the oscilloscope input which has a resistance of 1 MΩ giving:

$$\left(\frac{di}{dt}\right)_{max} = 2,5 \times 10^{-3} \text{ A/S}$$

The back e.m.f. generated in the coil is therefore

$$L\left(\frac{di}{dt}\right)_{max} = 1,05 \times 10^{-6} \text{ V}$$

Compared with the primary voltage this is negligably small.

5.2.4 APPROACH VELOCITY MEASURING APPARATUS

Rather than rely on the absolute determination of the e.m.f.-velocity relationship from a knowledge of the effective coil length and the magnetic field strength, a device was made to measure the approach velocity of the projectile. Knowing this, the calibration constant K_v can be found, since the vertical axis of the oscilloscope is calibrated in volts, and the initial part of the velocity time trace, which is horizontal, represents the approach velocity, (see Fig. 5.16). Hence;

$$e_o = K_v V_o \quad \ldots\ldots\ldots\ldots\ldots\ldots\ldots\ldots \quad 5.3$$

Both deceleration and displacement can be calculated from this initial calibration.

The device itself consists of two light beams across the projectile path and a measured distance D mm apart.

The beams are arranged to fall onto two photo-transistors, which are connected to two Schmitt triggers. These triggers are used to start and stop an electronic digital clock capable of measuring to an accuracy of $\pm$ 1 μs. When the projectile breaks the first beam, the timer is started and when it breaks the second beam the timer is stopped. Knowing the time taken to cover the measured distance D mm, the muzzle or approach velocity can be calculated.

The photo-sensors are mounted on the gun barrel by means of adjustable collars (see Fig.5.14 and photo 5.2). To ensure that the projectile is no longer being accelerated by the driver pressure of the gun, four 15 cm long slots are cut in the barrel to vent the driver pressure to atmosphere.

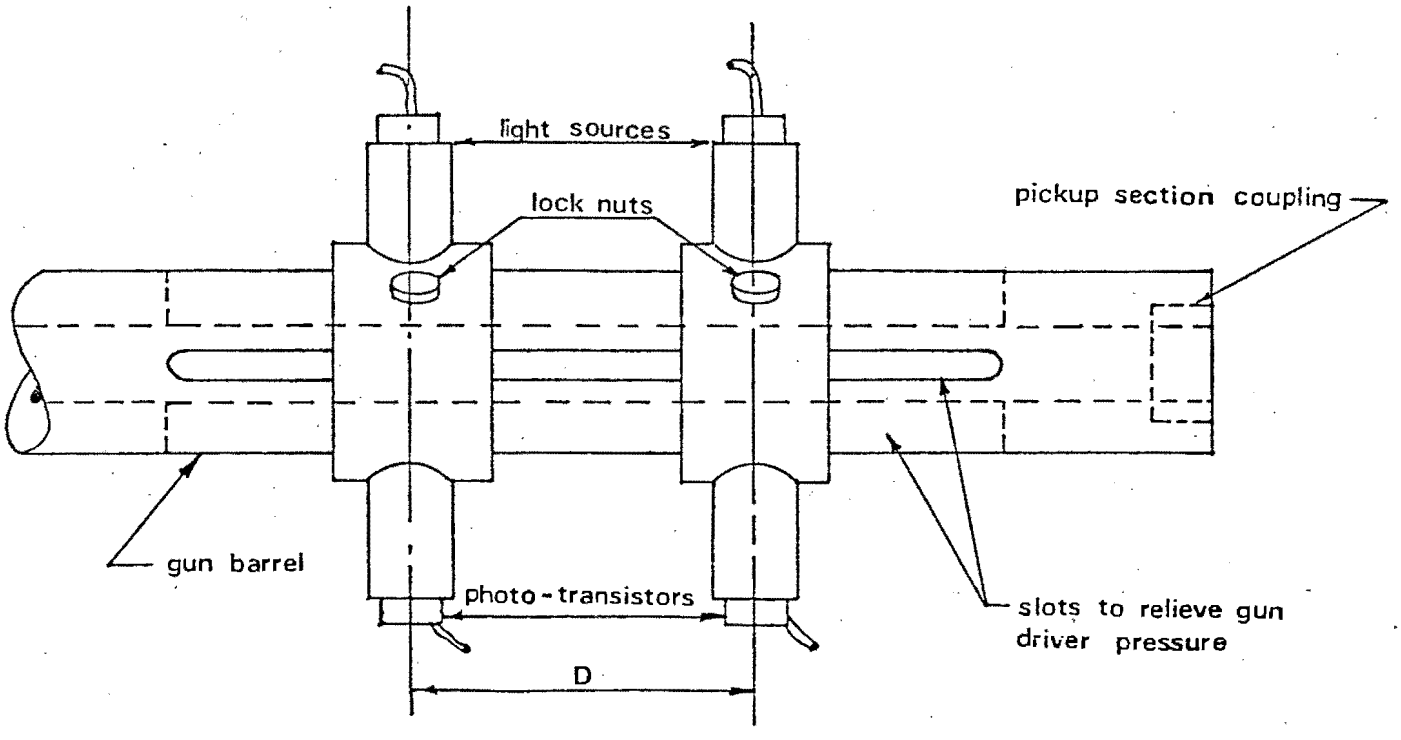

Fig. 5.14 Approach velocity measuring device

5.25 SIGNAL PROCESSING INSTRUMENTS

The signal generated in the sensor wire of the projectile is proportional to projectile particle velocity and to derive deceleration and displacement-time relations, it is differentiated and integrated electronically.

In the present work the differentiated signal is of prime importance as it leads directly to the required penetration force-time histories. Once this information has been recorded, it is a simple matter to derive the required lower derivatives and thus produce force-displacement traces. This would appear to make the electronically integrated response redundant but it is useful to record this parameter directly, since, if a digital recorder is available, it is possible to display deceleration-displacement traces immediately after the penetration has been monitored. Traces of this kind are closely related to force-displacement traces and provide a powerful experimental tool by which the merits and characteristics of a particular target configuration can be ascertained.

In the current work which is primarily concerned with quantitative results, only the differentiated data has been used, but for completeness the constructional details of the integrator have also been included. The general layout of the system is shown in Fig. 5.15 and details of the circuitry are presented in App. C.

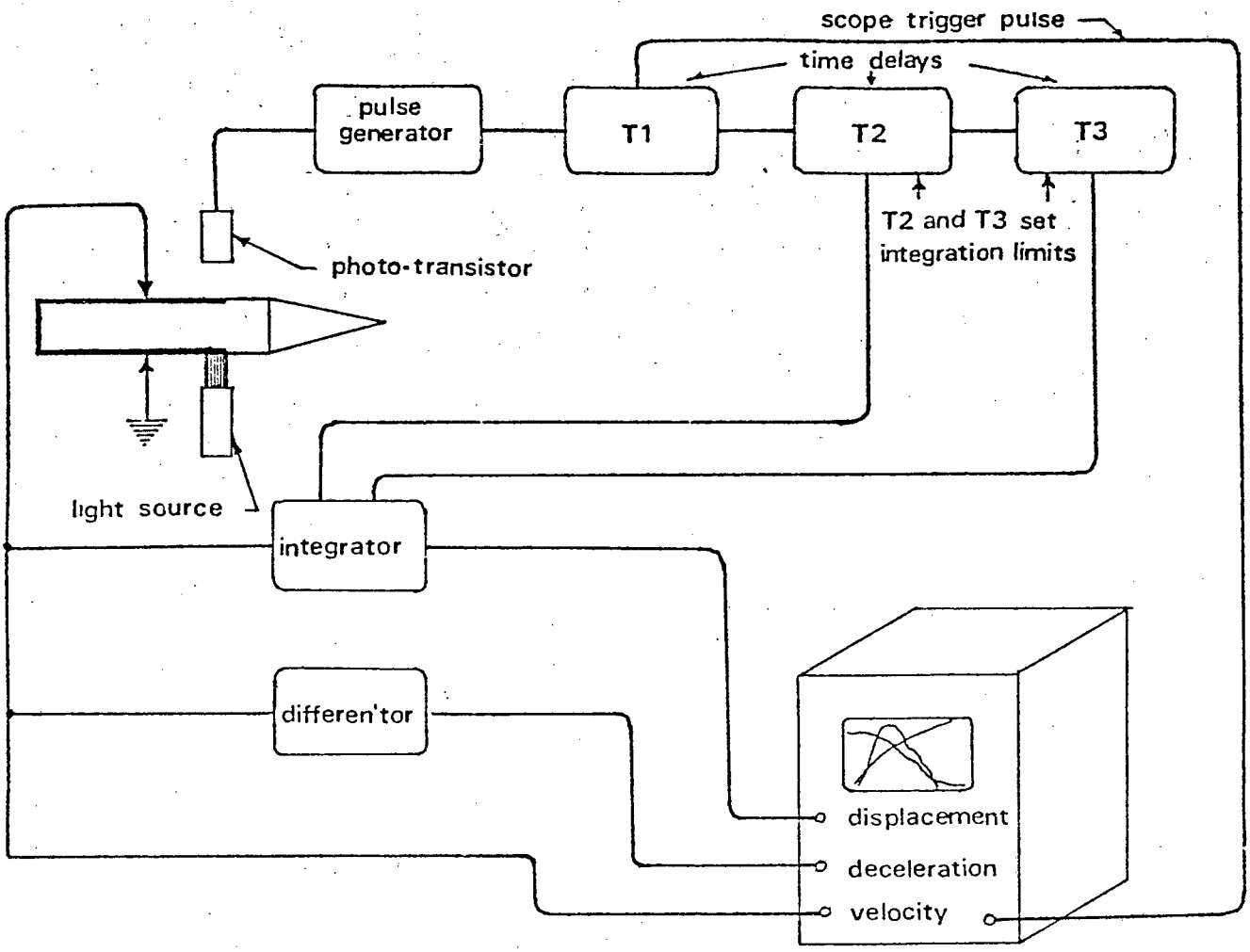

Fig.5.15 Schematic layout of the electronic processing instruments

Fig. 5.16 illustrates the pulsing sequence necessary to co-ordinate the velocity transducer and the oscilloscope. Whereas the velocity and deceleration channels can be switched on before the impact occurs, the integrator must be started and stopped at the desired limits since it is a summing device. LT 1 and LT 2 can be selected by graduated dials on the integrator control panel.

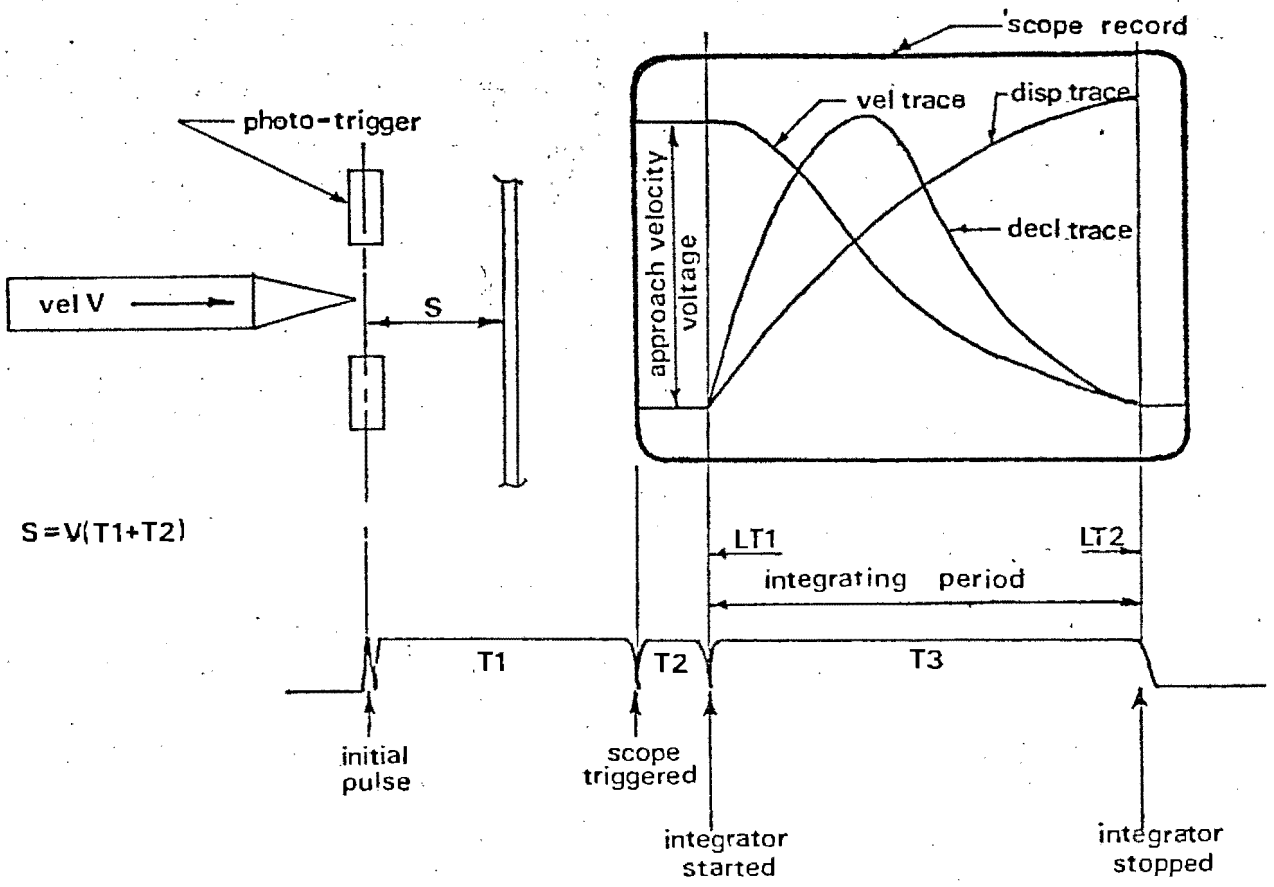

Fig. 5.16 Pulsing sequence

Photo 5.1 The force monitoring projectile with its range of heads. Note the partially inserted commutator wires.

Photo 5.2 Rear view of the field magnet showing the slotted section of gun barrel and the photo-electric device used to measure the projectile approach velocity.

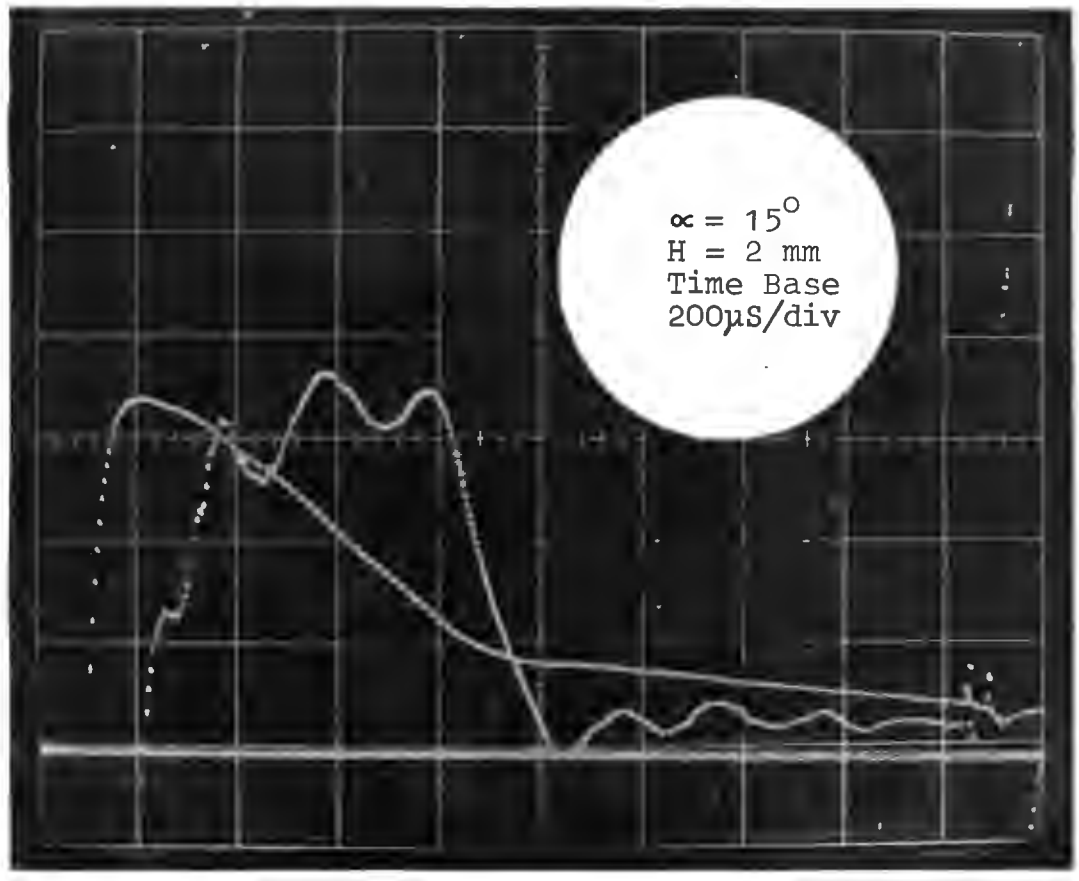

Photo 5.3 The oscilloscope traces representing projectile particle velocity and deceleration. Note the projectile's vibratory component on the latter.

Photo 5.4 The field magnet and pickup section showing the scratch pickups and photo-electric pulse generator.

5.3 TARGET MONITORING APPARATUS

5.3.1 MONITORING RADIAL EXPANSION OF THE INNER ZONE

5.3.1.1 PRINCIPLE OF THE METHOD

The method developed here is based on the fact that the Inner-Outer Zone boundary is defined as the limit of the projectile-target contact area. This contact phenomenon is used in the electrical sense to record the movement of the target material down the conical face of the projectile head.

Special projectile heads were constructed in the form of a series of insulated discs, as shown in Fig. 3.17, which are electrically inter-connected by means of 1KΩ resistors.

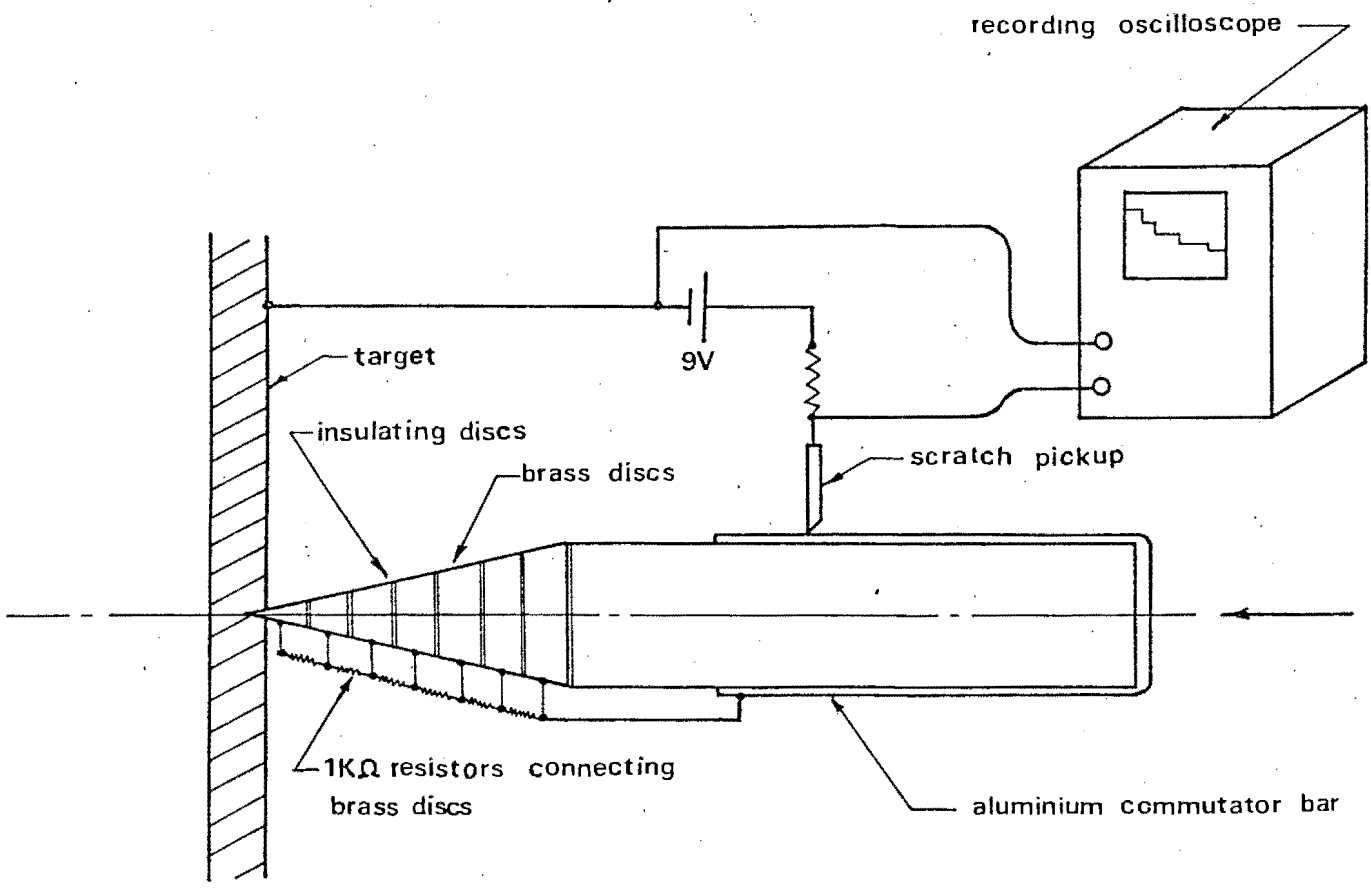

Fig. 5.17 Schematic representation of the method used to monitor Inner Zone radial expansion

On first striking the target, all resistors are connected in series with the circuit shown, but are successively short-circuited as the penetration proceeds. As each segment in the projectile head is traversed therefore, the current flowing in the circuit changes in a step-wise manner. These changes are recorded on a storage oscilloscope and produce a record of the Inner Zone radial expansion as a staircase waveform.

5.3.1.2 PROJECTILE CONSTRUCTION

Practical details of the method are shown in Fig. 5.18

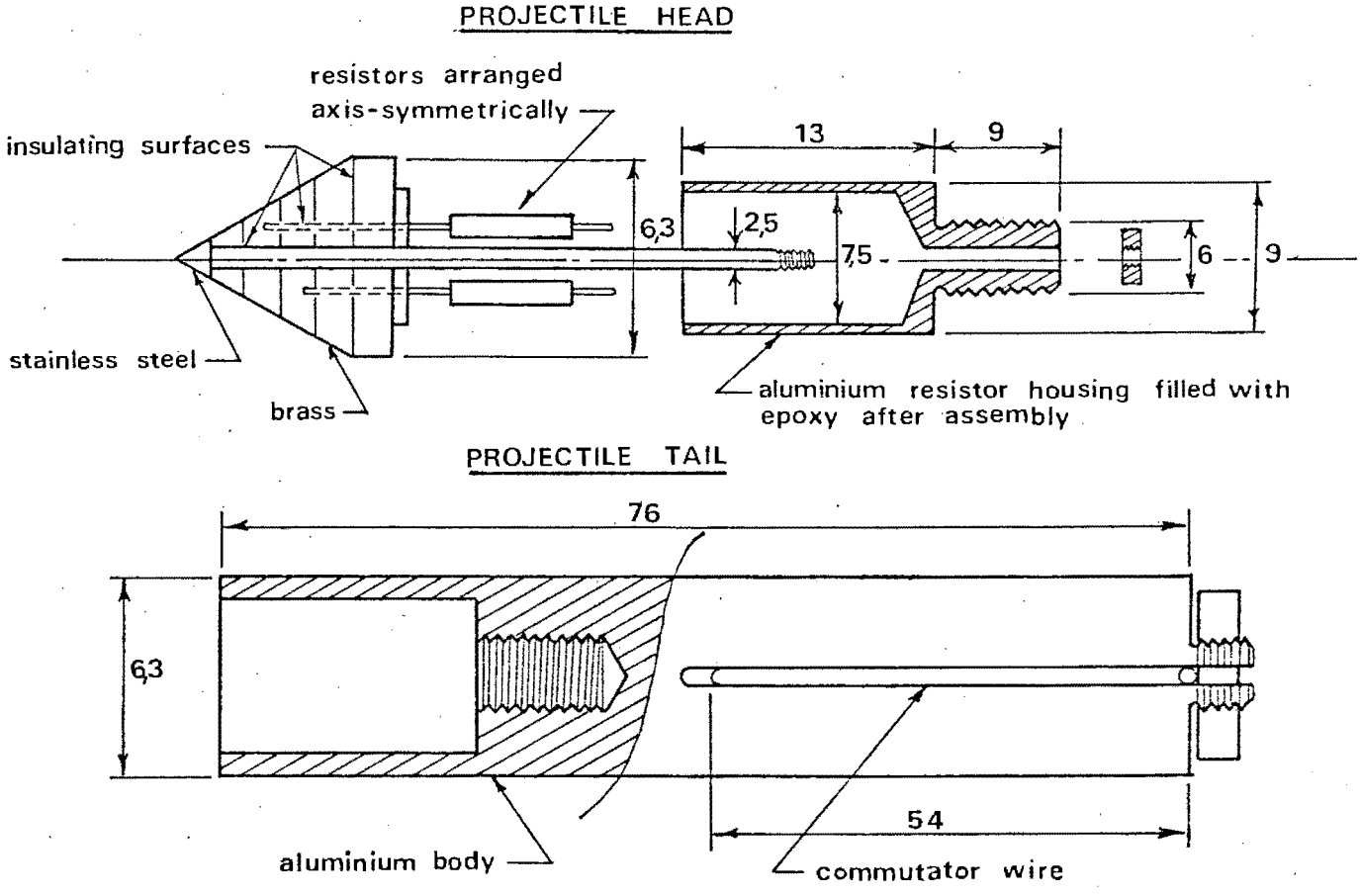

Fig. 5.18 Construction details

The segmented projectile head is constructed from brass with electrical insulation being provided by o,1 mm thick acetate sheet. The central rod and tip of the projectile are made from stainless steel. Each segment in the head has an insulated copper wire connected to it, which passes axially through the remaining segments to the resistor housing at the base of the conical structure. The 1/8 Watt resistors are soldered to these wires to form a series connection - the first being connected to the stainless steel tip and the last to the aluminium body of the projectile. The commutating method described in Section 5.2.2 is used to complete the circuit. After assembling the electrical components, the resistors are cast in an epoxy resin inside an aluminium housing. This produces a mechanically integral unit which is capable of withstanding the stresses of impact.

Five such projectile heads were constructed of semi-cone angles 15^{o}, 30^{o}, 45^{o}, 60^{o} and 75^{o}. For the more acute projectiles (15^{o}, 30^{o}, 45^{o}) it was possible to construct heads using five segments. This effectively gives six data points for the $r_{o}(t)$ trace. For the more obtuse projectiles construction difficulties limited the number of segments to three. Since $r_{o}(t)$ traces for obtuse projectiles are practically linear however, this is not a serious limitation.

5.3.1.3 CALIBRATION

The radial distances corresponding to the changes in electrical resistance, were found by means of the apparatus shown in Fig. 5.19

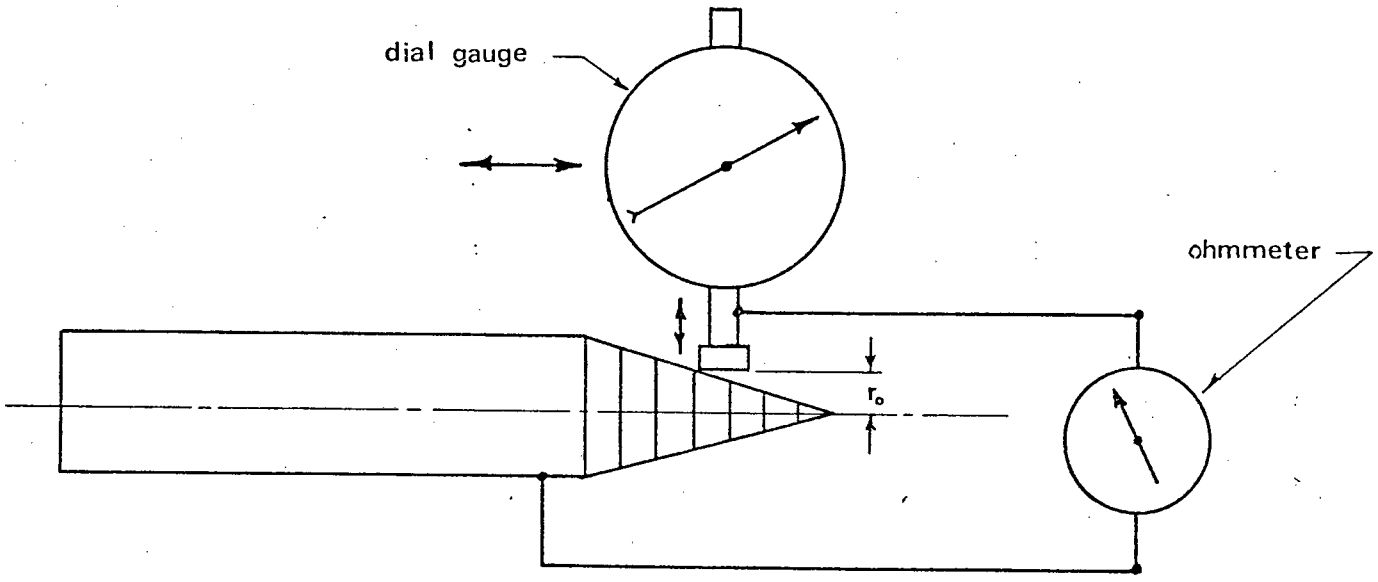

Fig. 5.19 Calibration of the projectile segments

Using a dial gauge to measure radial position, the electrical contact was traversed over the conical head surface (using the carriage of a lathe) until a change of resistance was recorded on the ohmmeter. Once located, the radial position of the transition point can be read from the dial gauge.

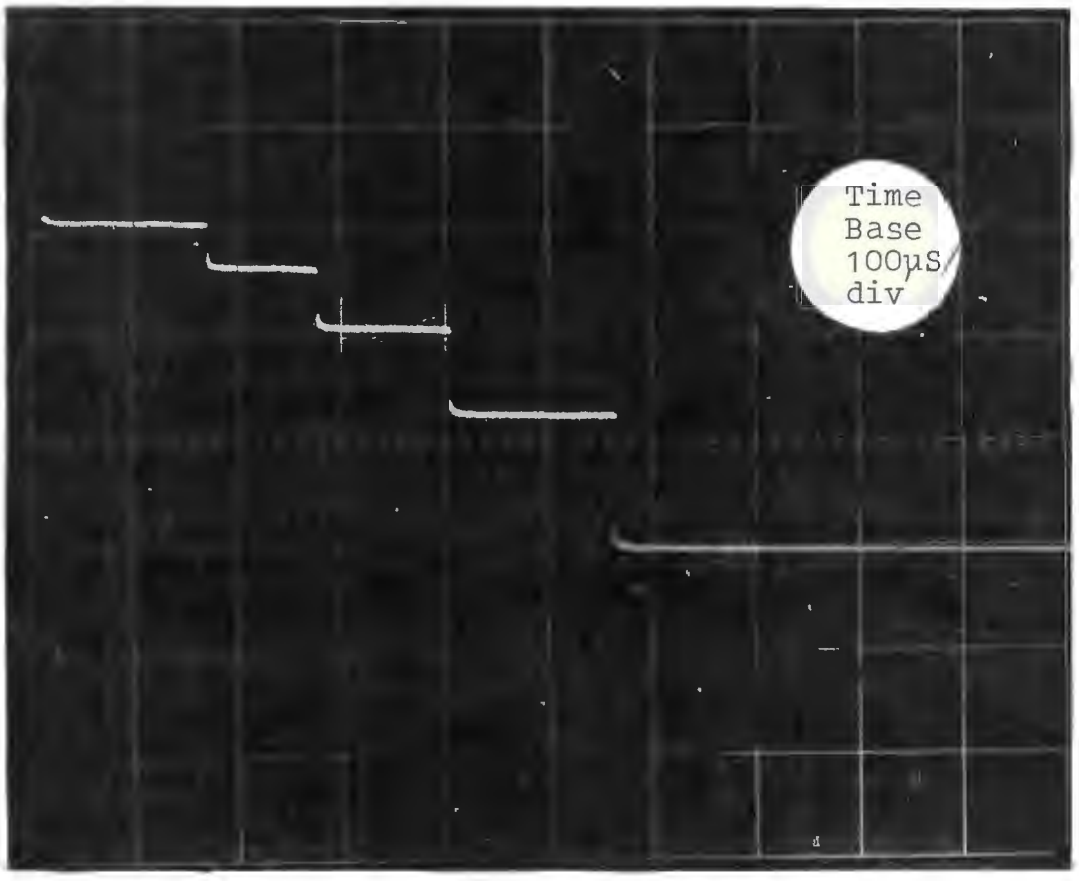

Photo 5.5 A typical staircase wave form recording inner zone radial expansion

Photo 5.6 The projectile used to monitor inner zone radial expansion and its range of segmented heads. Note the partially inserted commutator wire.

5.3.2 MONITORING A SPECIFIC TRANSVERSE MOTION IN THE OUTER ZONE

5.3.2.1 PRINCIPLE OF THE METHOD

Extensive Inner Zone deformation during penetration and perforation complicates the monitoring of the Outer Zone response anywhere near the point of impact. The following method was devised to record Outer Zone transverse velocity 9 mm from the centre of impact.

As was the case with the projectile monitoring system, the method utilises the principle of electro-magnetic induction. A schematic diagram of the method is shown in Fig. 5.20.

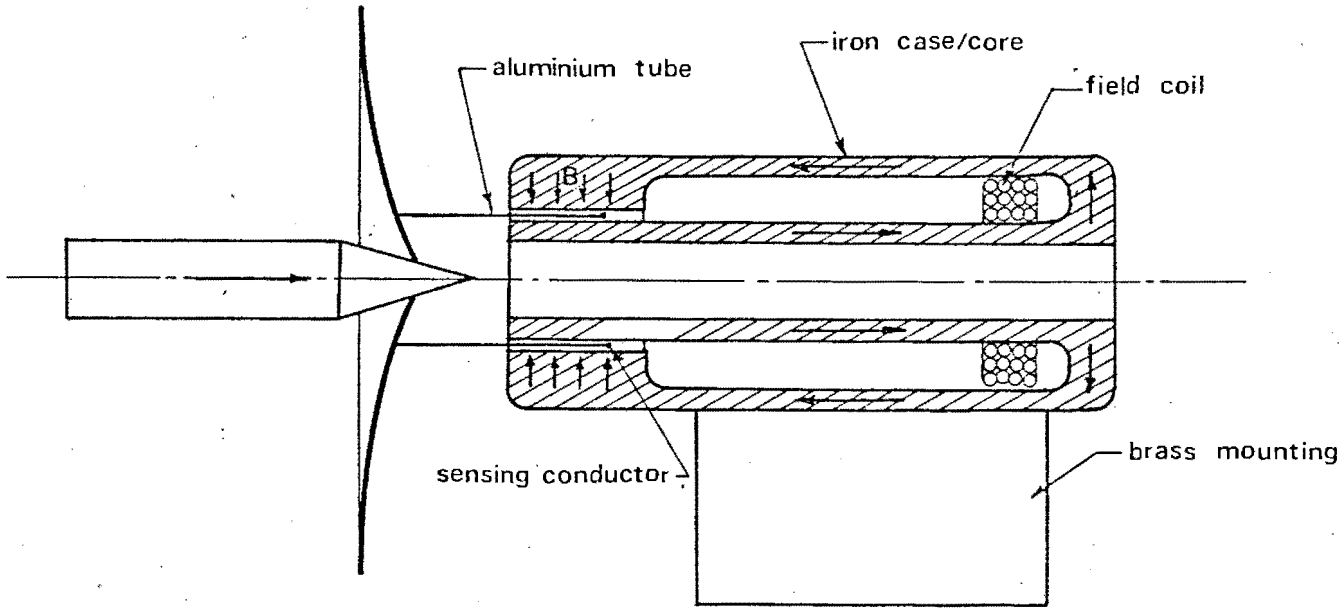

Fig. 5.20 Schematic diagram of the method used to monitor Outer Zone transverse velocity

The system can be likened to that of an electro-magnetic acoustic speaker, though operating in the reverse manner. Instead of electrical energy being converted into mechanical speaker-cone motion, target plate motion is converted into a proportional electrical signal. As with the projectile transducer we have:

$$e = BlV \quad \ldots\ldots\ldots\ldots\ldots\ldots\ldots\ldots \quad 5.1$$

or $$e = K\dot{X}_{dt} \quad \ldots\ldots\ldots\ldots\ldots\ldots\ldots\ldots \quad 5.5$$

where $\dot{X}_{dt}$ is the Outer Zone transverse velocity at the transducer location.

5.3.2.2 CONSTRUCTION DETAILS

An electromagnet of 1500 turns of 0,1 mm diameter copper wire is used to generate the magnetic field. The latter is conducted through the cylindrical soft iron case and core to produce a uniform radial field through which the sensing conductor moves. Mounting is by means of a brass pillar to prevent magnetic leakage to the steel bed of the gun. Should a projectile perforate the target plate, the hollow centre of the field magnet permits its free passage to the "catcher" which is placed directly behind the transducer.

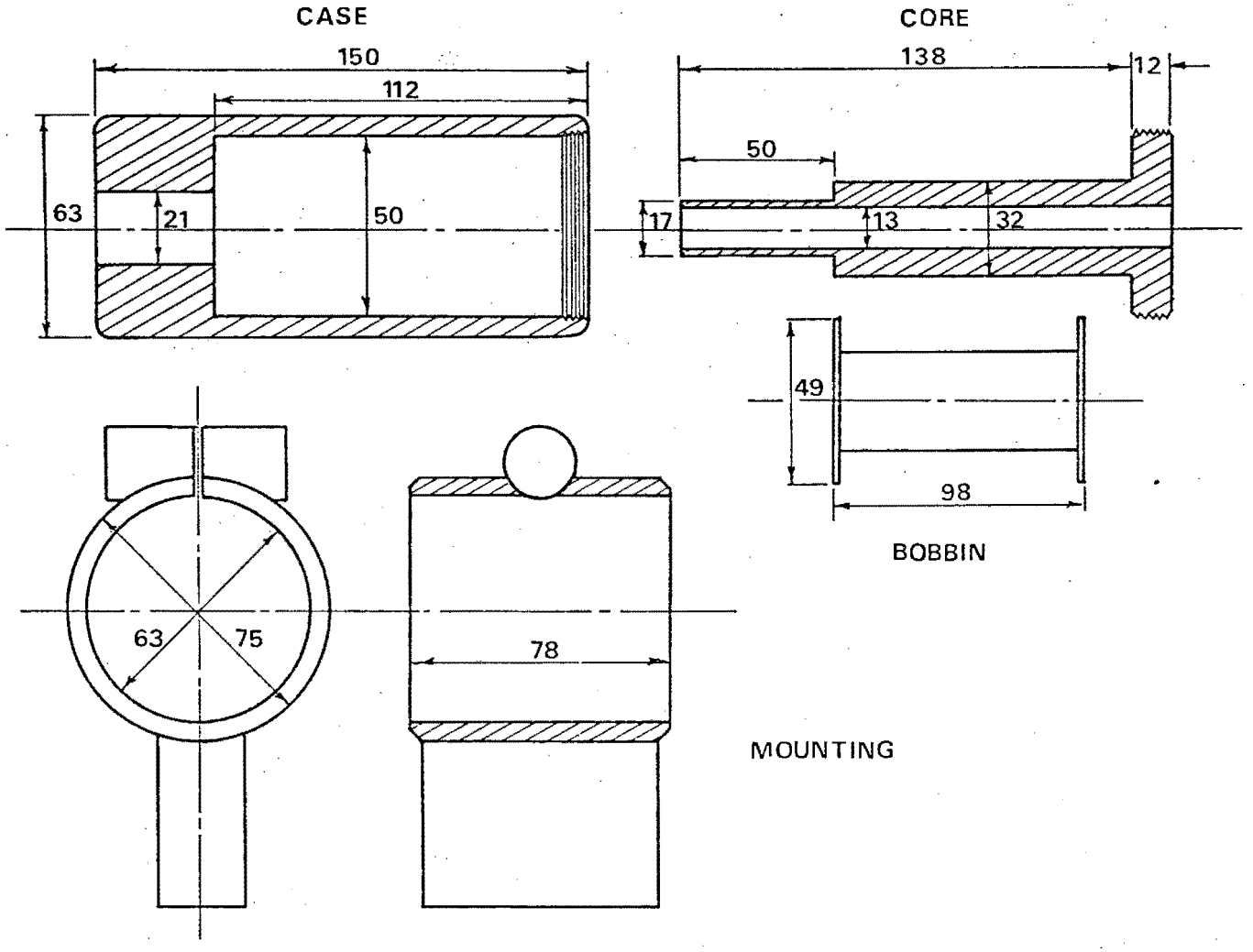

Fig. 5.21 Field magnet and mounting

The sensing conductor is circular and 18 mm in diameter. To permit free travel in the magnetic field, it is attached to the end of a thin aluminium tube with epoxy cement - the opposite end of the tube being soldered to the target plate with a low-temperature aluminium solder. At this joint, the tube is slit axially to allow for any radial expansion of

the plate that may occur and to ensure that the tube's material strength does not inhibit the target deformation process. The total mass of the conductor and tube is only 0,9 g so that body forces associated with it are negligibly small.

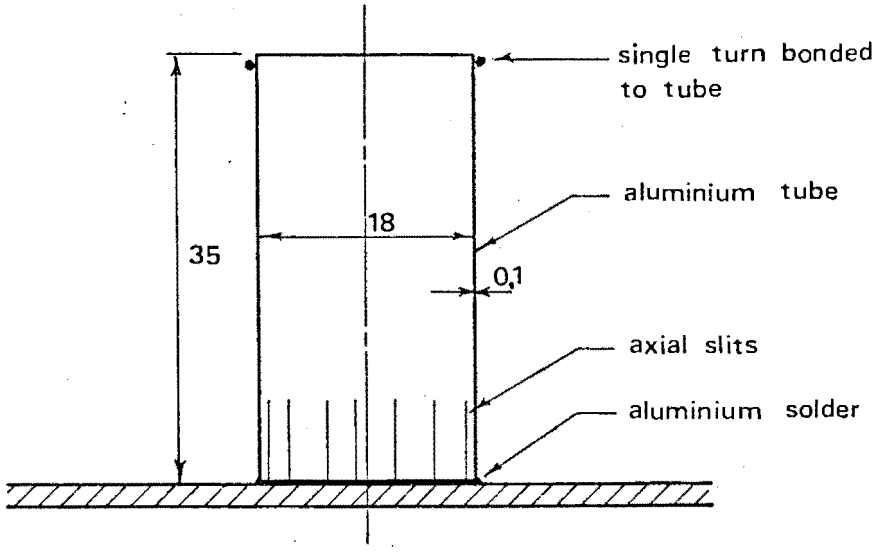

Fig. 5.22 Sensing conductor and mounting

5.3.2.3 CALIBRATION OF THE TRANSDUCER

In the case of the projectile transducer, the calibration constant is determined by measuring the approach velocity and

the initial transducer voltage before impact. Since this cannot be done in the case of the target transducer, a different calibration procedure has been adopted.

Using the apparatus shown in Fig. 5.23 the two transducers are first aligned by imparting an identical sinusoidal motion to each by means of a scotch-yolk mechanism driven by an electric motor. The output from the projectile transducer is displayed directly on an oscilloscope screen while that from the target transducer first passes through a variable gain amplifier. By adjusting the gain of the amplifier, the two traces can be aligned so as to have the same transfer constant (K_v). Once this has been accomplished, recorded projectile and target responses can be directly compared and the calibration constant derived for the projectile will apply equally to the target trace.

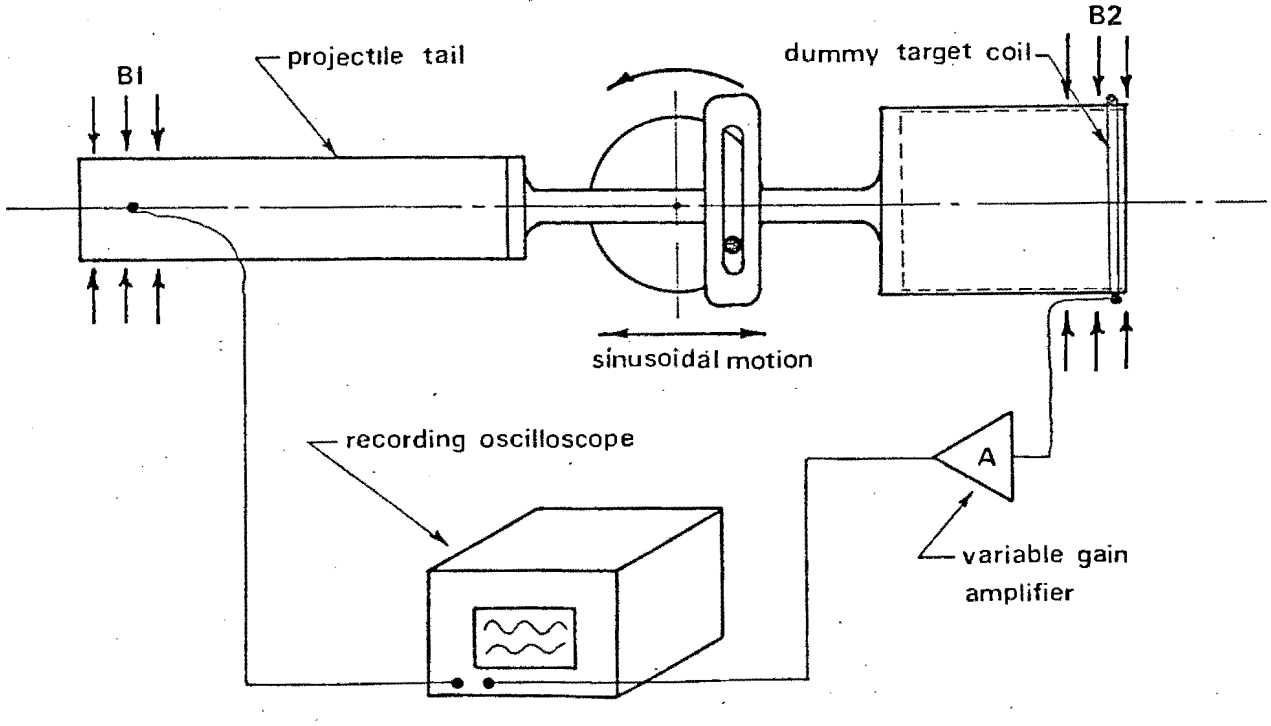

Fig. 5.23 Aligning the projectile and velocity transducers

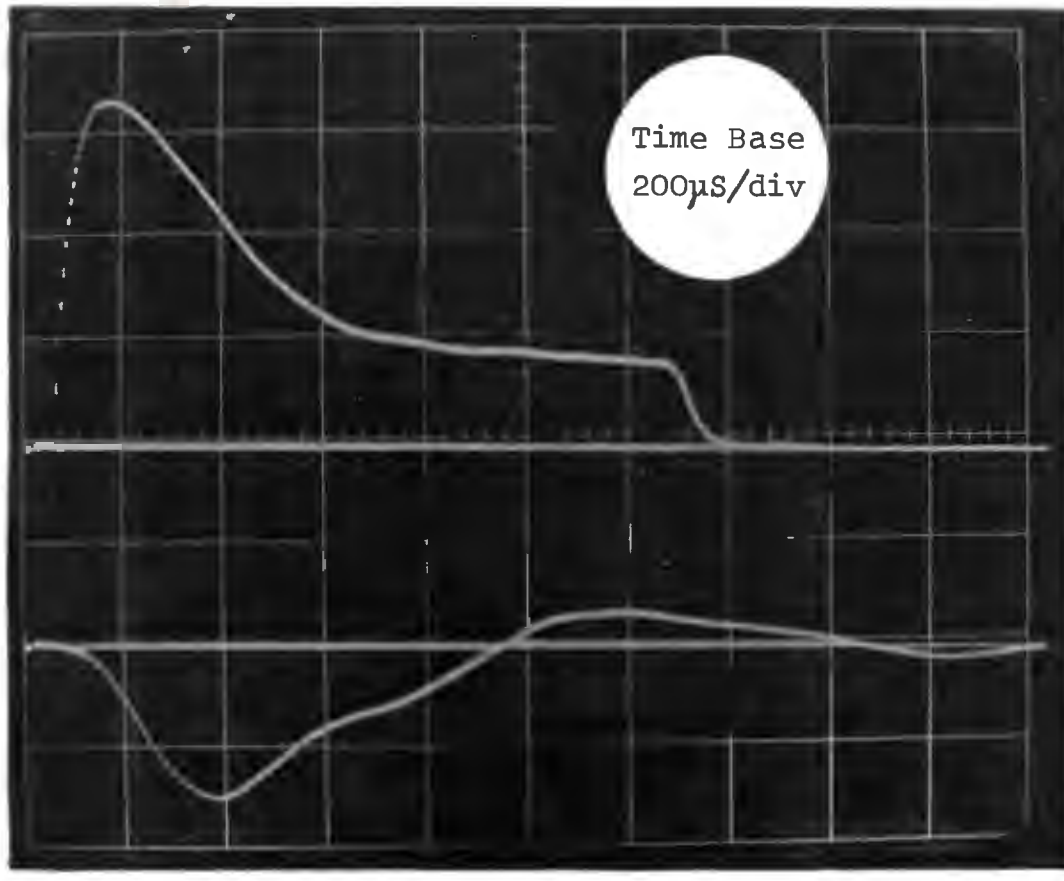

Photo 5.7 A typical oscilloscope record of the projectile velocity time trace (upper) and inverted target velocity time trace (lower). Note the elastic recovery in the target and subsequent vibration.

Photo 5.8 Rear view of the target transducer field magnet and mounting

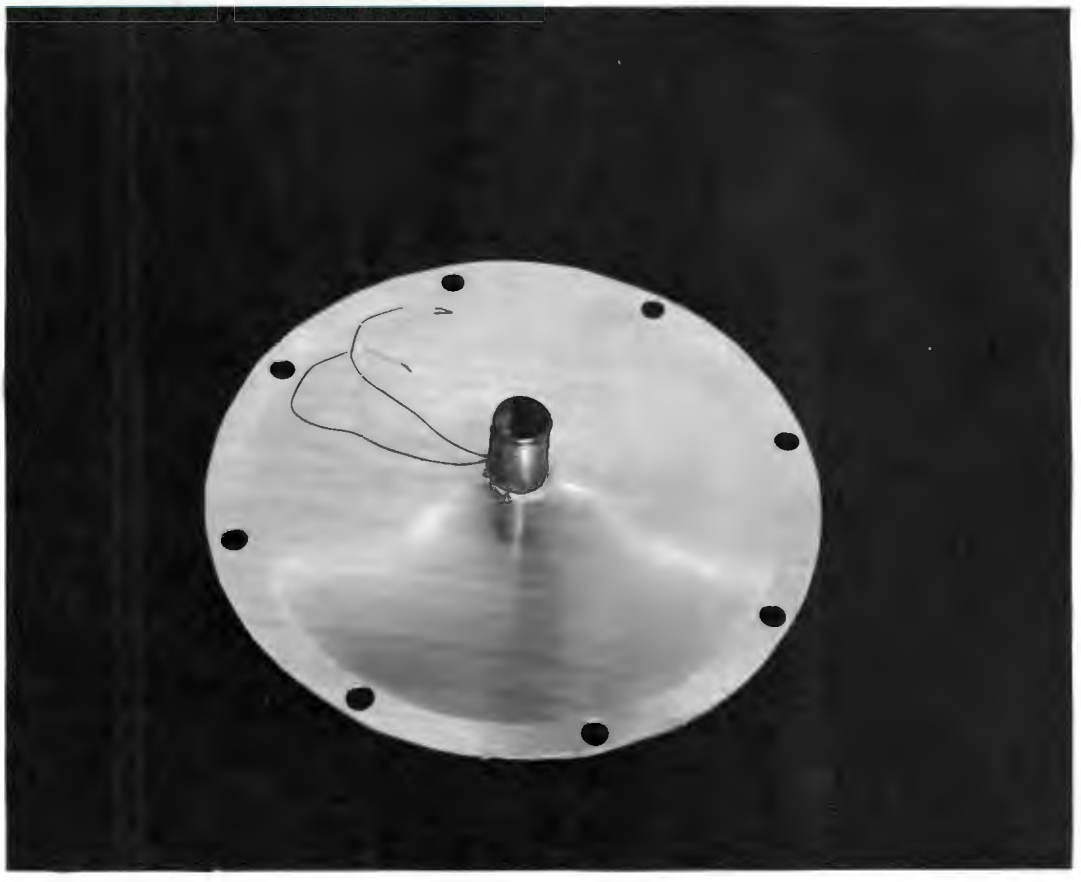

Photo 5.9 An impacted plate showing the sensing conductor and mounting tube

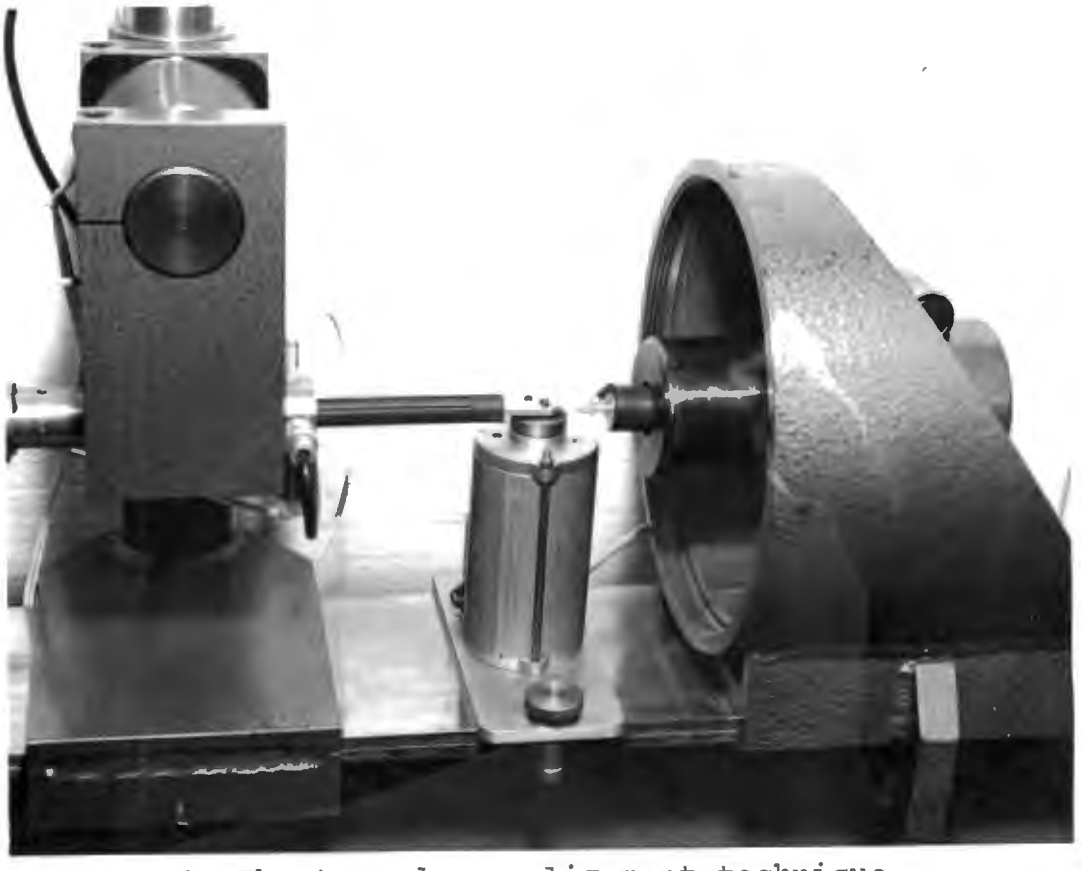

Photo 5.10 The transducer alignment technique. The electric motor mounted centrally gives the projectile transducer (left) and target transducer (right) an identical sinusoidal motion.

CHAPTER 6

RESULTS

6.1 INTRODUCTION

The present study has approached the penetration problem from the concept of a penetration force (F) and its displacement (X) - the two parameters being related by the equation:

$$E = \int F dX \quad \ldots\ldots\ldots\ldots\ldots\ldots\ldots\ldots \quad 2.1$$

The results presented in this chapter are therefore mainly concerned with the experimental recording and analytical description of penetration force-displacement histories. To supplement this, it has proved instructive to dissect the penetration process using the analysis developed in Chapt. 3. This provides added insight into the nature of F-X histories and the distribution of penetration energy in the target plate.

To obtain a wide range of impact conditions, five different conical projectile heads were used, with α the semi-cone angle varying from 15° to 75°, and in addition, three thicknesses (1 mm, 1,6 mm, 2 mm) of aluminium target plate (Alcan 2HS4) were investigated. Standardisation of the impacts was achieved by holding the projectile mass constant at M = 0,032 kg for the entire range of projectile heads and by

considering only the limiting case of containment for each recorded impact.

6.2 EXPERIMENTAL F-X TRACES

The penetration force-displacement graphs shown in Figs. 6.1 a, 6.1 b and 6.1 c are produced using the projectile monitoring apparatus in conjunction with the projectile analysis described in Chapt. 4. Primary data is recorded from deceleration-time traces (see photo 5.3) by measuring the trace co-ordinates with a travelling microscope and reduced by means of a computer program which is based on the analysis of Chapt. 4. This data reduction procedure is presented in App. D.

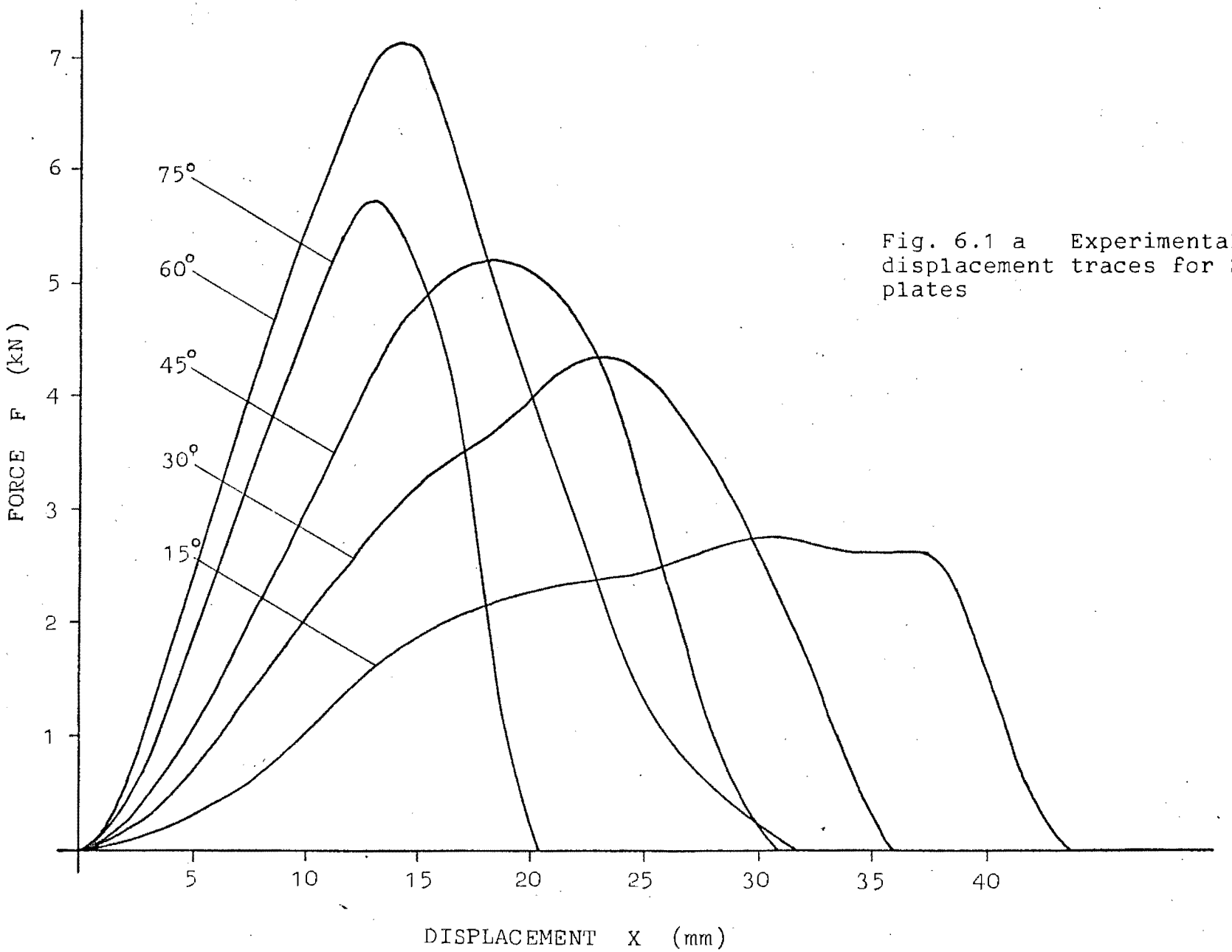

Fig. 6.1 a Experimental force-displacement traces for 2 mm thick plates

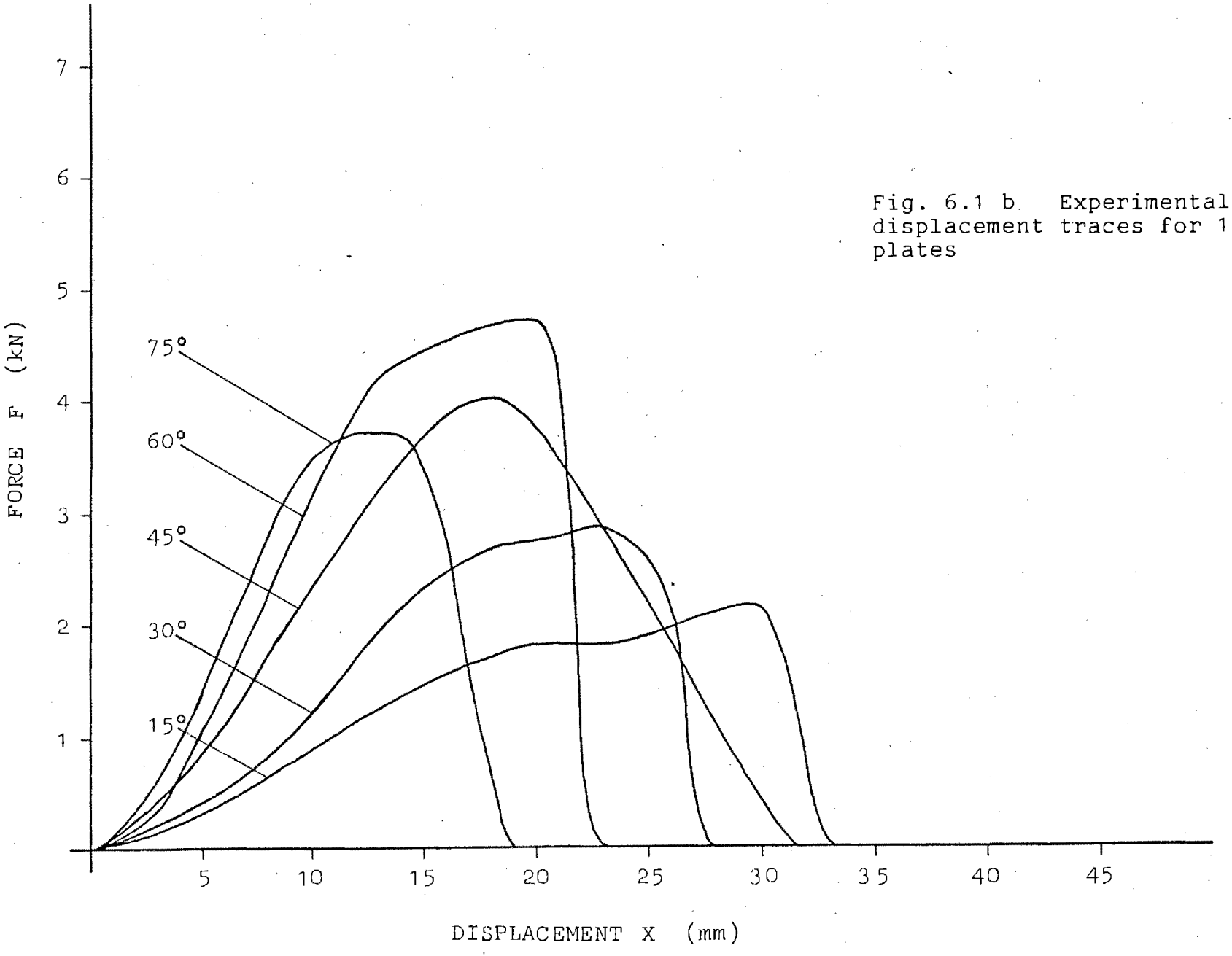

Fig. 6.1 b Experimental force-displacement traces for 1,6 mm thick plates

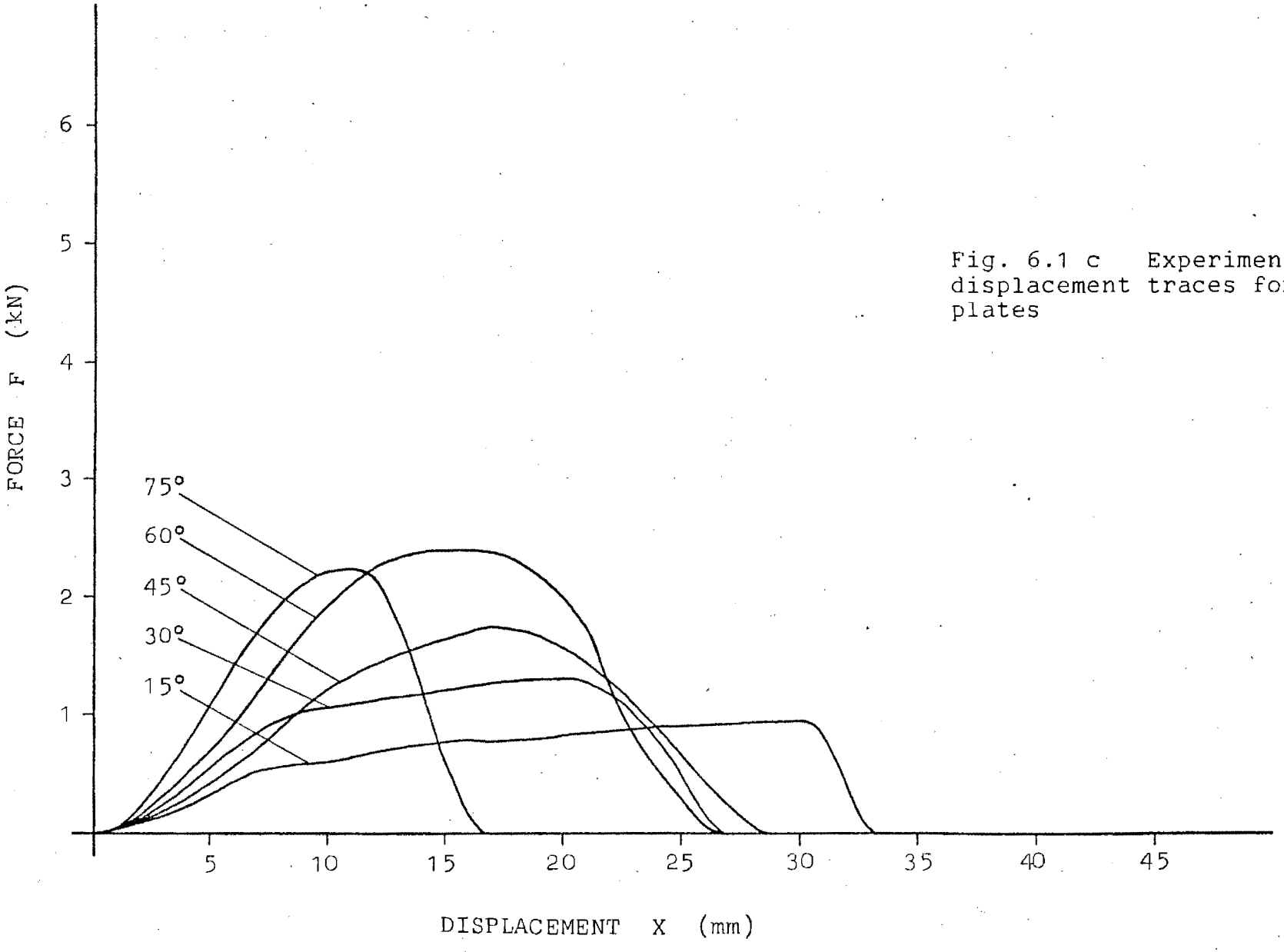

Fig. 6.1 c Experimental force-displacement traces for 1 mm thick plates

6.3 MODELLED F-X TRACES AND THEIR COMPARISON WITH THE EXPERIMENTAL RESULTS

The penetration model developed in Chapt. 3 assumes a sufficiently thin target plate so that thickness effects can be neglected. In the present study only the 1 mm target plate can be considered thin in this respect, the lateral stiffness of the 1,6 mm and 2 mm thick plate being such that the membrane analysis cannot account for the magnitudes of the recorded force-displacement histories without assuming an abnormally high target yield stress. For this reason all derived data is based solely on the 1 mm target plate impacts.

To use the penetration model described in Chapt. 3 it is necessary to find certain parameters empirically and some must be assumed. The stratagem adopted in this regard has been to model the analytical curves as closely as possible to their experimental counterparts. The values taken on by these parameters using this procedure are presented in the table below and will be discussed in Chapt. 7. The modelled F-X traces are presented in Fig. 6.3 along with a superimposed transparency of the experimental results.

α	r_o (mm)	θ_o	σ_p^*/Y	† σ_s^*/Y	
15°	1,4	42°	0,55	——	† μ=0,1 H=1mm Y=119MN/m^2
30°	2,6	35°	0,31	——	
45°	4,0	31°	0,20	——	
60°	——	—	0,15	0,30	
75°	——	—	0,15	0,30	

† Assumed value

Fig. 6.2 A comparison between modelled and experimental force-displacement traces

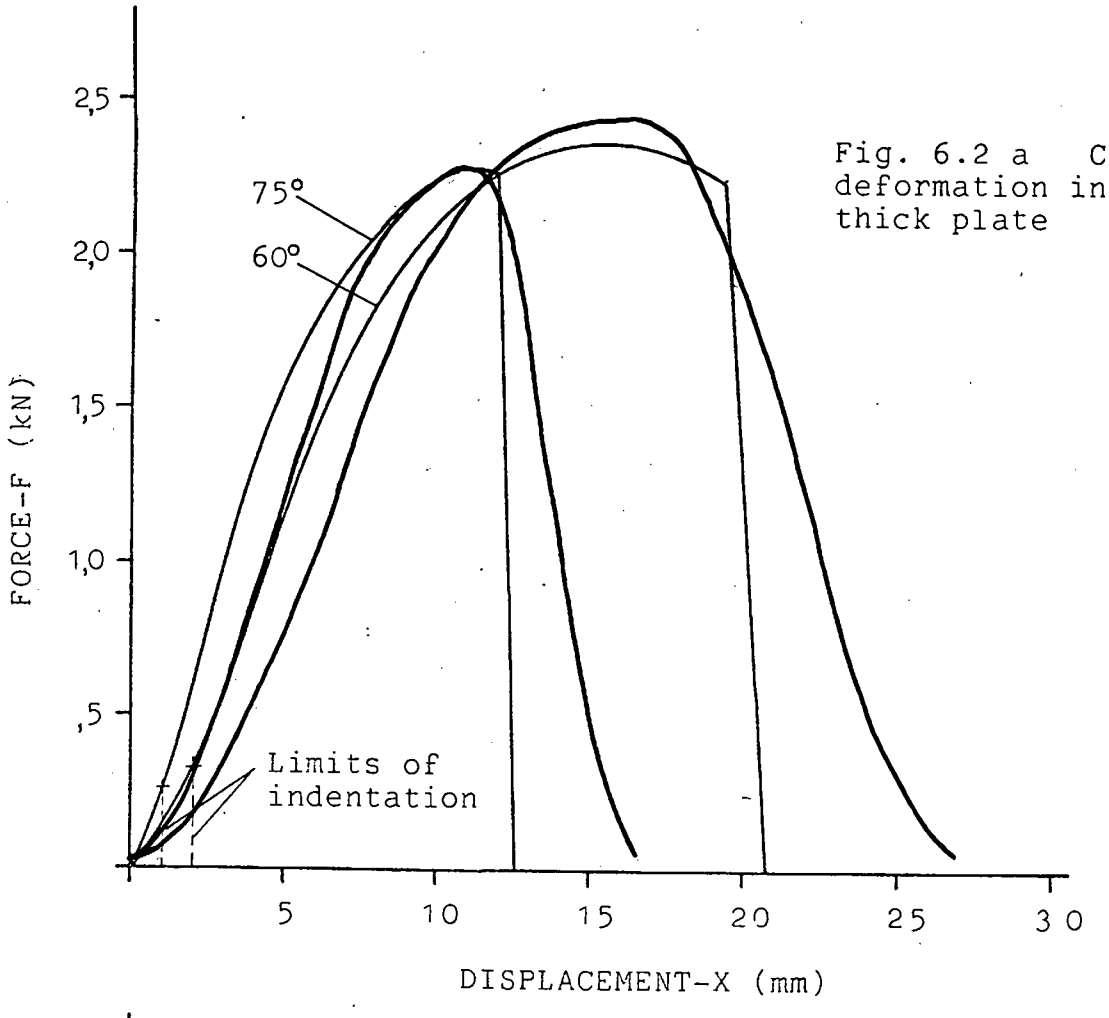

Fig. 6.2 a Conic deformation in 1 mm thick plate

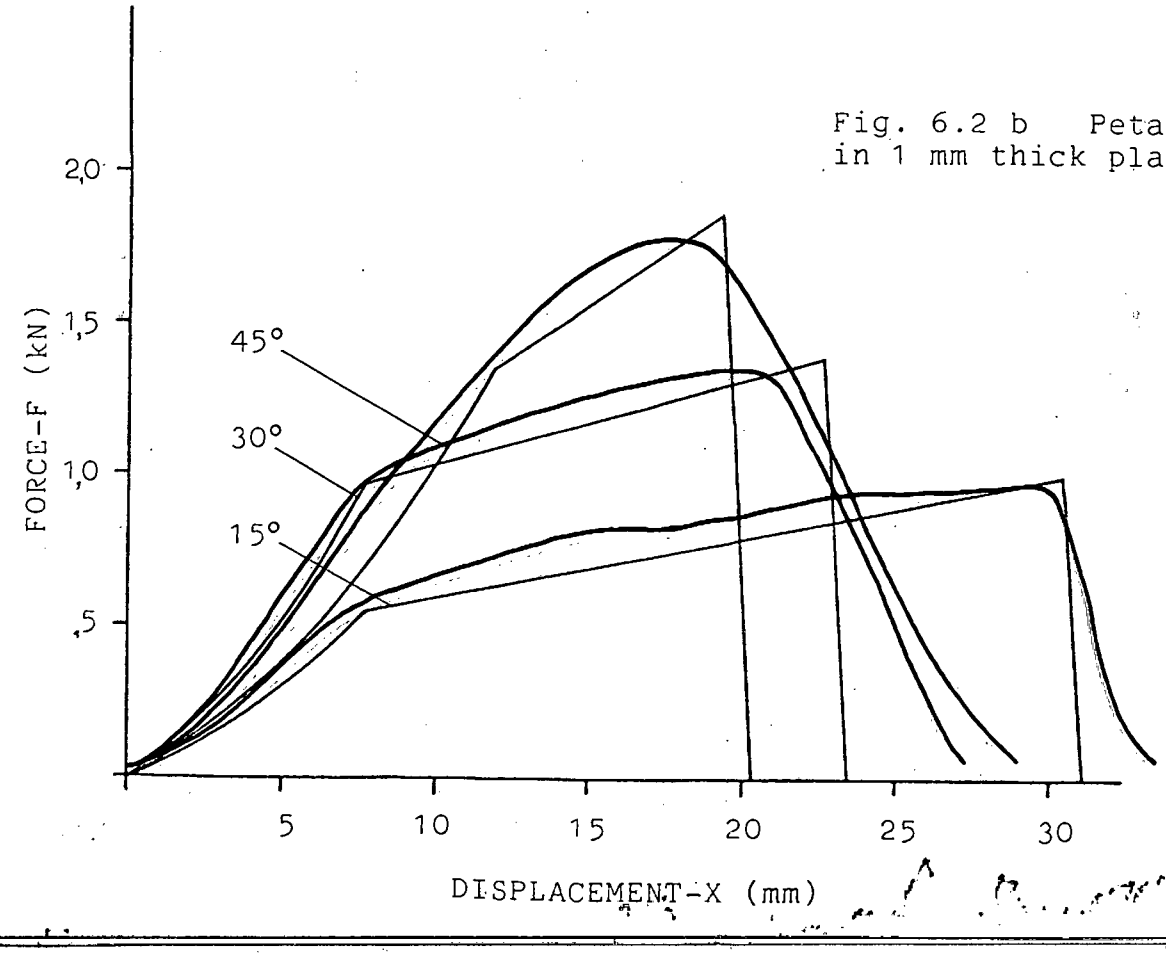

Fig. 6.2 b Petalling in 1 mm thick plate

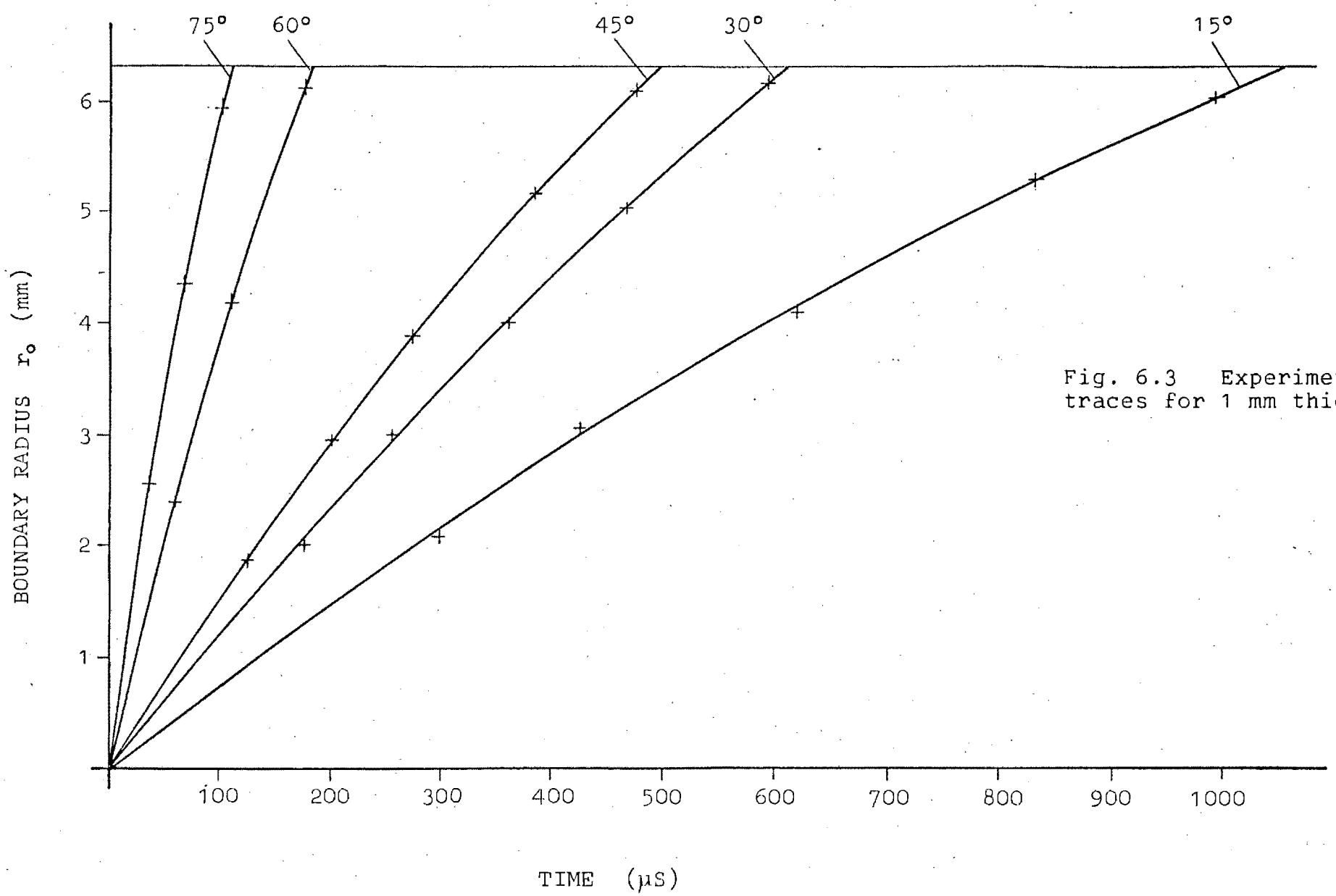

Fig. 6.3 Experimental r_o-t traces for 1 mm thick plate

Fig. 6.4 Experimental and modelled $r_o - \theta_o$ traces

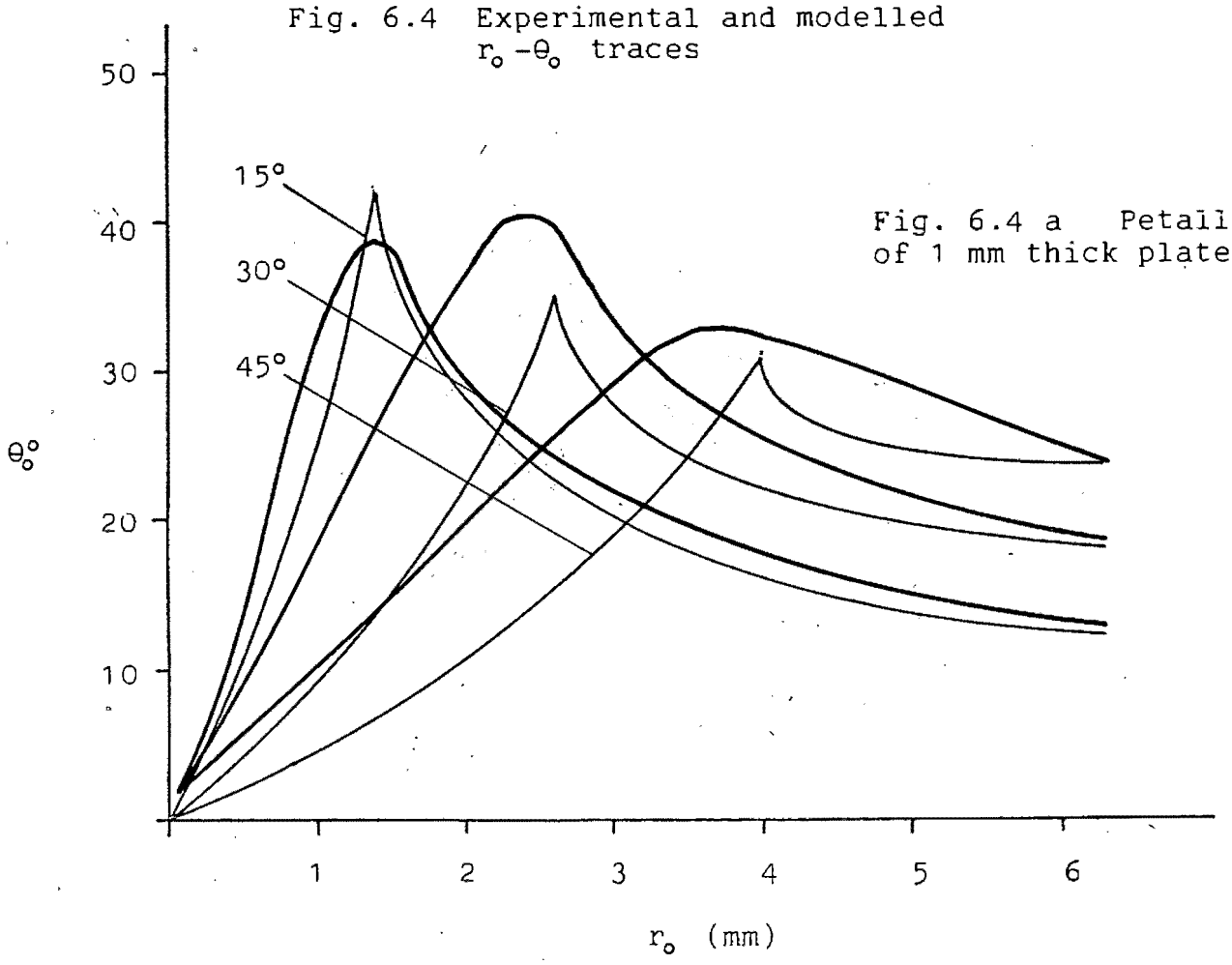

Fig. 6.4 a Petalling of 1 mm thick plate

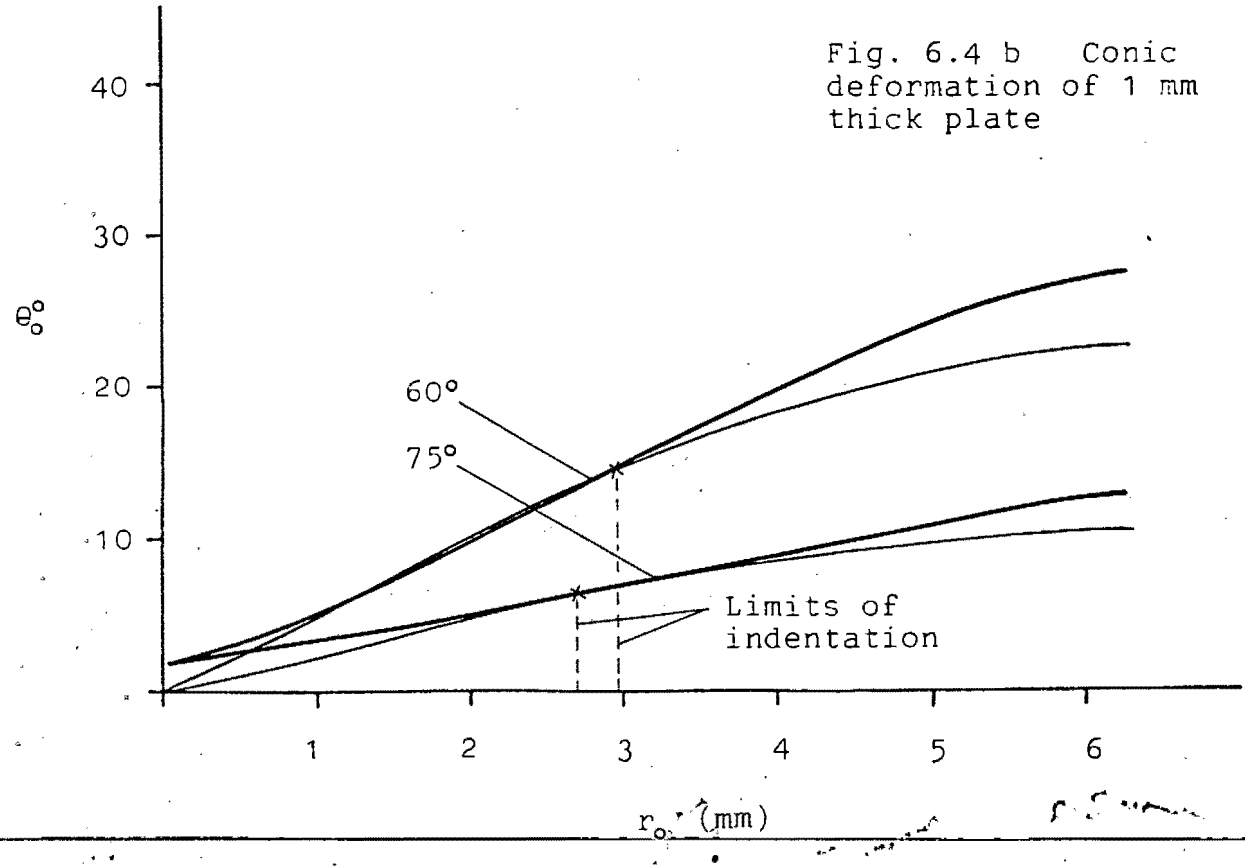

Fig. 6.4 b Conic deformation of 1 mm thick plate

6.6 EXPERIMENTAL INNER AND OUTER ZONE TARGET DISPLACEMENTS

The projectile displacement (X) and target displacements (X_{iz} and X_{oz}) are related by the equation:

$$X = X_{iz} + X_{oz} \quad \ldots\ldots\ldots\ldots\ldots\ldots \quad 2.2$$

and in addition X_{iz} is given by the expression

$$X_{iz} = r_o \cot \alpha \quad \ldots\ldots\ldots\ldots\ldots\ldots \quad 3.35$$

Since $r_o(t)$ and $X(t)$ have been monitored and are known, it is therefore possible to determine the Inner and Outer Zone displacements using these equations. The results obtained for the 1 mm thick plate and the range of projectile heads are presented in Fig. 6.5.

In addition to this, the Outer Zone response which was monitored directly using the apparatus described in Sect. 5.3.3 is shown in Fig. 6.6 and compared with the corresponding modelled responses.

Fig. 6.5 Inner and Outer Zone displacements as a function of time

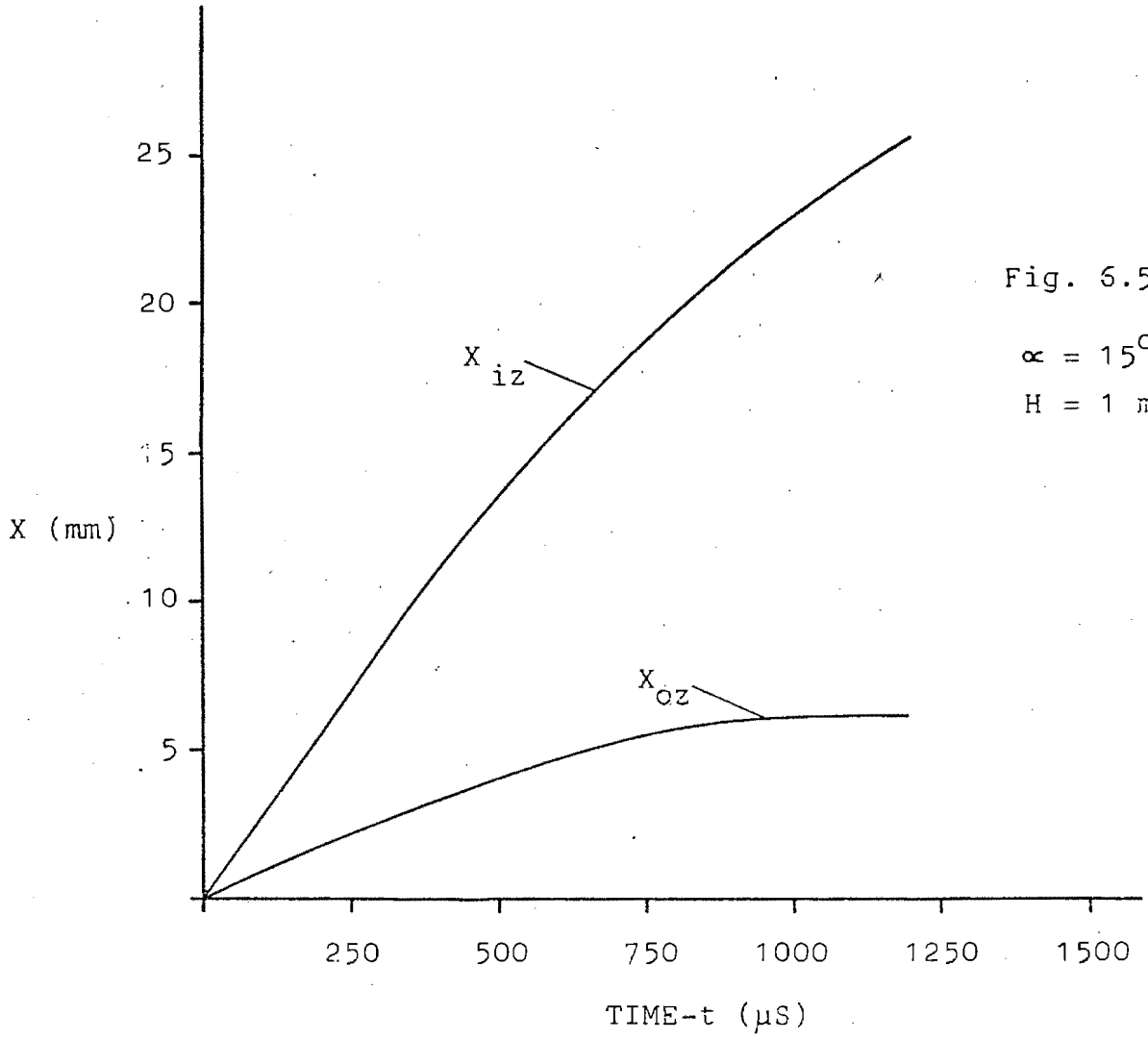

Fig. 6.5 a

$\alpha = 15^{o}$

H = 1 mm

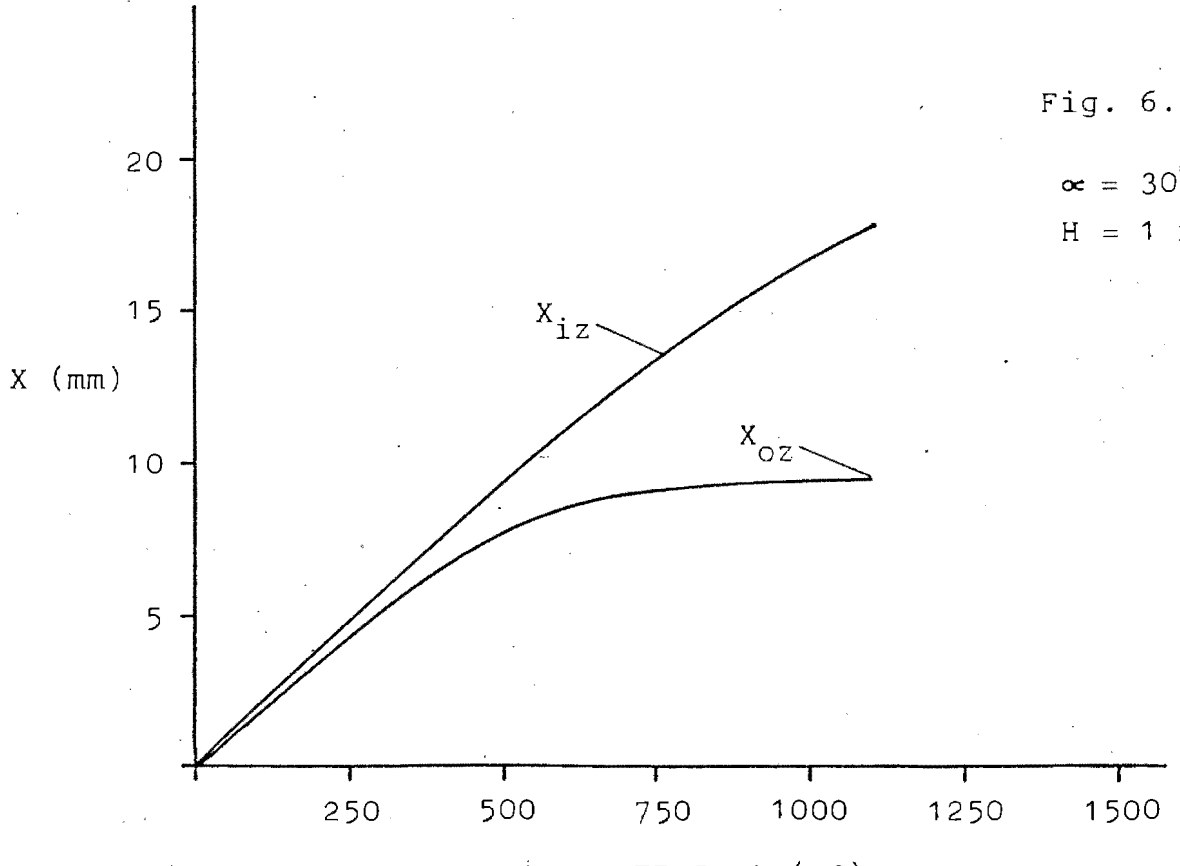

Fig. 6.5 b

$\alpha = 30^{o}$

H = 1 mm

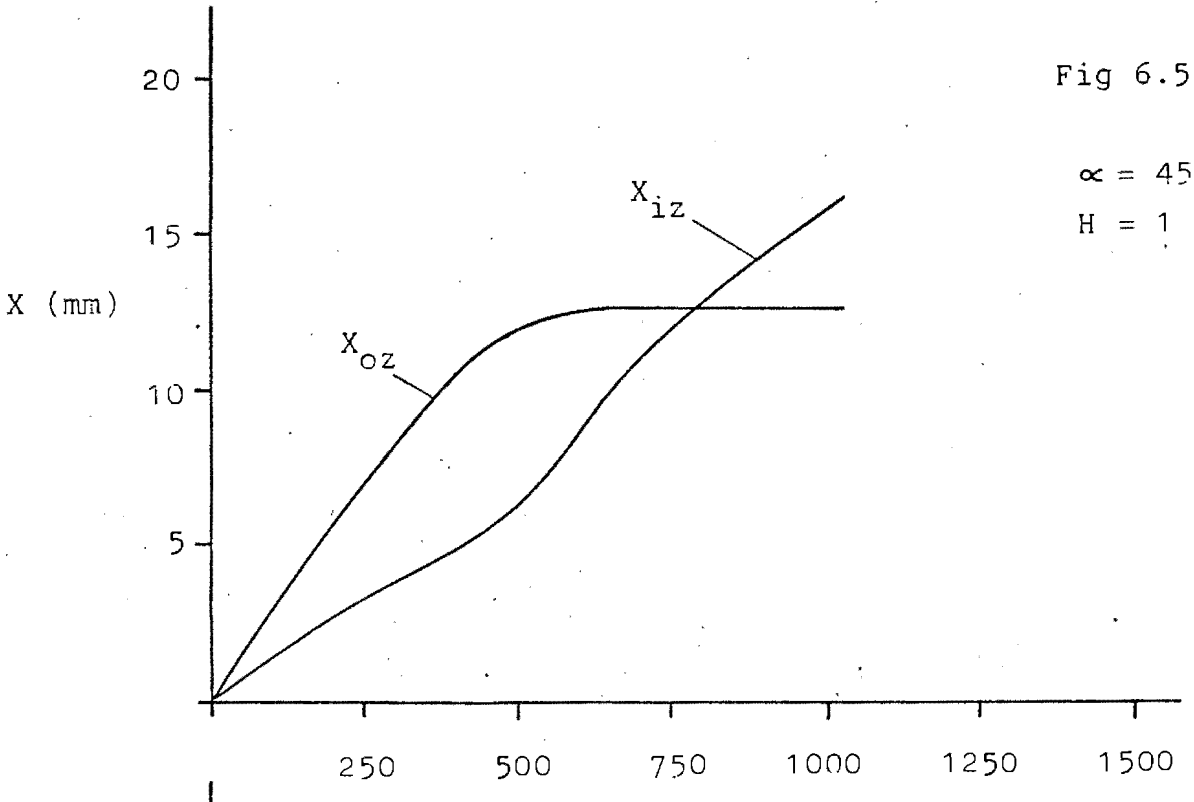

Fig 6.5 c

$\alpha = 45^{\circ}$

H = 1 mm

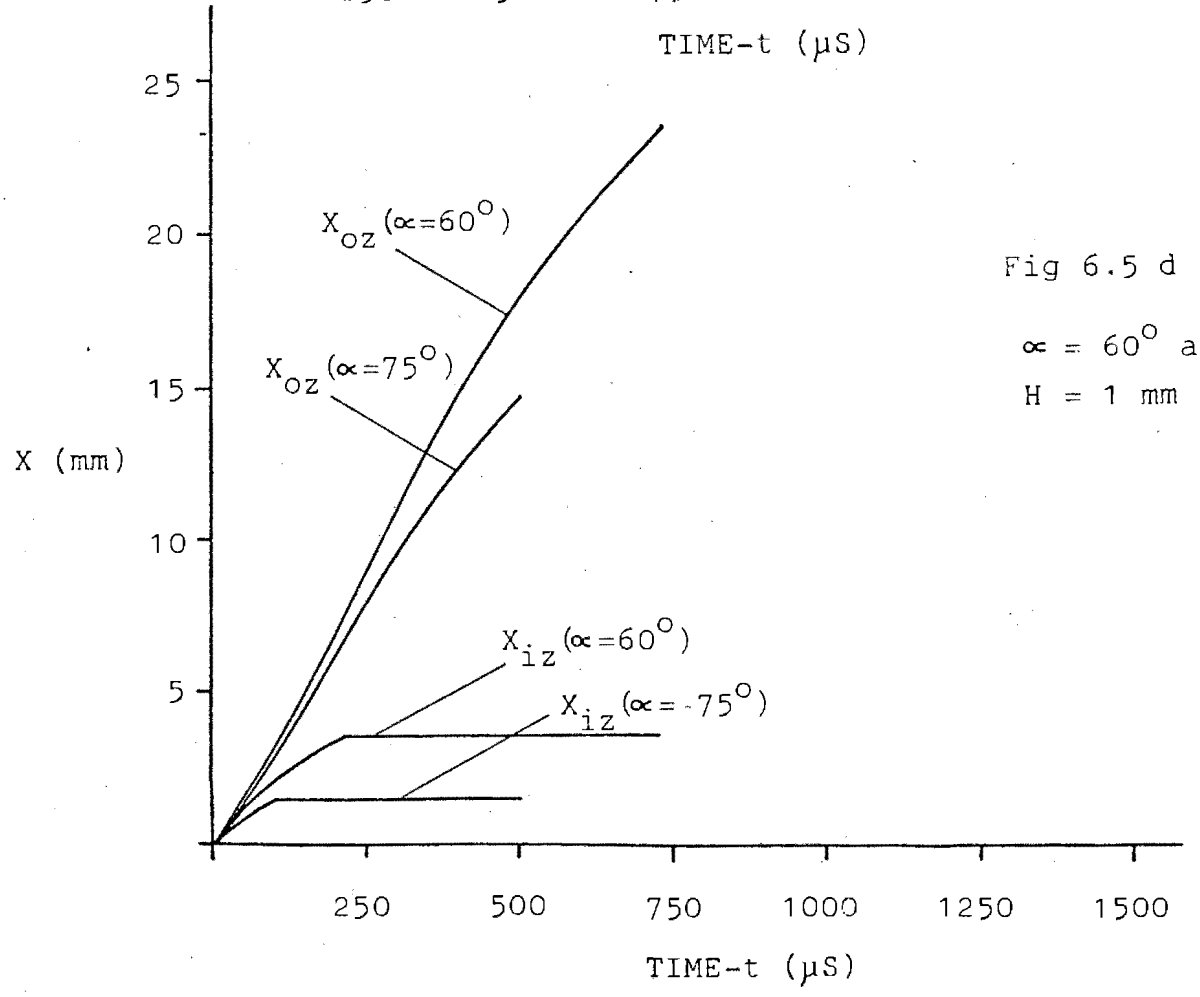

Fig 6.5 d

$\alpha = 60^{\circ}$ and 75°

H = 1 mm

Fig. 6.6 - A comparison between modelled and experimental Outer Zone responses

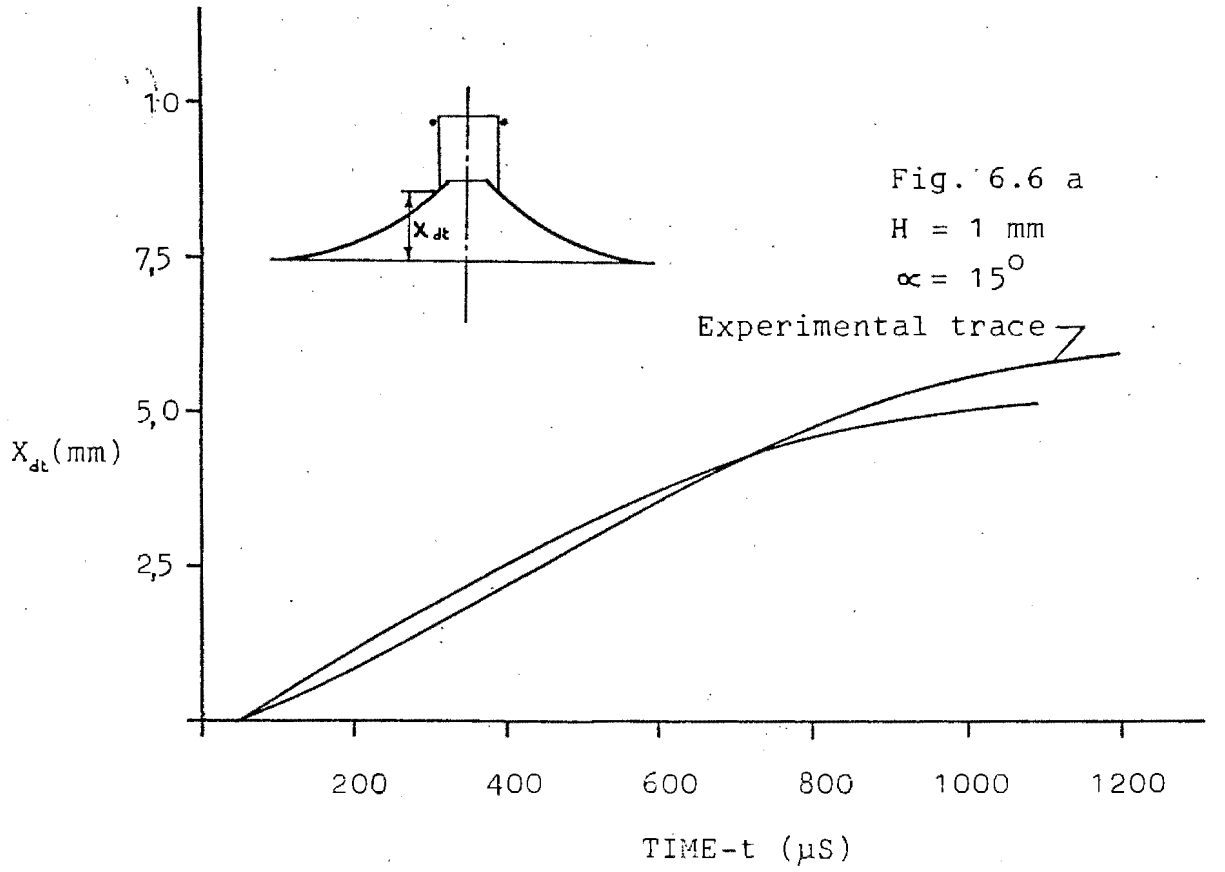

Fig. 6.6 a
H = 1 mm
$\alpha = 15^{o}$

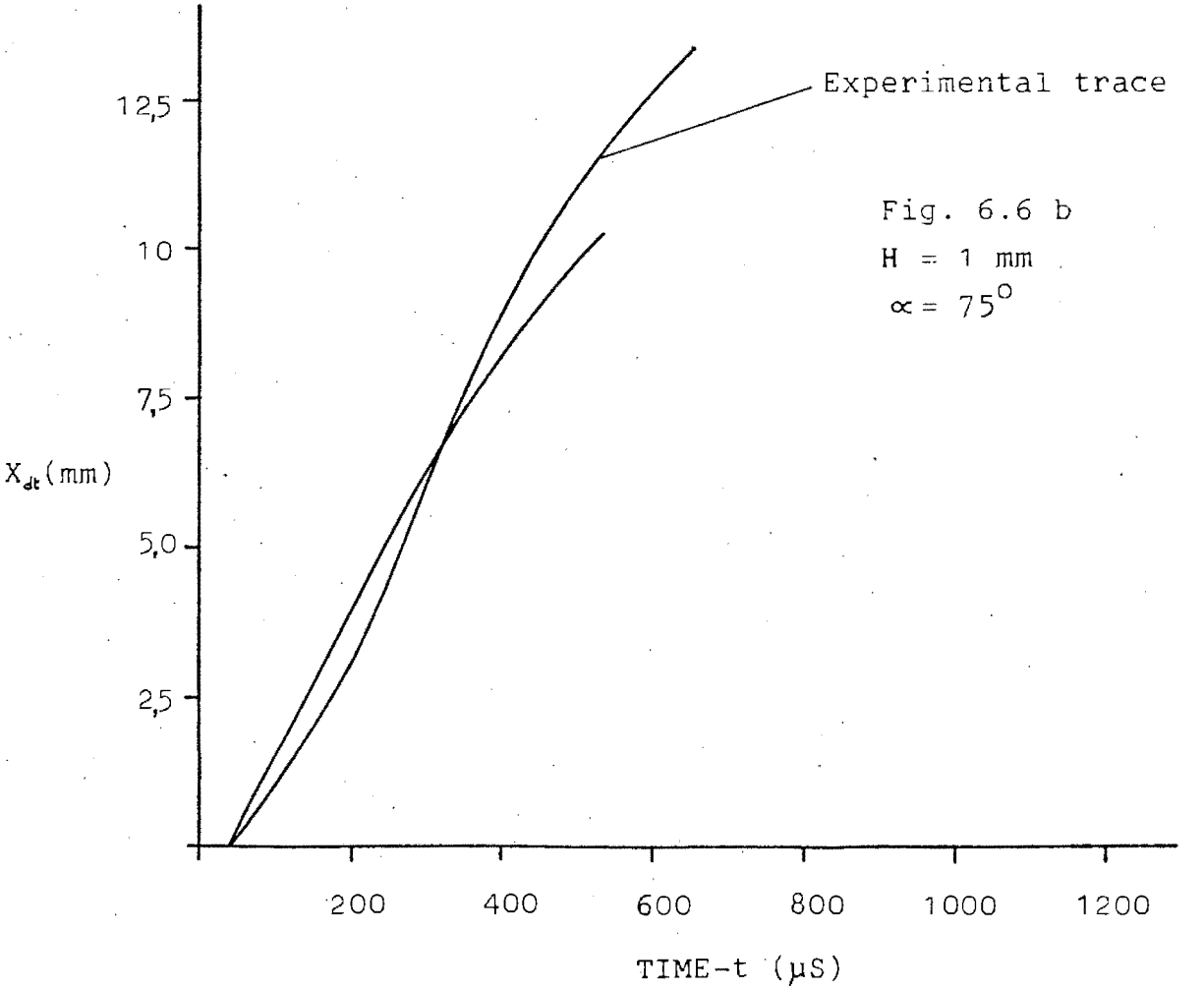

Fig. 6.6 b
H = 1 mm
$\alpha = 75^{o}$

6.7 ENERGY DISTRIBUTION IN THE TARGET PLATE

Instead of evaluating equation 2.1 directly i.e.

$$E = \int F dX \qquad \ldots\ldots\ldots\ldots\ldots\ldots\ldots\ldots \quad 2.1$$

it is instructive to compute the integral in the form of its Inner and Outer Zone components i.e.:

$$E = \int F dX_{iz} + \int F dX_{oz} \qquad \ldots\ldots\ldots\ldots \quad 6.4$$

The energy distribution for the Inner and Outer Zones throughout the penetration process was computed in this manner using the experimentally found penetration forces and target displacements. These results are plotted in Fig. 6.7. In addition a few energy predictions based on the Outer Zone deformation analysis of Section 3.1 (by use of equation 3.20) have been carried out and the results recorded in Fig. 6.7 a and 6.7 d.

Fig. 6.8 shows the final energy distribution in the target plates as a function of the projectile semi-cone angle and finally to summarise, the containment energies for the full range of projectile heads and target plate thicknesses are presented in Fig. 6.9.

Fig. 6.7 Energy distribution in the target plate as a function of time

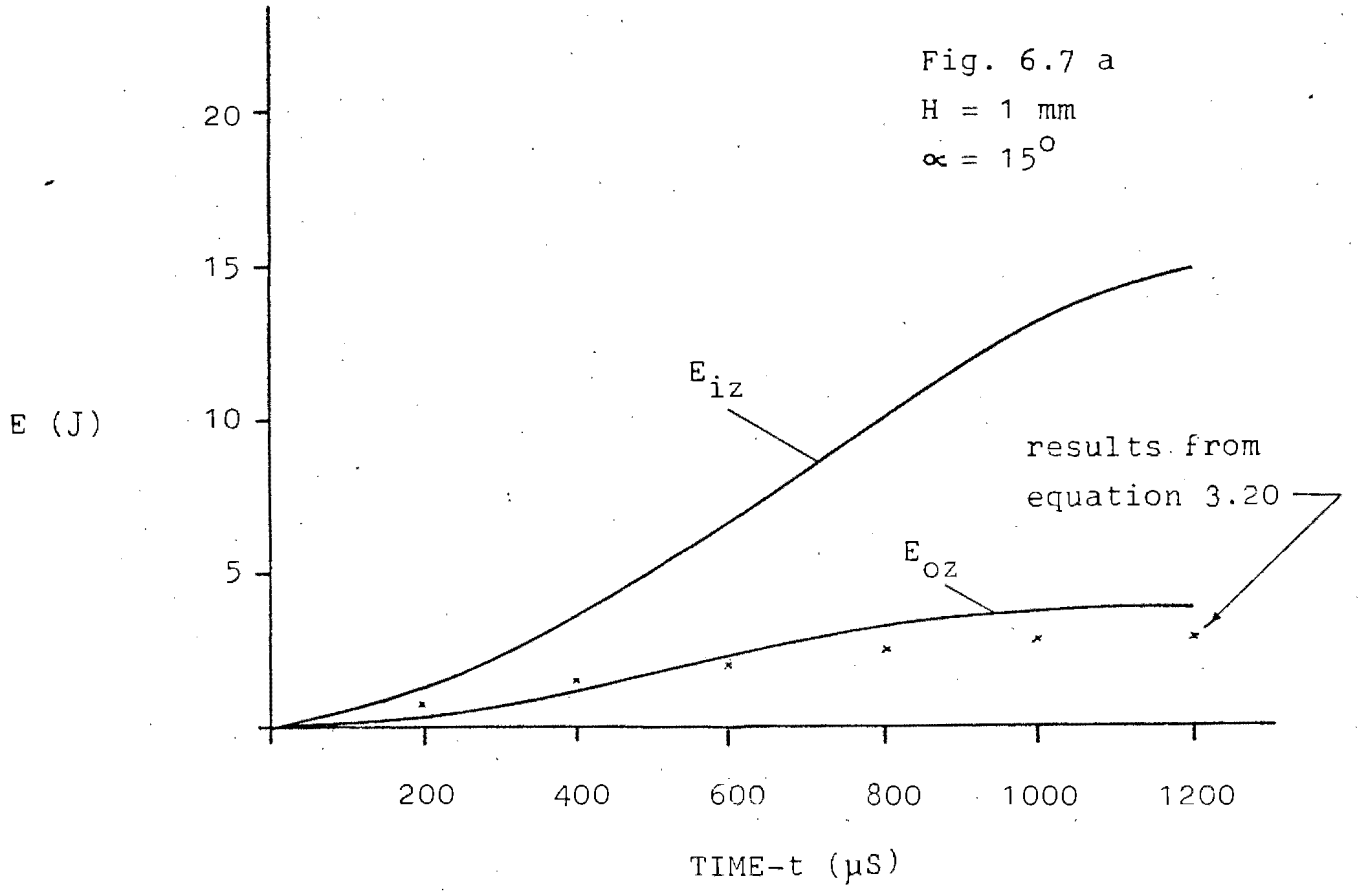

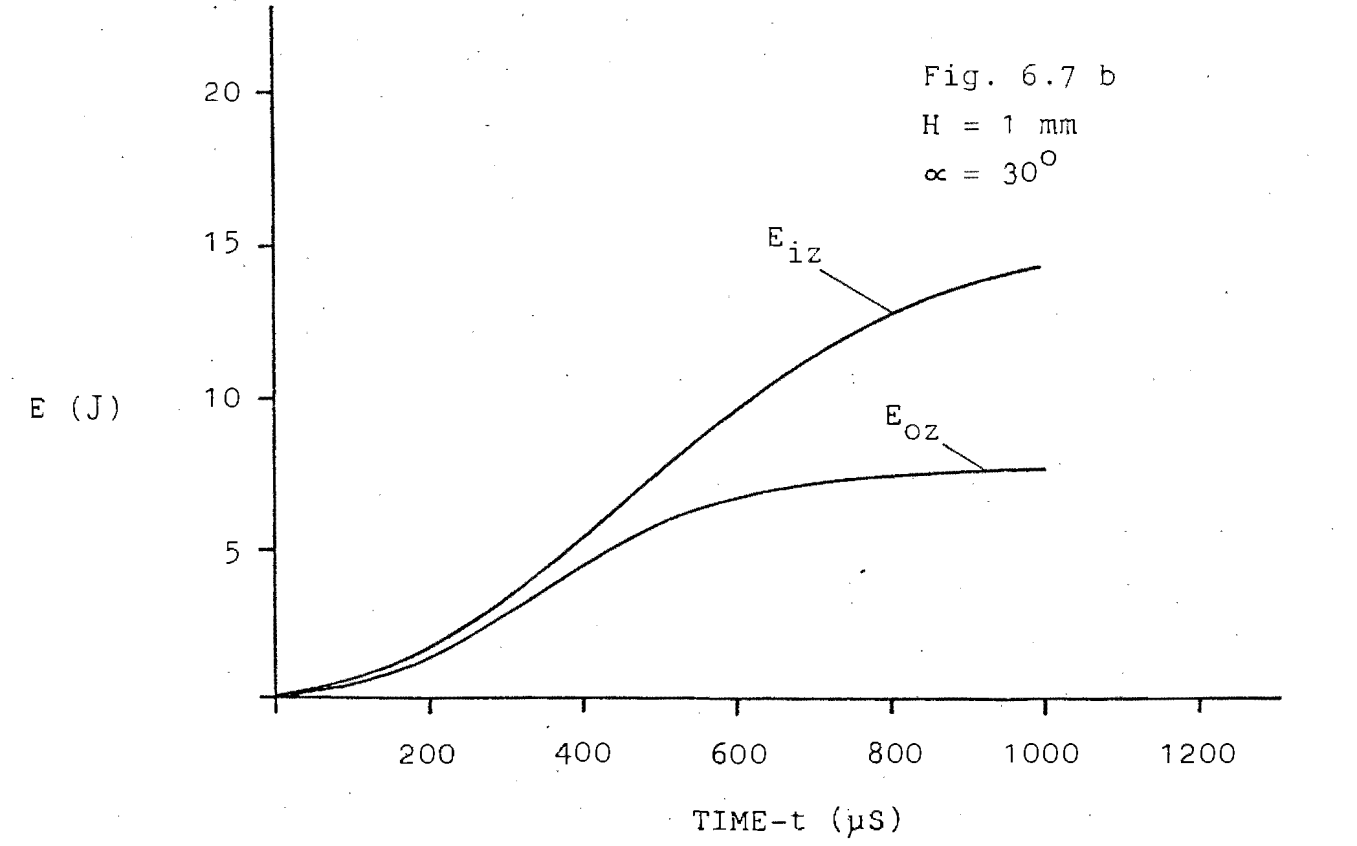

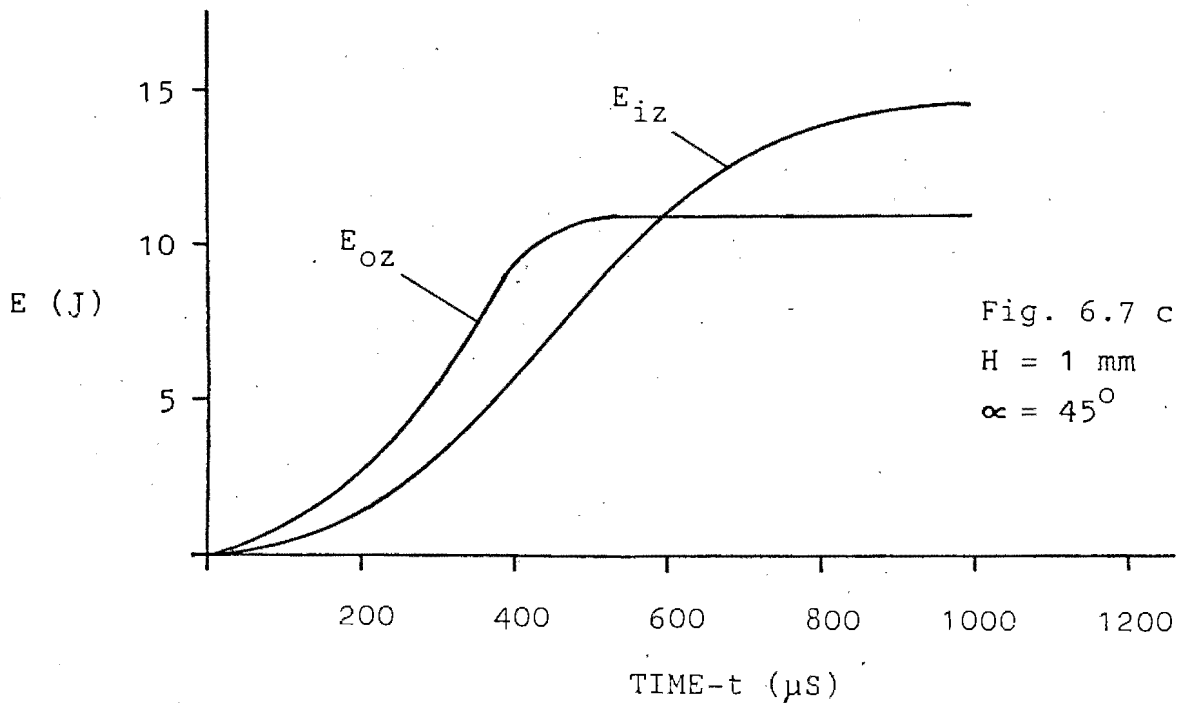

Fig. 6.7 c
H = 1 mm
$\alpha = 45^{O}$

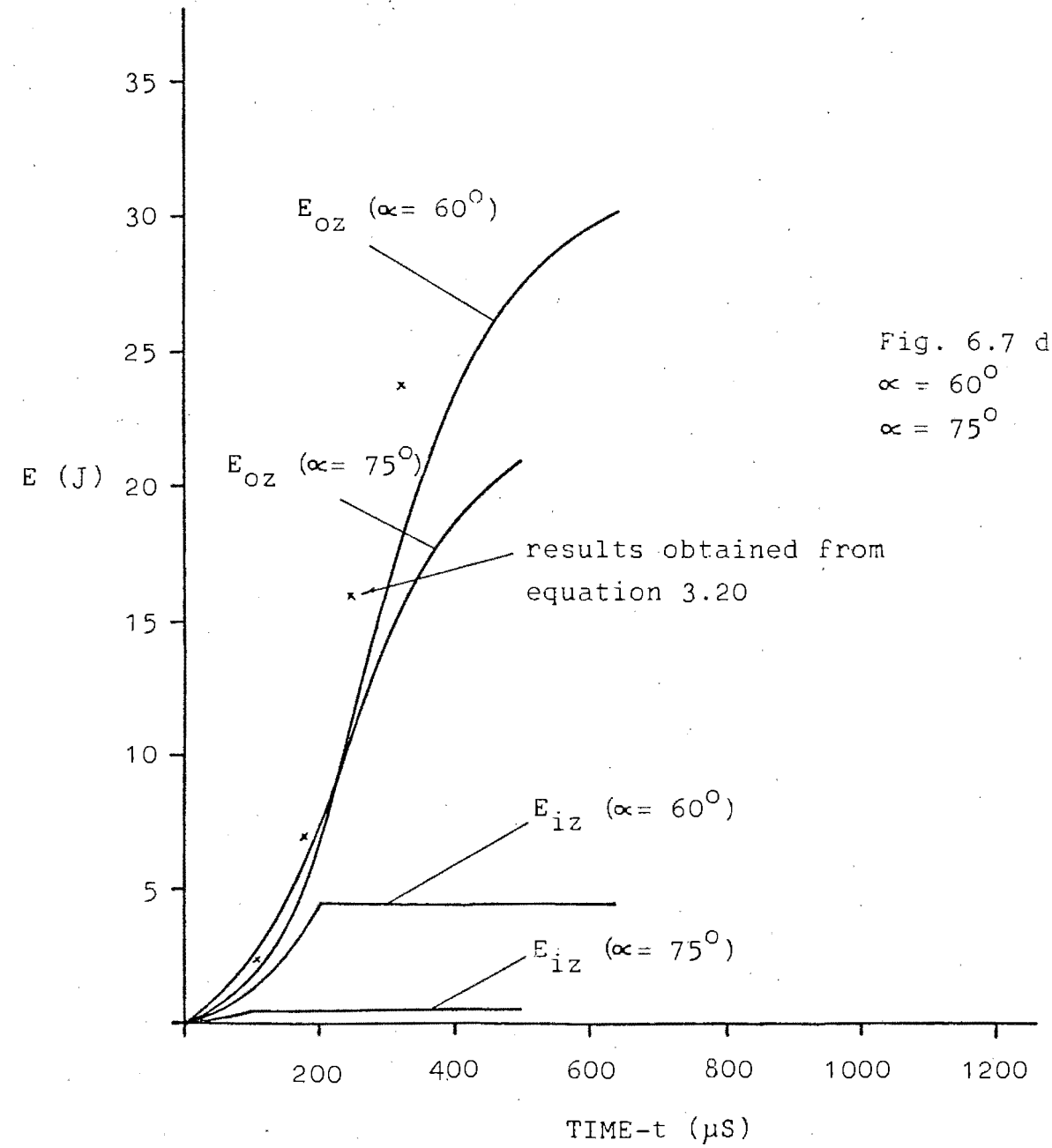

Fig. 6.7 d
$\alpha = 60^{O}$
$\alpha = 75^{O}$

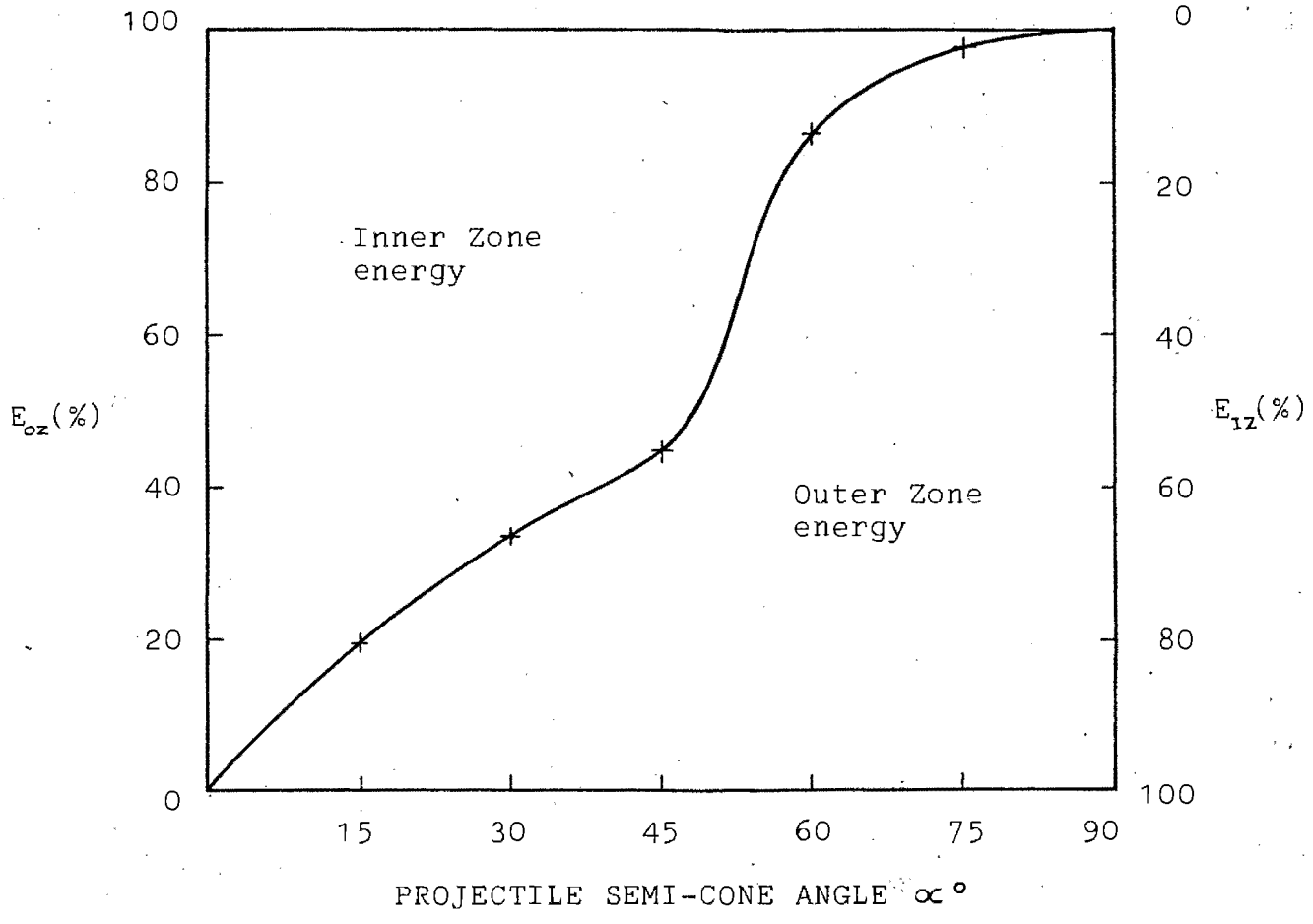

Fig. 6.8 Energy distribution in the target plate as a function of ∝

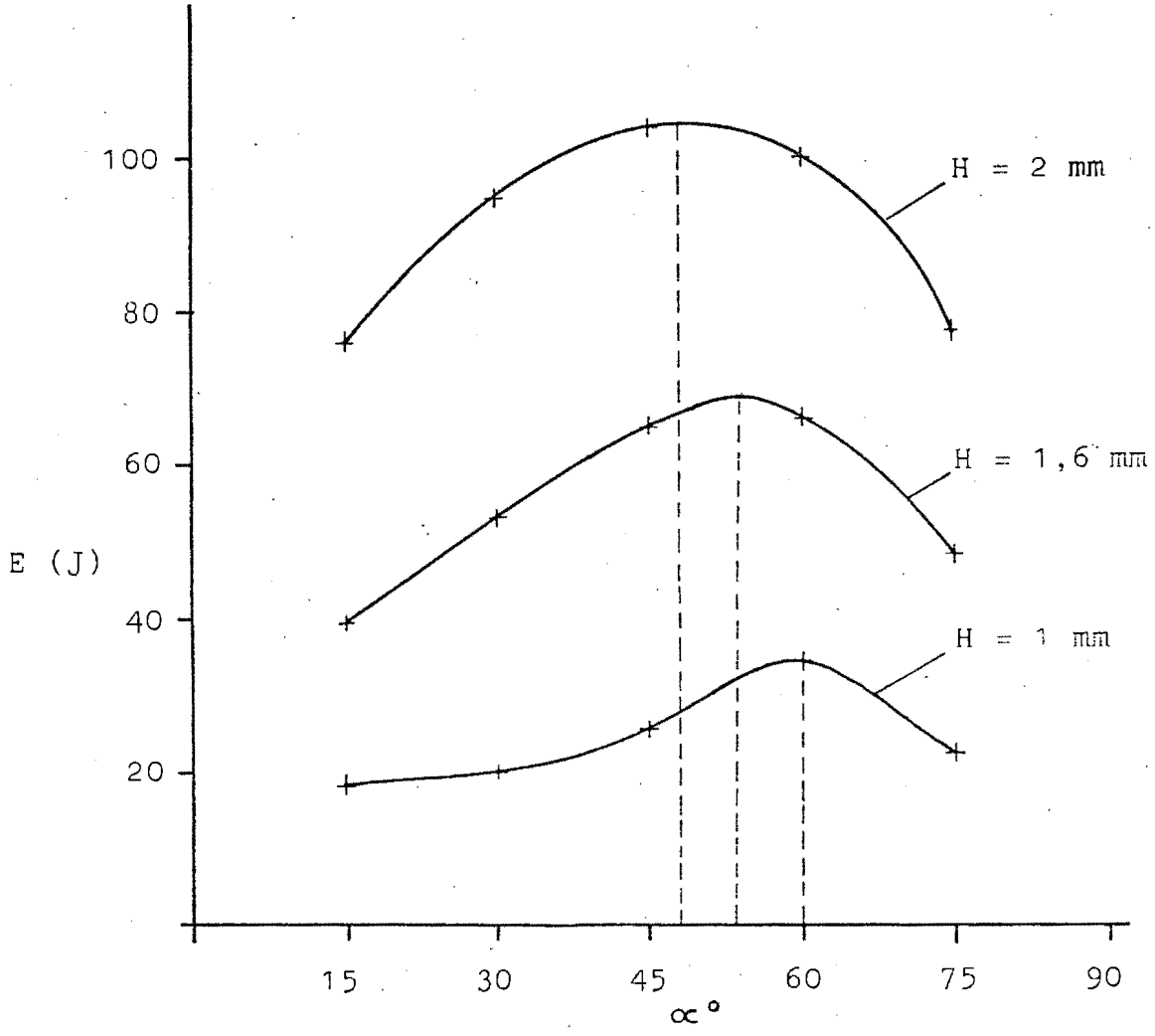

Fig. 6.9 Containment energy as a function of the semi-cone angle ∝

CHAPTER 7

DISCUSSION

7.1 THE MONITORING TECHNIQUES

The present work differs from previous thin plate penetration studies in that it has been possible to monitor the force of impact directly and this has enabled a more fundamental approach to be made to the penetration problem.

As mentioned in Chapt. 5, several researchers in the field have attempted to derive penetration forces from a knowledge of projectile displacement-time data, but with little success. The difficulty of numerically differentiating experimental data is well illustrated by the traces recorded in photo 5.3. The deceleration-time trace in this photograph clearly shows the projectile vibration phenomenon whereas in the velocity-time trace (from which the deceleration-time trace is derived) the phenomenon is barely discernable. To derive the deceleration-time trace from the velocity-time trace by a numerical differentiating procedure would indeed require extremely accurate primary data and when a double differentiating procedure is contemplated to derive deceleration from displacement data, it is highly unlikely that the final result will be of much value.

The accuracy of the traces recorded by the projectile monitoring system is difficult to ascertain since no parallel results are available for comparison. Derived force-time traces must have the correct functional form (F(t)) as well as the correct scale factor to be considered accurate. An indirect check which combines these two aspects of accuracy is possible through the use of the impulse momentum relationship i.e.:

$$\int F dt = M(V_o - V_f) \quad \ldots\ldots\ldots\ldots\ldots\ldots\ldots\ldots \quad 7.1$$

The projectile monitoring system lends itself to this type of check since all the parameters involved can easily be measured. The left hand side of equation 7.1 is evaluated by numerically integrating force-time traces, while the approach and post penetration velocities are conveniently measured directly from the velocity-time trace which is recorded simultaneously with the deceleration-time trace (see photo 5.3).

For the range of projectiles tested, the computed areas beneath the F-t traces agree with the projectile momentum drops to within 4% - the agreement being best for acute projectiles and steadily decreasing for the more obtuse ones.

This trend in accuracy can be explained in terms of the approximate nature of the projectile analysis of Chapt. 4. Whereas the analysis serves as a rational way of averaging particle motion during impact, it becomes less reliable as the impact duration approaches the projectile's natural period of vibration since the averaging procedure then takes place over fewer projectile oscillations. Ideally, the analysis should be able to predict overall projectile behavior irrespective of impact duration, but in practice the complex nature of the projectile (i.e. pointed head and composite material construction) can only be approximated in the projectile model and the less emphasis placed on the functional form of the projectile's vibrational component of particle motion, the more accurate is the final result. The projectile used in the present study has a natural period of 175 μS and impacts incorporating at least three projectile oscillations can be monitored with the stated accuracy.

Several researchers, notably Zaid and Travis (24) have reported the significance of post penetration energy and account had to be taken of this phenomenon in the present study. (Post penetration refers to the region of impact when the cylindrical sides of the projectile are passing through the target plate)

Photo 5.3 provides an illustration of the phenomenon.

The impact from which this trace was recorded was considered to be a good example of containment - the projectile being stopped within 5 mm of the cylindro-conical shoulder. It should be noted however that at the terminal point of the impulse (or deceleration-time trace) the projectile still possesses considerable kinetic energy.

Since it is extremely difficult to approach the ideal containment condition more closely than this, the procedure used here has been to minimise the post penetration period and to simultaneously record pre- and post penetration velocities. These velocities are then incorporated in the penetration model to ensure identical conditions are being studied.

It is interesting to compute a value for the post penetration force and this can be done by measuring the negative slope of the velocity-time trace in the post penetration region (see photo 5.3). Forces computed on this basis were found to be of approximately 150 N magnitude and by acting over a 5 mm displacement, they will absorb 0,75 J of the projectile's kinetic energy. This corresponds to a projectile post penetration velocity of 6,8 m/S which compares favourably with the monitored value of V_t = 7,1 m/S.

Several points of interest have arisen from the two methods used to monitor target response.

Firstly it was noticed that containment velocities required for the target monitoring device were between 1,5 and 3,5% lower than those recorded for the projectile monitoring apparatus. The reason for this is thought to lie in the different materials used in the two monitoring projectiles which both have identical masses of 0,032 kg. Having viscoelastic properties and a lower value of Young's Modulus, the nylon body of the projectile monitoring apparatus will absorb and dissipate more penetration energy than its aluminium counterpart.

The nature of the Outer Zone motion at a distance of 9 mm from the point of impact is clearly shown in the trace recorded in photo 5.7. Typically the target will accelerate to a maximum velocity which is somewhat below the current projectile velocity and then decelerate along with the projectile. Body forces associated with this motion may in some instances be quite significant and will be discussed in the following section.

By measuring the base diameter of the sensor mounting tube before and after impact it is possible to get an idea of the severity of the target's radial strain. Typically this was found to be approximately 8% which corresponds fairly well with values reported by Zaid (23) and Duffey (19).

7.2 THE NATURE OF F-X HISTORIES

Three sets of experimental F-X histories for three thicknesses of target plate are presented in Fig. 6.1 (abc). The magnitude of the forces recorded covers a wide range (from 7 kN to 1 kN) but the same scales have been used for all three sets of curves to highlight the fact that the forms of traces corresponding to particular projectile semi-cone angle are similar - the effect of target plate thickness being mainly to change the magnitude of the penetration force.

In the present study, penetrations involving 15°, 30° and 45° projectiles all take place by the petalling process irrespective of the target plate thickness. The dividing lines between the two modes of penetration (ie petalling and conic deformation) are defined by the maxima of the containment energy curves shown in Fig. 6.9. This phenomenon will be explained later.

Typically, the initial stage of petalling is characterised by an exponential rise in penetration force with projectile displacement. At a certain stage this rapid increase ceases and is followed by a steady rise in penetration force with displacement. This stage is terminated by a sudden drop in penetration force which marks the end of the penetration. This sequence is best illustrated by the 15°, 1mm trace. For thicker plates and less pointed projectiles these stages

become less well defined but are still discernable.

Unlike the petalling traces those of conic deformation do not have well defined stages. These curves are typically bell-shaped with initial rapid increases in penetration force transforming smoothly to a peak and then decreasing to produce an almost symmetrical force-displacement history.

Further discussion of the penetration F-X traces is possible through the penetration model developed in Chapt. 3. Using this analysis for a 1 mm thick target plate, the traces shown in Fig. 6.2, 6.4 and 6.5 have been generated and are compared with their experimental counterparts.

7.2.1 THE INDENTATION PHASE

The penetration model indicates that this phase is very short-lived in the case of obtuse projectiles which lead to the conic deformation mode of failure lasting 40 μS for the 60^{o} projectile and 25 μS for the 75^{o} projectile. The transition points where indentation ceases have been marked in Fig. 6.2 and 6.4.

This phase of penetration is mainly governed by the magnitude of the target's mean pressure of resistance

which was found using the E-α traces in Fig. 6.9 by the method outlined in section 3.2.2, to have a value of $\sigma_p^* = 0,15Y$. The reason that such a low contact stress is required to produce plastic flow during indentation of this kind is that the prevailing membrane and hoop stresses are both large and in the correct sense (tensile) to fulfill the requirements of a yield criterion.

Calculating the limiting indentation depth for the 75^o projectile on this basis gives a value of $X_I^* = 0,3$ mm which is a realistic value and corresponds to the type of deformation found in ejected caps.

Whereas for indentations which proceed into the conic deformation mode, X_I tends to a limiting value of X_I^*, those for the more acute projectiles (15^o, 30^o, 45^o) have no such limit and for these, α has been calculated using the experimental $r_o - \theta_o$ traces shown in Fig. 6.4. This procedure gives values for σ_p^* of 0,55Y, 0,31Y and 0,2Y for the 15^o, 30^o and 45^o projectiles respectively. This trend in the magnitude of σ_p^* is due to the change in geometry of the stresses at the projectile-target contact surface. As the projectile semi-cone angle gets smaller it approaches the ideal radial hole expansion of Taylor (9) when $\sigma_p^* = Y$, while at the other extreme, the 45^o pro-

jectile's value of σ_p^* approaches the conic deformation result.

It should be noted that once $X_1 > H$ the indentation analysis is strictly speaking invalid since as soon as the tip of the projectile leaves the distal surface of the target, the projectile-target contact area will no longer increase with the square of the Inner-Outer Zone boundary radius. This change in the mode of penetration has not been modelled here but does not affect the final result significantly.

The indentation phase of petalling represents the kind of penetration envisaged by Taylor (9), Brown (10) and Thomson (4) which is characterised by a hypothetical infinitely ductile material which can undergo the prescribed hoop strain without cracking. In the early stages of indentation when the effective D/H ratios or rather r_o/H ratios are low, there is sufficient target material in the vicinity of the projectile to accomodate the large hoop strains and this type of penetration is possible. As r_o/H ratios grow however, a point is reached where the target can no longer accomodate the hoop strain and radial cracks form which lead directly to petalling.

The effect of the target plate thickness on petalling is well illustrated in the traces of Fig. 6.1. For the 1 mm thick target plate (large D/H ratio) the petalling transition occurs early in the penetration and is clearly defined. For the thicker

plates the transition occurs later with a more gradual transformation to the petalling mode.

7.2.3 CONIC DEFORMATION

When obtuse projectiles (60^{o} and 75^{o} in the present example) reach the limiting indentation depth X_1^* , a smooth transition into conic deformation occurs which is shown in the traces of Fig. 6.2 and 6.4. For a short period after this transition, both Inner and Outer Zone displacements (X_c and X_{do}) take place, but the former ceases as soon as the Inner Zone reaches its limit at $r_o = D/2$. Except for the plug separation displacement (X_s) which occurs in the terminal stage of conic deformation, the remainder of the penetration is governed entirely by the Outer Zone response.

One obvious discrepancy between the modelled and experimental F-X traces of Fig.6.2 is the lateral shift which separates them. This effect is due mainly to the simplistic nature of the Outer Zone model which has been used in the current work and better agreement could probably be obtained by including the effects of the target's mass and elastic response. The traces of Fig. 6.6 clearly show the difference between the actual Outer Zone response and the predicted response based on the thin rigid plastic membrane model. The sinuous nature of the experimental result indicates that target inertia effects

cannot be totally neglected. It was also noted in the course of the study that 1 mm targets could undergo a central elastic deflection of up to 2 mm. The inclusion of these two effects into the Outer Zone model would probably bring the experimental and analytical traces into better agreement.

The value of the target's tensile yield stress (Y) used in the penetration model was found by a simple tensile test to be 119 MN/m^2. Whereas this value gave excellent agreement between predicted and experimental F-X histories for the 1 mm plate, the 1,6 and 2 mm plate required values which were 27 and 48% larger to achieve the same agreement. As the target material is relatively strain-rate insensitive, this additional stress can only be due to the fact that the lateral stiffness of these thicker plates is not negligibly small as assumed by the thin plastic membrane model and the higher yield stress must be used to compensate for this effect. Unless thickness effects such as bending are included in the Outer Zone model it appears that the current thin plastic membrane model is limited to impact situations where D/H ratios are greater than 10.

The modelled terminal stage of conic deformation is markedly different from the experimental result. The smooth bell-shaped nature of the experimental F-X histories suggests that the shear failure and disc ejection process which takes

place is not as abrupt as assumed but is a more gradual process. It is interesting to note that the Outer Zone model which accounts for plate thinning predicts a maximum possible penetration force of $F = \pi r_o HY$ when the boundary slope θ_o reaches a value of 45^o. For slopes greater than this, the predicted penetration force will decrease due to the plate thinning effect. Although this prediction models the trend of events correctly, the rate of thinning is far slower than appears to be the case in practice. This suggests that plug separation involves a more complex mechanism than originally thought and probably takes place by a combined shear tensile process over an extended period.

7.2.4 PETALLING

As soon as radial cracks begin to form in the target plate at the end of the petalling-indentation phase, there is a distinct change in the slope of the F-X histories. This transition is even more clearly defined by the cusps in the r_o-θ_o traces cf Fig. 6.4.

From these traces it can be seen that θ_o, the boundary slope, reaches its maximum value at the end of the indentation phase and once petalling proper has set in, this angle decreases progressively with the penetration. This is an unexpected re-

sult, since intuitively one expects r_o and θ_o to both increase with the penetration, as is the case in conic deformation.

The reason for this trend in θ_o can be found from the relation:

$$F = \pi r_o HY \sin 2\theta_o \quad \ldots\ldots\ldots\ldots\ldots\ldots\ldots\ldots \quad 3.17$$

During petalling, r_o increases almost proportionately with the projectile displacement (X) while the penetration force (F) increases only marginally. (This is best illustrated by the 15^o F-X trace). If equation 3.17 is to hold under these circumstances, θ_o must decrease as the penetration proceeds.

Unlike the $r_o - \theta_o$ relationships of conic deformation which are only applicable during the early stages of penetration, those of petalling extend over the greater part of the penetration process and are mainly responsible for the form of the F-X history.

The complex nature of the terminal phase of petalling when $r_o = D/2$, prohibits the formulation of a simple $r_o - \theta_o$ relationship as has been found for the initial phase, and although the simple terminal phase analysis circumvents this problem, it does not model the experimental result closely.

For sharp projectiles (15^o, 30^o), the petalling analysis

models the penetration process well, as shown by the traces of Fig. 6.2 b. It should be noted that in these penetrations, the terminal phase plays a minor role, so that inadequacies in the penetration model are not significant.

For the 45^{o} projectile, which represents an impact in the petalling-conic deformation transition zone, a type of quasi-conic deformation persists until late in the penetration and is followed by a delayed petalling process. As the petalling phenomenon extends into the terminal phase (i.e. $r_o = D/2$), a large portion of the F-X history cannot be modelled well and results in the poor agreement found for the 45^{o} trace. This type of penetration is extremely difficult to model since there is no obvious relationship between the target deformation and the projectile motion during the terminal phase.

In the present example, the 60^{o} projectile represents the upper bound of the petalling-conic deformation zone. This penetration is a classic example of a combined mode process, with eventual target failure occuring by the formation of two conically deformed petals which are partially detached at their bases. It has been found that combined mode penetrations tending to the upper bound, are best modelled by means of the conic deformation analysis which is able to describe target behavior after the Inner Zone reaches its limit at $r_o = D/2$.

The petalling analysis is based on the annular ring model

described in Section 3.2.4.2 which ascribes the target's penetration resistance totally to the hoop straining of a hypothetical ring of target material. The cross-sectional area of this ring (see Fig. 7.1) is assumed to vary throughout the penetration according to the relationship:

$$A = A_F - K_A H(D/2 - r_o) \quad \ldots\ldots\ldots\ldots\ldots\ldots\ldots\ldots \quad 3.37$$

which can be rewritten as:

$$A = A_o + K_A\, r_o\, H \quad \ldots\ldots\ldots\ldots\ldots\ldots\ldots\ldots \quad 7.2$$

where A_o represents the cross-sectional area at $r_o = 0$ and K_A is constant.

When equation 7.2 is fitted to the experimental F-X traces to derive the petalling $r_o - \theta_o$ relationship, K_A takes on a mean value of 1.25. Thus we have:

$$A = A_o + 1.25 r_o H \quad \ldots\ldots\ldots\ldots\ldots\ldots\ldots\ldots \quad 7.3$$

An estimate of the actual 'A' function can be obtained from the geometry of the deformed Inner Zone during petalling. This is shown in Fig. 7.1

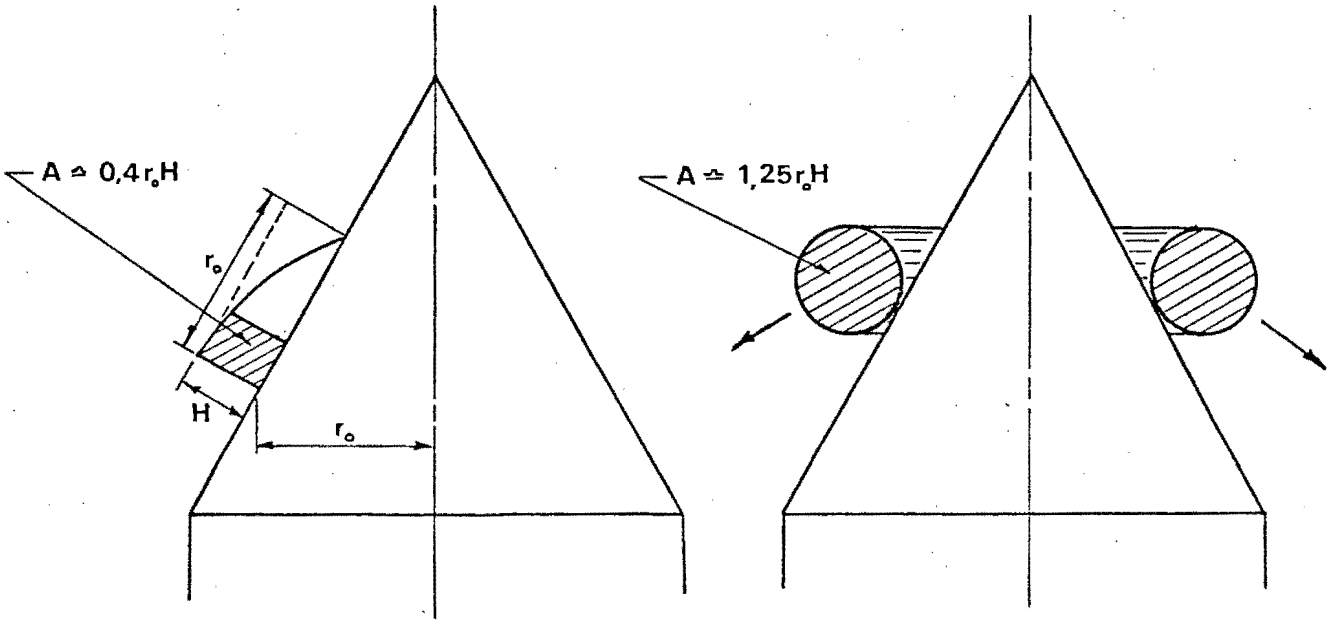

Fig. 7.1 The cross-sectional areas of the Inner Zone and hypothetical annular element during petalling

The maximum possible area the Inner Zone can have disregarding deformation and cracking is $A = r_o H$. Including deformation reduces this value to $0,6r_o H$ and assuming that radial cracks extend halfway through the Inner Zone the area is reduced to $A = 0,4r_o H$.

The difference between this result and that predicted by equation 7.3 indicates that an additional mechanism is involved in the petalling process. This "missing area" can be accounted for in terms of the forces required to bend the intact region of the Inner Zone into its truncated conical form. This finding indicates that in the Inner Zone, thickness effects are significant and that plastic bending probably accounts for more than 60% of the target's resistance during petalling.

The bending and hoop straining components are critically determined by the physical dimensions of the intact region of the Inner Zone and to develop a theoretical model of petalling requires a better understanding of the radial crack growth phenomenon.

7.3 DISTRIBUTION OF THE PENETRATION ENERGY IN THE TARGET PLATE

The outcome of any penetration study must invariably be to determine how a target absorbs projectile kinetic energy. Few studies have approached the problem directly from the point of view of the force-penetration displacement histories, most employing energy relationships based on the deformation of the target plate.

By using this indirect approach it is often possible to account for penetration energy reasonably well, even though implied force-displacement histories are totally erroneous. The reverse procedure which has been used in this study is thought to be far more reliable and the results presented in Fig. 6.7, 6.8 and 6.9 are able to highlight some important aspects of penetration.

The energy distribution curves shown in Fig. 6.7 were derived from the displacement-time traces of Fig. 6.6 and both sets of curves can be seen to have similar characteristics. Once $F\text{-}X_{oz}$ and $F\text{-}X_{iz}$ traces have been found using this displace-

ment-time data it is a simple matter to numerically integrate these expressions over their respective displacements thus giving Inner and Outer Zone energy expressions.

As expected, the pointed projectiles dissipate most of the projectile energy in the Inner Zone mechanisms that take place. By neglecting Outer Zone response for impacts of this type, Zaid and Paul (5) and Thomson's (4) models would incur a 20% error for the 15^{o} projectile, 34% for the 30^{o} projectile and 42% for the 45^{o} projectile. Impacts involving more obtuse projectiles than 45^{o} would not fall into the range of these models.

Using the Outer Zone strain energy analysis which is summarised by equation 3.20, it is possible to predict values for the Outer Zone energy from the point of view of target plate deformations. These values are plotted in the graphs of Fig. 6.7 a and 6.7 d and show that for the small plate deflections recorded for the 15^{o} projectile, predictions are low whereas for the large deflections recorded for the 75^{o} projectile, predictions are high.

This result indicates that many of the assumptions made in modelling the Outer Zone response, which permit the prediction of penetration forces reasonably well, nevertheless produce a rather inflexible model which does not reflect changes in the Outer Zone response for the variety of impacts in-

vestigated. As previously explained, this model could be improved by incorporating the target's inertia and elastic responses.

The transverse dynamic equation for the Inner Zone during petalling is given by the expression:

$$F = F_p (\mu \text{Cos}\alpha + \text{Sin}\alpha) \quad \ldots\ldots\ldots\ldots\ldots\ldots\ldots\ldots \quad 7.3$$

where F_p is the interfacial compressive force between the target and projectile. Assuming that the coefficient of friction has a value of 0,1 and that the average penetration force for the 15° projectile is 0,4 kN, the frictional force μF_p can be evaluated from equation 7.3 to be 113 N. (Note that this value is of the same order of magnitude as that found for the post-penetration force in Section 7.1).

During penetration this force acts for a 24,3 mm displacement along the projectile's conical head and absorbs 2,75 J or 14% of the penetration energy. If the Inner Zone bending mechanism absorbs 60% of the Inner Zone energy as suggested in Section 7.2.4 and friction accounts for 14% then only 4,9 J can be attributed to the Inner Zone hoop straining mechanism.

This value can be used to estimate the magnitude of strain which the Inner Zone undergoes during petalling. For this

region of the target the strain-energy relationship (equation 3.18) becomes:

$$\bar{\varepsilon}_{\theta} = E_{iz} \, (\pi D^2 HY/4) \qquad \ldots\ldots\ldots\ldots\ldots\ldots\ldots\ldots \quad 7.4$$

and gives a value for the mean hoop strain $\bar{\varepsilon}_{\theta}$ of 0,33.

This value represents the mean critical hoop strain that the target material can tolerate before the radial crack phenomenon renders it ineffective. Fig. 3.12 which plots hoop strain as a function of position in the Inner Zone, indicates that a value of $\bar{\varepsilon}_{\theta} = 0,33$ means that only 30% of the Inner Zone remains intact, the remaining 70% being petalled.

It should be noted that this value for the critical hoop strain is a <u>mean</u> value. As previously mentioned, during the indentation phase of petalling when r_o/H ratios are low, the plate can effectively accommodate hoop strains so that the critical value of ε_{θ} is theoretically, infinitely large. At the indentation-petalling transition, ε_{θ} attains a finite value and radial cracks appear in the Inner Zone. As the penetration proceeds further, the critical strain decreases in value so that the petalled region will envelope more and more of the Inner Zone material. To develop a theoretical model of penetration by petalling, this kind of behavior must be accurately modelled.

Finally, to summarise, the containment energies recorded for the three thicknesses of target plate and five projectile heads are plotted in Fig. 6.9 as a function of the projectile semi-cone angle α.

These curves have characteristic maxima which represent the transition between the petalling and conic deformation modes of penetration and it is apparent that thicker plates require more acute projectiles to reach this condition.

The amount of energy absorbed by a target plate is a function of the magnitude of the forces generated and the displacement over which they act. For small values of α, penetration forces are small but extend over a large displacement while the reverse is true for large values of α. In the case of the petalling-conic deformation type of impacts, Inner Zone stresses are optimally distributed which results in both large penetration forces and displacements.

CHAPTER 8

CONCLUSIONS

The monitoring techniques developed in this thesis operate reliably, economically, and with a high degree of accuracy.

In its present form, the projectile transducer is limited to moderate impacts in the lower ballistic range where impact durations are longer than 500 μS and amplitudes less than 10 kN. This is not an intrinsic limitation to the method however, as a differently designed projectile could monitor far more severe impacts.

The target transducer monitoring the Inner Zone radial expansion, has enabled the projectile transducer data to be interpreted in terms of the target parameters. This has provided invaluable information about the target's response to penetration and greatly facilitated the development of a penetration model.

The empirical penetration analysis developed in this thesis has been successful in modelling the experimentally derived F-X histories and most of the primary features of these traces have been explained. The model is however limited

to thin plate impacts where D/H ratios are greater than 10 and to ductile strain rate insensitive target materials such as aluminium.

The concept of modelling the target response in terms of its inner and outer zone responses is a good one, and could form the basis of a purely theoretical approach to the penetration problem. Such an approach however, would require further study into the following aspects of thin plate penetration;

(a) A physical description of the inner zone during petalling which accounts for inner zone deformation and radial crack growth.

(b) An inner zone petalling model based on the plastic bending and hoop straining of the target material.

(c) An analysis to predict indentation behavior.

(d) An analysis incorporating a failure criterion to model disc ejection during conic deformation.

(e) An improved outer zone model which includes the target's inertia and elastic responses.

REFERENCES

1. Goldsmith, W., Liu, T.W. and Chulay, S., "Plate Impact and Perforation by Projectiles" Exp. Mech. 5, 385 (1965)

2. Nishiwaki, J., "Resistance to the Penetration of a Bullet through an Aluminium Plate" Jnl. Phy. Soc. Japan 6, 374 (1951)

3. Awerbuch, J. and Bodner, S.R., "Analysis of the Mechanics of Perforation of Projectiles in Metallic Plates" Int. Jnl. Solids Structures, 10, 671 (1974)

4. Thomson, W.T., "An Approximate Theory of Armour Penetration" Jnl. Appl. Physics, 26, 80 (1955)

5. Zaid, M. and Paul, B., "Mechanics of High-Speed Projectile Perforation" Jnl. Franklin Institute 264, 117 (1957)

6. Recht, R.F. and Ipson T.W., "Ballistic Perforation Dynamics" Jnl. Appl. Mech. Trans ASME, Ser. E 30 (3) 384 (1963)

7. Beth, H.A. "An Attempt at a Theory of Armour Penetration" Frankford Arsenal Rpt No. UN-41-5-23 (1941)

8. Kinslow, R. (editor) "High-Velocity Impact Phenomena" Academic Press (1970)

9. Taylor, G.I., "The Formation and Enlargement of a Circular Hole in a Thin Plastic Sheet" Quarterly Jnl. Mech. and Appl. Math., 1, 103, (1948)

10. Brown, A. "A Quasi-Dynamic Theory of Containment" Int. Jnl. Mech. Sci. 6, 257 (1964)

11. Goldsmith, W. and Finnegan, S.A. "Penetration and Perforation Processes in Metal Targets at and above Ballistic Velocities" Int. Jnl. Mech. Sci. 13, 843 (1971)

12. Goldsmith, W. and Calder, C.A. "Plastic Deformation and Perforation of Thin Plates Resulting from Projectile Impact" Int. Jnl. Solids Structures, 7, 863 (1971)

13. Beynet, R. and Plunkett, R. "Plate Impact and Plastic Deformation by Projectiles" Experimental Mechanics 5, 65 (1971)

14. Latheby, J.W. and Skidmore, I.C. "The Deformation and Plugging of Thin Plates by Projectile Impact" Institute of Physics Conf. Ser. No. 21, 429 (1975)

15. Timoshenko, S. and Woinowsky-Krieger, S. "Theory of Plates and Shells" McGraw Hill (1959)

16. Craggs, J.W. "The Normal Penetration of a Thin Elasto-Plastic Plate by a Right Circular Cone" Proc. Royal Soc. of Edinburgh, A, 63, 369 (1952)

17. Calder, C.A., Kelly, J.M. and Goldsmith, W. "Projectile Impact on an Infinite Visco-Plastic Plate" Int. Jnl. Solids Structures, 7, 1143 (1971)

18. Masket, A.V. "The Measurement of Forces Resisting Armour Penetration" Jnl. Appl. Physics 20, 132 (1949)

19. Duffey, T.A. "The Large Deflection Dynamic Response of Clamped Circular Plates Subjected to Explosive Loading" Sandia Corp. Res. Report No. SC-RR-67-532 (1967)

20. Johnson, W. "Impact Strength of Materials" Edward Arnold (1972)

21. Bluhm, J.I. "Stresses in Projectiles during Penetration" Proc. SESA 13 (2) 167 (1956)

22. Wingrove, A.L. "The Forces for Projectile Penetration of Aluminium" J. Phys. D: Appl. Phys. 5, 1294 (1972)

23. Pearson, G.C. and Miles A.W. "Snap Action Pneumatic Valve for a Gas Gun" Jnl. Sci Instrum. 45, 459 (1973)

24. Zaid, A.I.O. "An Examination of the Perforation of a Mild Steel Plate by a Flat-Ended Cylindrical Projectile" Int. Jnl. Mech. Sci. 15,129 (1973)

LIST OF APPENDICES

APPENDIX A

GAS GUN DESIGN AND PERFORMANCE

A.1 THE GAS GUN

The general layout of the gas gun and mounting is shown in Fig. A 1. To give a rigid and massive foundation, the gun is mounted on a 300 mm x 100 mm rolled steel joist which itself stands on legs of 50 mm square steel tubing. The upper flange of the rolled steel joist is covered with a 100 mm x 8 mm thick bright mild steel strip and provides a test bed, facilitating the alignment of the field magnet, target holder and projectile catcher with the gun barrel.

A console at the breech end of the gun is used to house the pressure regulating valves, the monostable circuit for the solenoid valve and the Schmitt triggers for the approach velocity measuring apparatus. The gas bottle lies conveniently under the test bed and its weight helps to stabilise the rig. The general layout can be seen from photo. A.1 and Fig. A.1.

A.2 PRINCIPLE OF GAS GUN VALVE

The gas gun was designed specifically to launch the special projectile described in Chapter 5 . To penetrate 2 mm thick aluminium sheet, a projectile velocity

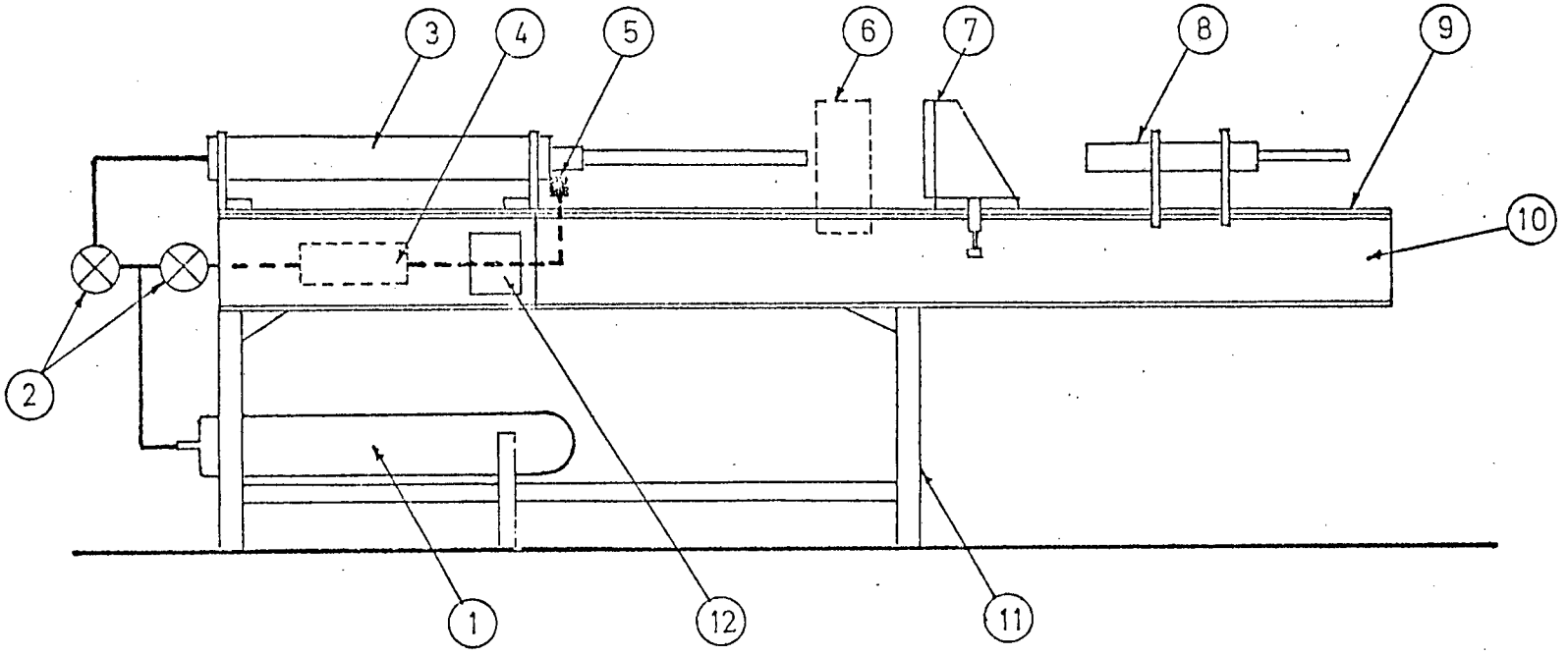

1	Compressed air cylinder	7	Target holder
2	Pressure regulating valves	8	Projectile catcher
3	Driver chamber	9	Bright mild steel bed
4	Valve pressure resevoir	10	300 × 125 R.S.J.
5	Solenoid valve	11	Sq. steel tubular legs
6	Position of velocity transducer	12	Control pannel

Fig. A 1 General layout of gun and ancillaries

of around 100 m/s is required although the gun is capable of delivering velocities of up to 200 m/s.

The desirable characteristics of a gas gun are ease of loading and firing and economy in the usage of compressed air. A comprehensive literature survey was carried out on the subject but no suitable designs were found. The following design by the author and Mr. A.W. Miles was finally used (23).

The gas gun incorporates a snap action pneumatic valve the function of which is to provide rapid admission of compressed air from the driver chamber to the barrel for propulsion of the projectile and a rapid closure to prevent excessive loss of pressure in the driver, once the projectile has been expelled from the barrel. A schematic of the valve assembly is shown in Fig. A 2. The valve is actuated by compressed air from a secondary pressure reservoir, the pressure of which acts on the valve actuating piston in opposition to the driver chamber pressure to ensure valve closure. A three-way solenoid valve coupled into the valve pressurizing line is used to either admit pressure to the valve chamber for valve closure, or to vent the pressure in the valve chamber to effect rapid opening of the piston-valve. The solenoid valve is operated by a monostable circuit which de-energises the solenoid valve, to pressurise the valve chamber, after a pre-selected delay.

The delay of the monostable can be selected to coincide with the time of passage of the projectile through the barrel, thereby reducing the pressure loss in the driver chamber and minimising the make-up pressure required to restore the chamber pressure.

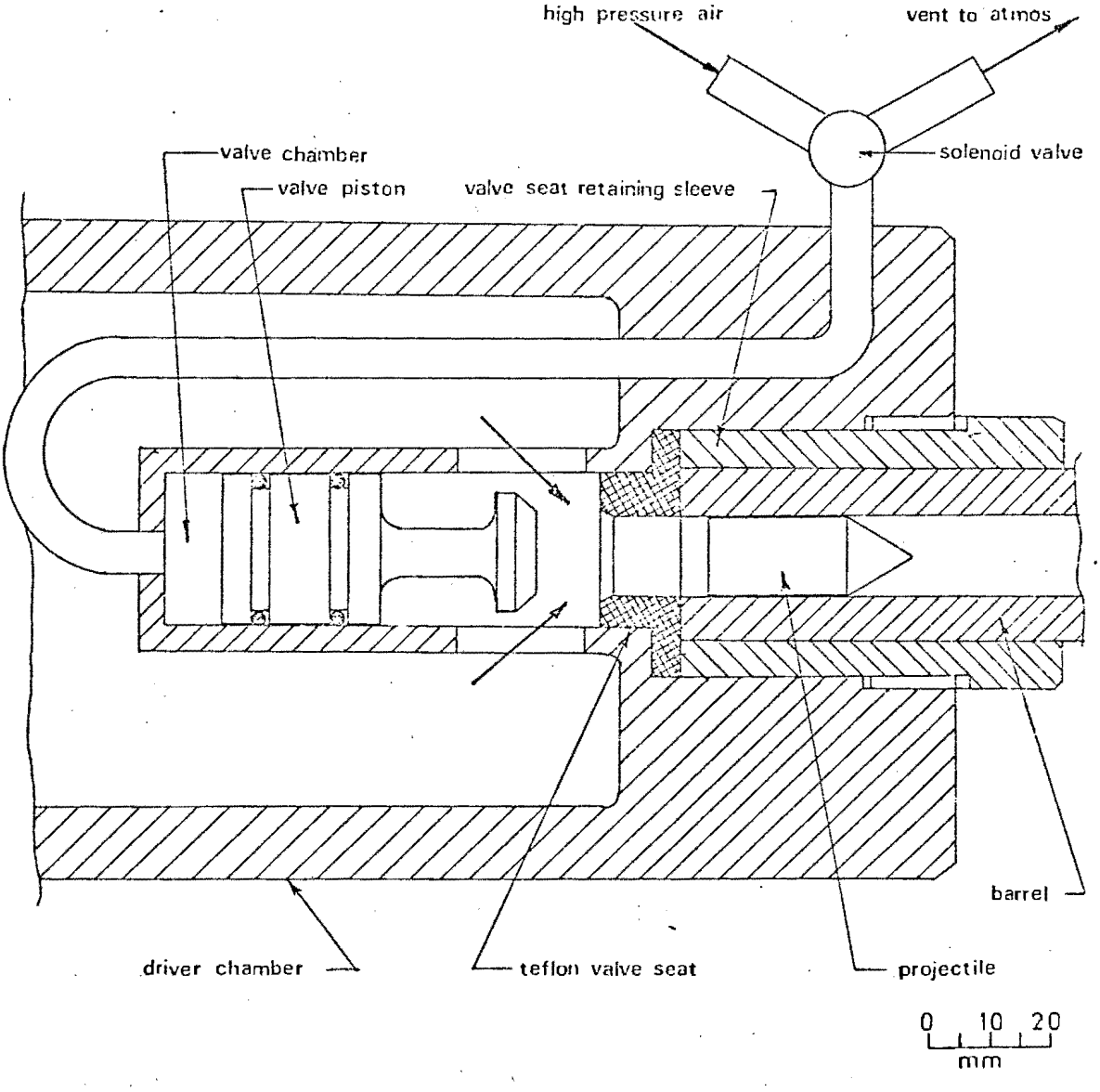

Fig. A 2 Schematic of gun valve

The valve head, stem and actuating piston are made from aluminium to reduce the mass of the working parts of the valve and so minimise the inertia effects on the valve opening and closing times. To ensure rapid venting and pressurising of the valve chamber, the chamber volume is small and the length of the pressurising line between the chamber and the solenoid valve is as short as possible. A solenoid valve with a large orifice size is used to ensure that rapid venting and pressurising can be achieved even when the solenoid valve is only partially open. The valve seat is made from "Teflon" and can easily be replaced.

Both the driver chamber and secondary pressure reservoir are connected via pressure regulating valves to a compressed air bottle so that manual pressure make up adjustments between shots are obviated.

A.3 TARGET CLAMP

To permit cross checking of results with other experiments in the field, a standard method of clamping is adopted. The present design is similar to that used by Goldsmith (12).

The arrangement consists of two steel rings 190 mm in diameter (internally) between which the target is clamped

by means of eight 8 mm Allen screws. One of the rings is threaded to enable the arrangement to be screwed onto the holder which slides along the test bed. This layout is very rigid and setting up of the target and removal is rapid.

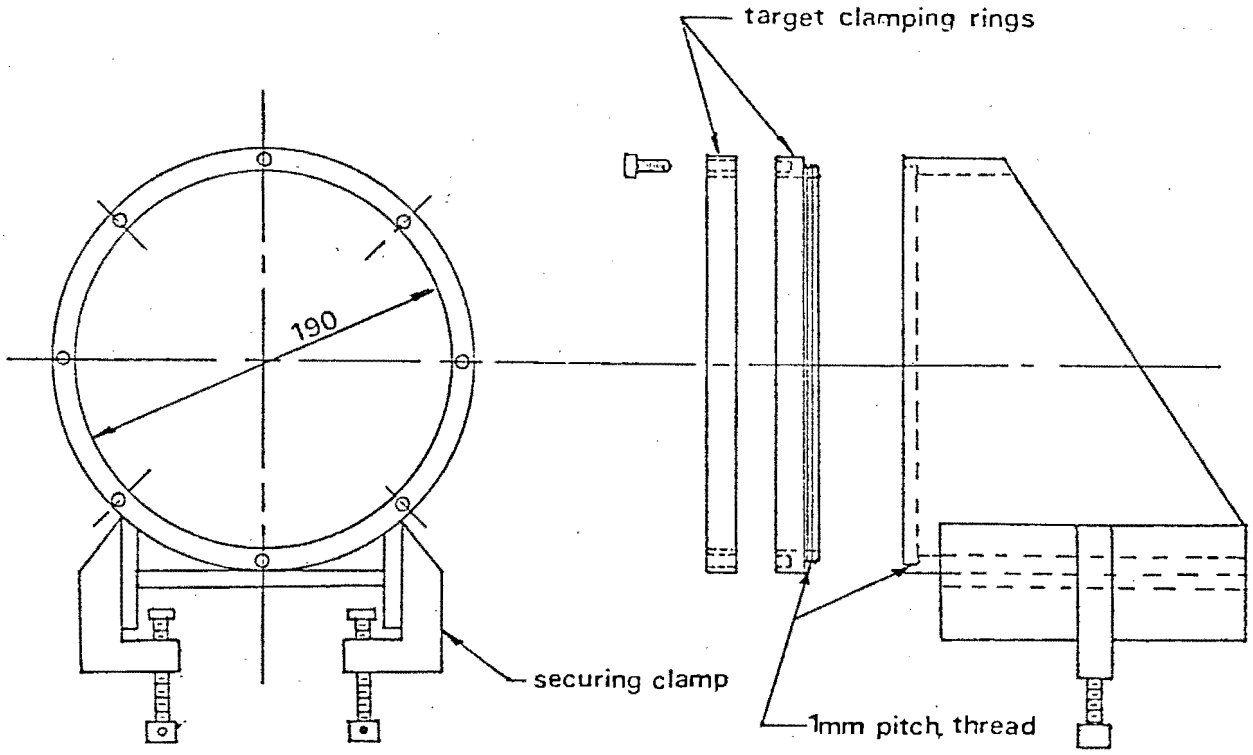

Fig. A 3 Target clamp

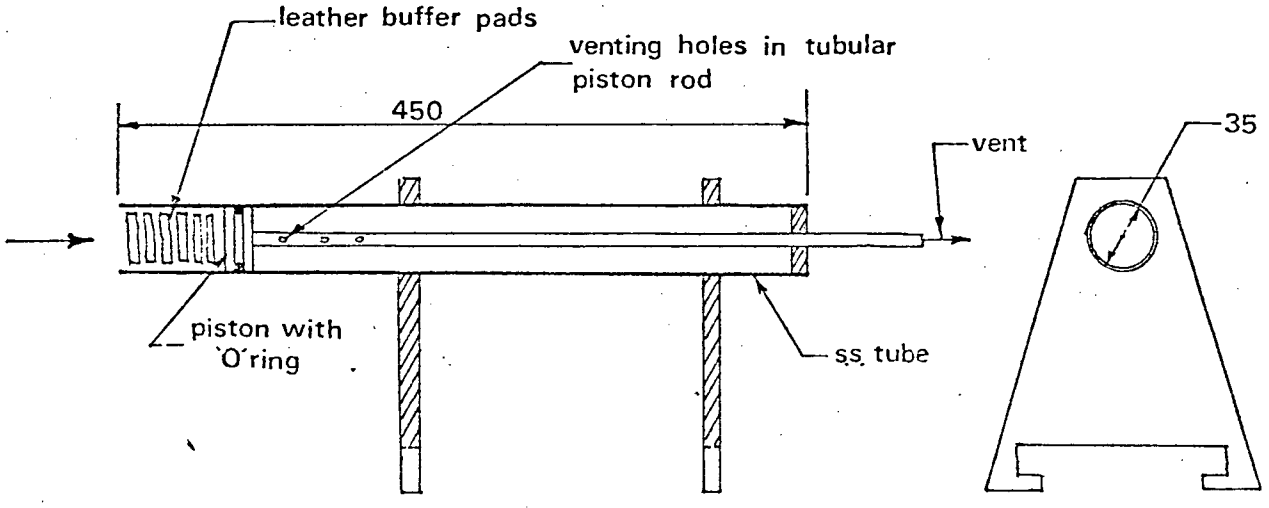

Fig. A 4 Projectile catcher

A.4 PROJECTILE CATCHER

For free flight shots when no target is placed in the projectile's path, and when perforations are being

studied, it is necessary to absorb the projectile's residual energy. The pneumatic projectile catcher shown in Fig. A 4 is used for this purpose. Air trapped behind the piston is allowed to bleed to atmosphere through an adjustable vent. This adjustment allows the resistance of the catcher to be varied. The leather pads serve to soften the impact with the catcher piston and to hold the projectile and thus prevent rebound.

A.5 MONOSTABLE CIRCUIT

The monostable provides a pulse for a pre-determined length of time. This pulse is fed to the gate of a triac which controls the A.C. supply to the solenoid valve. In its normal state the high pressure air supply is directed via the solenoid valve to effect the closure of the gun valve. On depressing the trigger switch the pulse from the monostable switches the solenoid valve to vent the valve closing pressure to atmosphere. After the predetermined time the monostable reverts to its initial state, the solenoid is switched off and the high pressure air re-admitted to effect closure of the gun valve. An additional switch sw 2 is placed in the solenoid circuit as a safety measure to isolate the latter as a precaution against random triggering due to electrical noise.

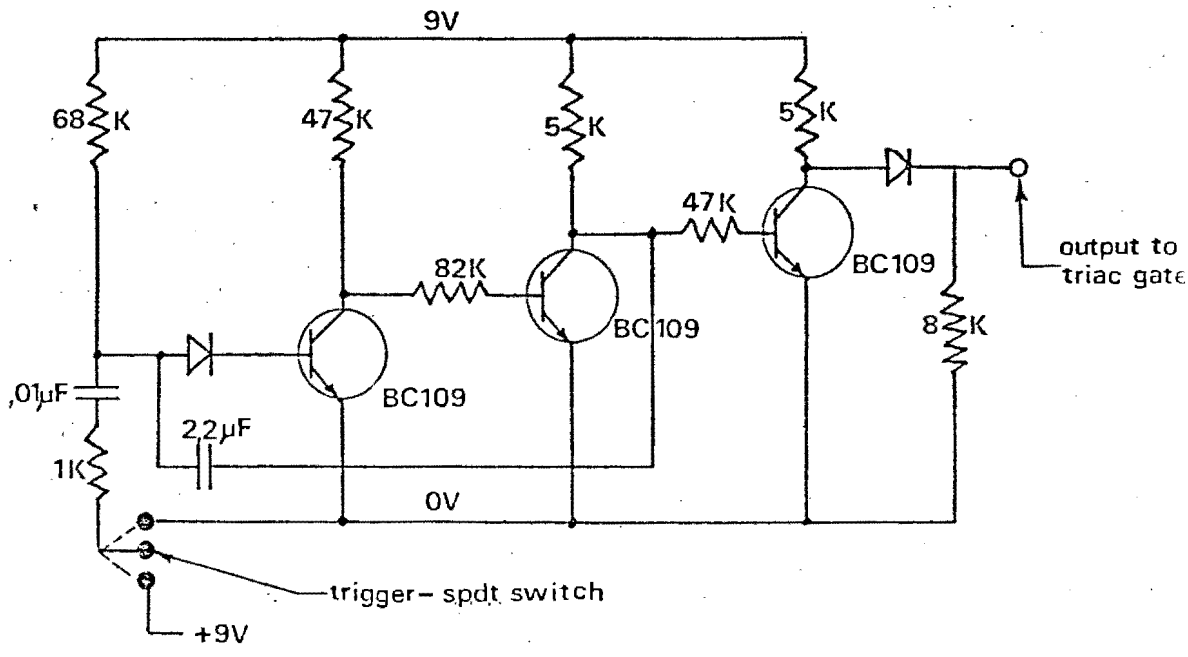

Fig. A 5 Monostable circuit

A.6 GUN PERFORMANCE

For a gun barrel length of L metres and a constant drive pressure of P pascals, the velocity V attained by a projectile of mass M kg, cross sectional area A m^2, on leaving the barrel can be calculated from energy considerations, viz:

$$PAL = \frac{1}{2} MV_o^2$$

or $$V_o = \sqrt{\frac{2PAL}{M}}$$

For an actual gun however there will be deviations

from this ideal behaviour due mainly to friction and windage losses experienced by the projectile and the fact that the driver pressure P is not constant but falls as the projectile moves down the barrel. Since the valve has a finite opening and closing time, the assumed square pulse shape of the pressure pulse will also be ideal - the actual shape having a finite rise and fall time. These deviations all act in a way to reduce the ideal muzzle velocity. This is exactly the trend that was found in practice. The results are shown in Graph A 6.

Graph A 6

Calibration of gas gun

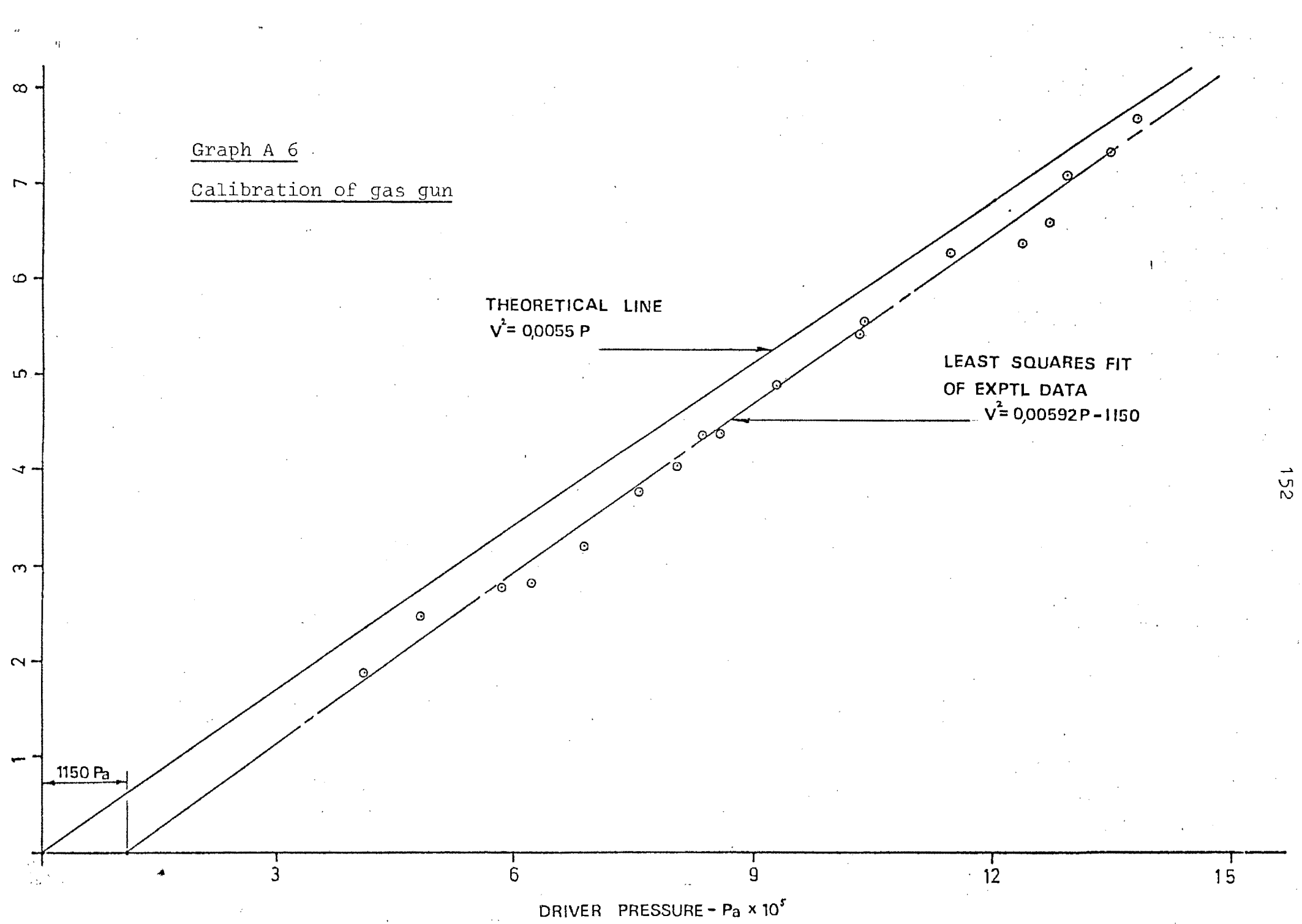

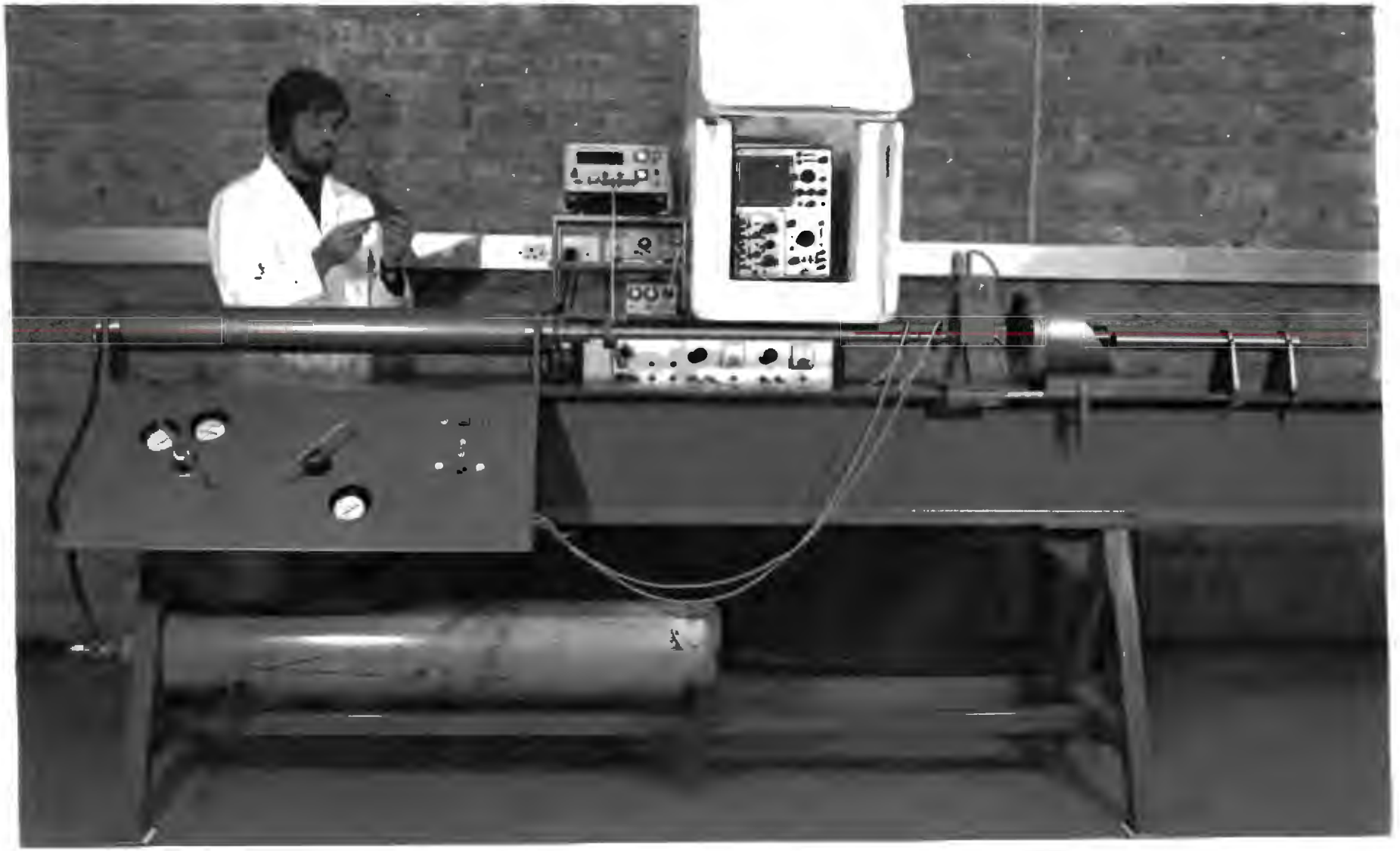

Photo A.1 A general view of the gas gun and penetration monitoring apparatus. Note the oscilloscope's accoustic shielding to prevent radio-phonic interference.

Photo A.2 The target mounting and projectile catcher

Photo A.3 The breach of the gas gun showing the triggering solenoid

APPENDIX B

PROCESSING ELECTRONICS

The processing electronics can be summarised as follows:

(1) Differentiator

(2) Integrator

(3) Triggering and co-ordinating circuitry

B.1 DIFFERENTIATOR

An ideal electronic differentiator should sense the slope of an input signal (which is varying in time) and produce an output voltage proportional to it. The circuit shown in Fig. B 1 which uses a high speed operational amplifier (LM 318H) will approximate this.

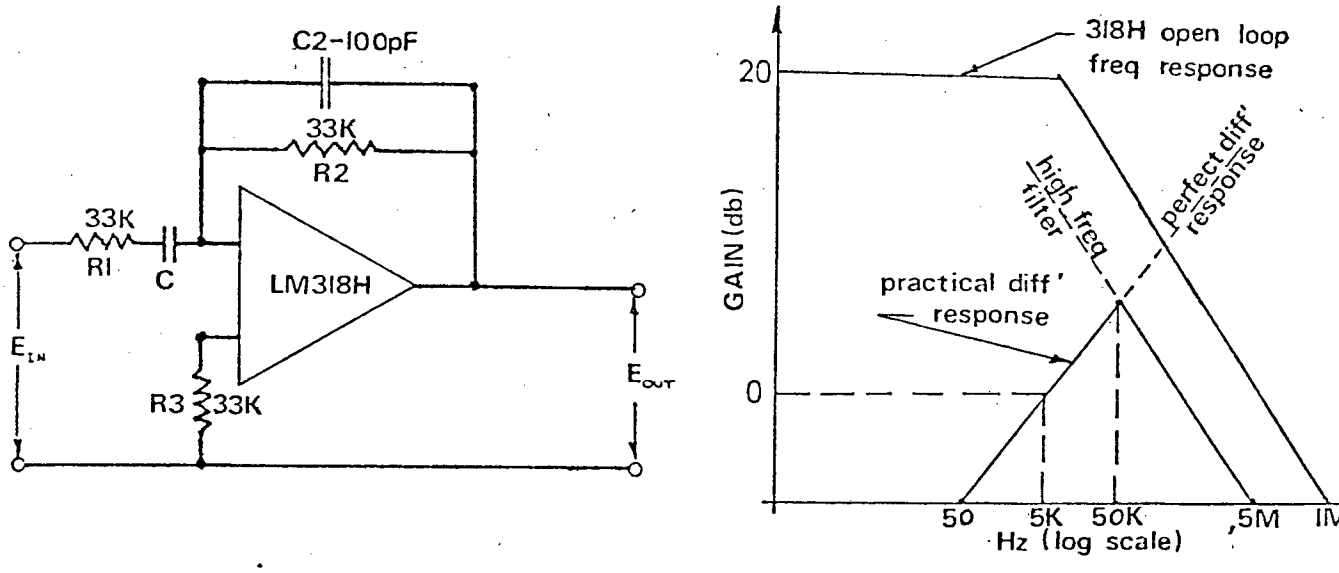

Fig. B 1 Differentiator

In practice, a perfect differentiator is undesirable since any input will contain a degree of noise and the differentiator will sense the sharp slope of the noise and produce a corresponding output which will distort the main signal or even swamp it. The circuit shown in Fig. B 1 has a built-in break point so that for input signals above f_h = 20 kHz the operational amplifier will in conjunction with C_2 , act as an integrator and thereby filter out the effects of noise. F_h was chosen as a compromise between the actual requirements and the frequency limitations of the special high-speed operational amplifier. The actual response of the differentiator is presented in Graph B 5.

B.2 INTEGRATOR

The function of an electronic integrator is to sum an input voltage e_{in} in the domain over a given period of time, and provide an output voltage e_{out} proportional to the instantaneous value of the sum. By its very nature, the integrator is a more stable device than a differentiator and if noise is present in the input singal, it is automatically filtered by the integrating process.

The main problem encountered with integrators is the fact that definite limits must be set to the integrating process. In the present system, limits LT 1 and LT 2 (see

Fig. 5.16) are set by means of the adjustable time delays T 2 and T 3. The output from T 3 is a 9 V pulse of T 3 seconds durations corresponding to the period over which the integration will be carried out.

The inverting and switching circuit (see Fig. B 2) is controlled by the pulse from T 3. The output from the inverter is normally at + 9 V potential and for the duration of the pulse T 3, the output falls to - 9 V. This output is connected to the gate of the field effect transistors (F.E.T's) in the feedback loop of the integrator. These F.E.T.'s are used as switching devices to either ground the output of the integrator, or allow it to operate.

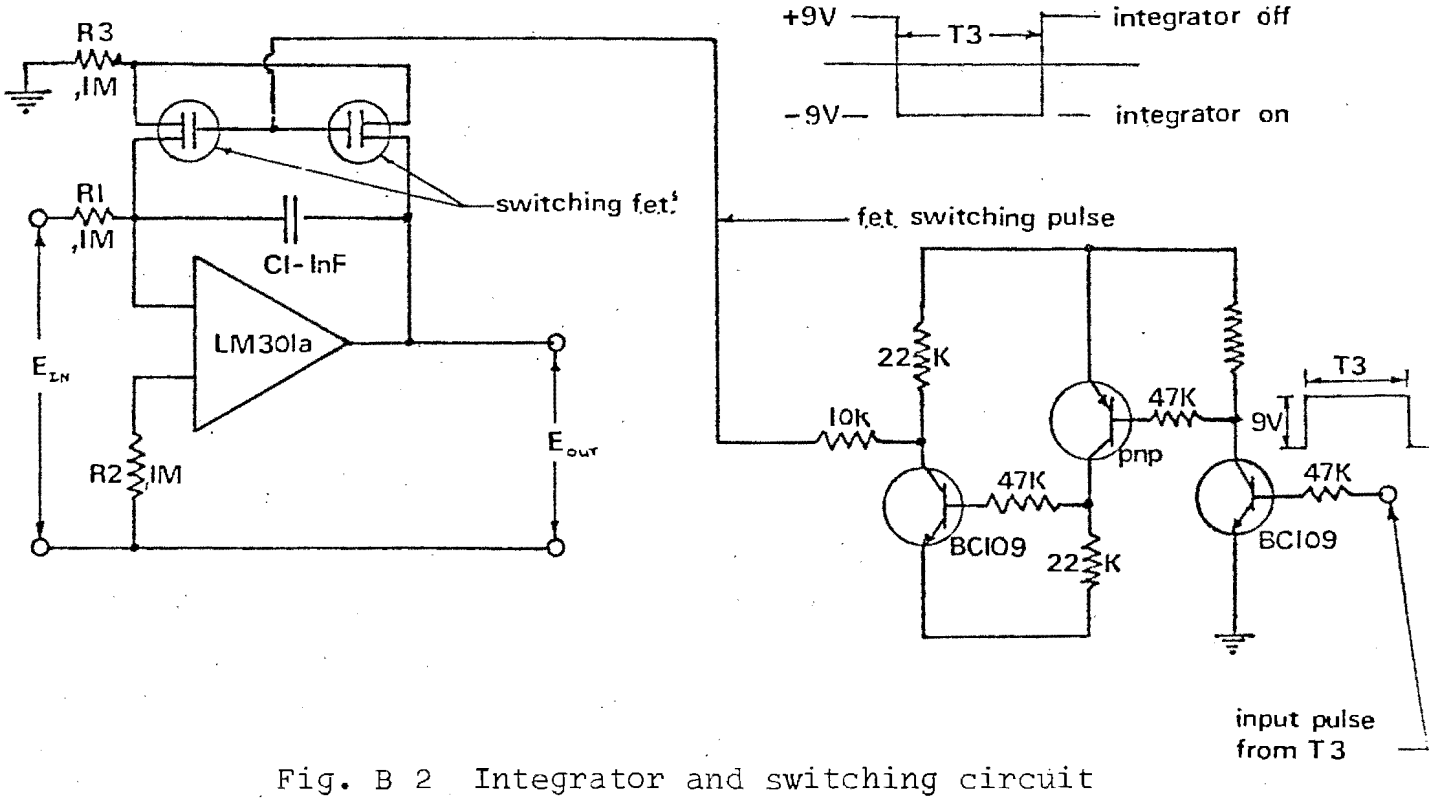

Fig. B 2 Integrator and switching circuit

B.3 TRIGGERING AND CO-ORDINATING CIRCUITRY

To co-ordinate the integrator and the recording oscilloscope with the impact of the projectile, the following circuitry is necessary.

B.3.1 PHOTO TRIGGER

The circuit for this device is shown in Fig. B 3. A light beam situated in the pickup section next to the scratch pickups falls onto the base of a photo-transistor and effectively holds the output terminal at ground potential. When the projectile breaks the light beam, an output pulse of about 18 V is generated. This pulse marks the projectile's motion in time and space.

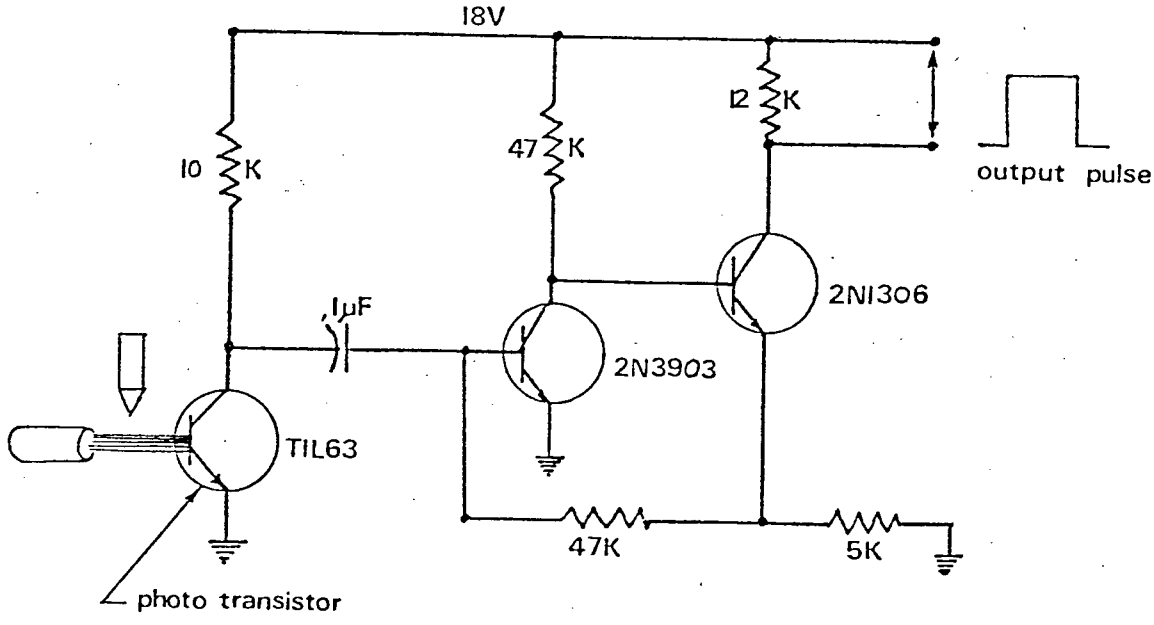

Fig. B 3 Photo pulse generator

B.3.2 SEQUENCING CIRCUITRY

With an initial pulse to give a reference point, co-ordination of the electronics with the impact is accomplished by a series of delay circuits which are started by the initial pulse. The pulsing sequence is explained in Fig. 5.16.

The delay circuits T 1, T 2, T 3 are all built around the signetic SE 555 integrated circuit. The desired time delay is set by means of the capacitor C and resistance R. (See Fig. B 4). According to the relationship:

$$T = RC$$

All the delays are adjustable by means of a variable resistance. To given an even greater range of delays, T 1 also has a selection of capacitors to vary.

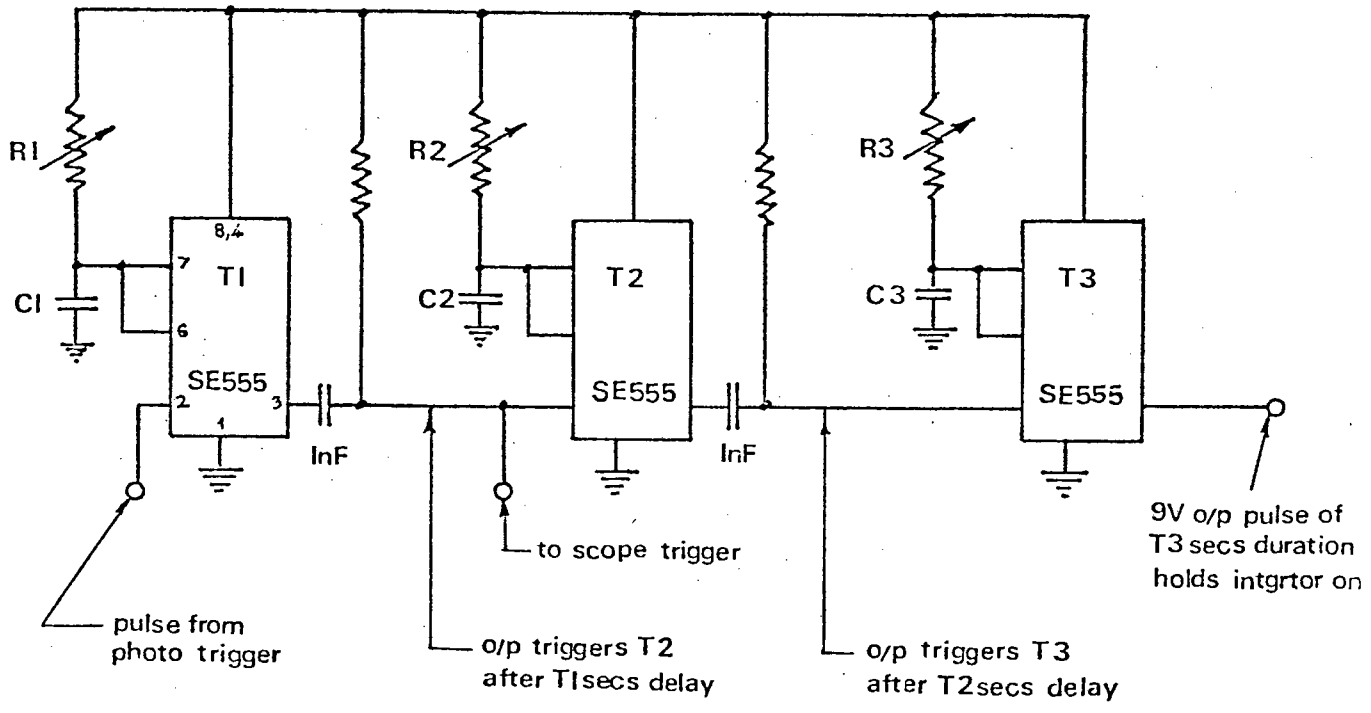

Fig. B 4 Delay circuitry

The delay times used are:

T1 from 5μs to 5000μs

T2 from 100μs to 300μs

T3 from 200μs to 1500μs

B.4.1 CALIBRATION OF DIFFERENTIATOR

The ideal differentiating process can be represented as:

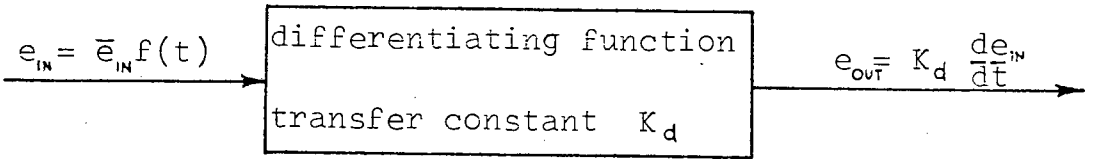

In practice an electronic differentiator will have a transfer function K_d which depends on the components used (see Fig. B 1). This can be calculated from

$$K_d = RC$$

Instead of relying on an absolute determination of K_d from a knowledge of the exact values of the resistance and capacitance used, the constant was determined experimentally.

Using a sine wave generator as the input singal, the differentiator was tested over a range of frequencies.

If the input to the differentiator is:

$$e_{IN} = \bar{e}_{IN} \sin\omega t$$

Then ideally, $e_{out} = \omega \bar{e}_{IN} \cos\omega t$.

Since in practice $e_{out} = K_d \frac{de_{IN}}{dt}$

We get $K_d = \frac{\bar{e}_{out}}{\omega \bar{e}_{IN}} = 3{,}45 \times 10^{-5}$ for the differentiator used.

Thus for each input frequency K_d can be calculated from a knowledge of the amplitudes $\bar{e}_{in}$ and $\bar{e}_{out}$ and the circular frequency ω. Ideally the phase shift between the input and output signals should be 90°. In practice this is approximated only, the approximation deteriorating towards the designed breakpoint of the circuit when the phase shift approaches 180°. The results of the calibration are presented graphically in Graph B 5.

B.4.2 CALIBRATION OF INTEGRATOR

The same procedure was adopted for the integrator as was used for the differentiator.

In this case we have:

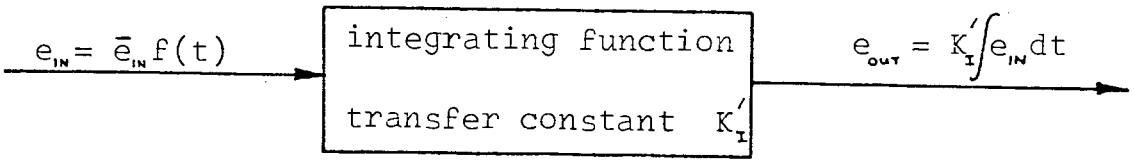

Theoretically $K_I' = \frac{1}{RC}$ (see Fig. B 2). A calibration was carried out using the sine wave generator as the input signal, and using the same reasoning as for the differentiator we get:

$$K_I' = \frac{\omega \bar{e}_{out}}{\bar{e}_{in}} = 8{,}18 \times 10^3$$ for the integrator used.

The results are presented graphically in Graph B 5.

Graph B 5

Frequency response of integrator and differentiator

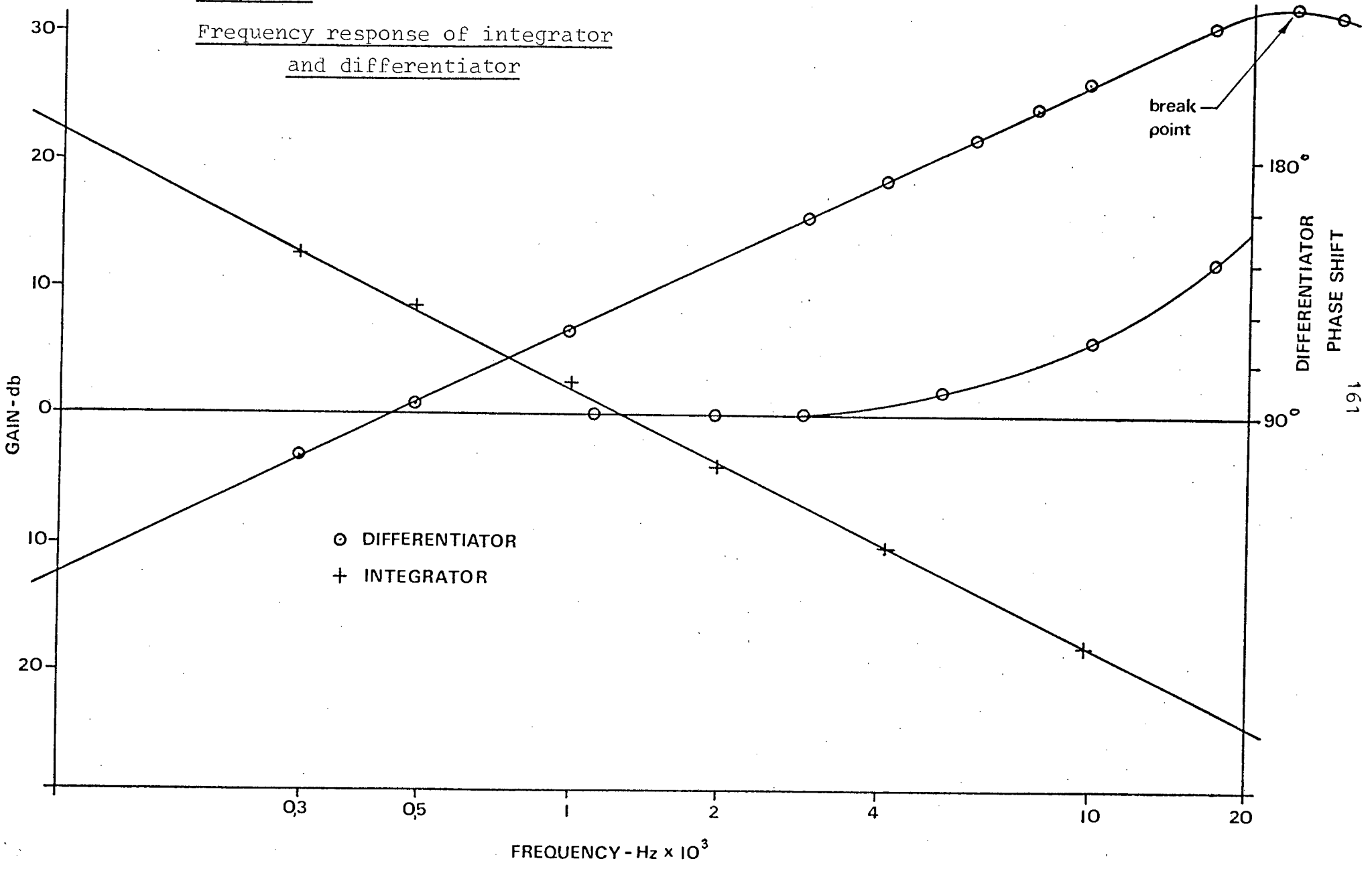

APPENDIX C

TRANSDUCER CHARACTERISTICS

C.1 THE PROJECTILE TRANSDUCER

An ideal projectile transducer should generate an output voltage, which is directly proportional to the particle motion in the projectile, at the sensor location. In practice, distortion of this signal can be due to:

(a) the processing electronics

(b) commutator inefficiency

(c) ineffective magnetic shielding of the passive arm in the projectile measuring coil.

The processing electronics discussed in Appendix B have been designed with frequency responses far in excess of that required by the projectile transducer signal. This source of distortion will therefore be negligibly small.

The scratch pickup concept however, is open to several disturbances. Firstly, the relative motion between the aluminium commutator and high speed steel brush, generates heat and the contact of two dissimilar metals at an elevated temperature will produce Seebeck and Peltier e.m.f.[5] Fortu-

nately, however, the pickup contains two such thermocouples in opposition (see Fig. C.1) so the overall effect should be zero.

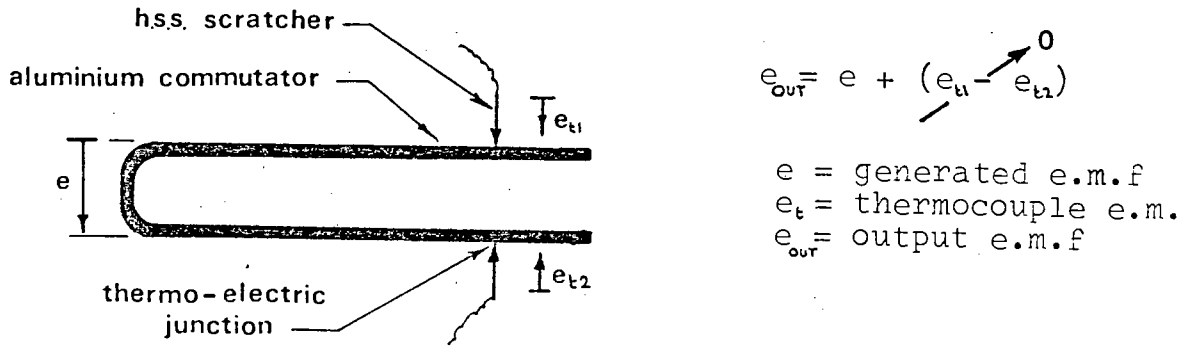

Fig. C.1 Thermocouple disturbance

Distortion of the signal at the scratch pickup-commutator junction could also be caused by a change in the effective electrical resistance at this point. As the oscilloscope and integrated circuits draw only about one microamp of current from the projectile's generating coil, the scratch pickup can vary from its normal fraction of an ohm resistance to 10 000 ohms before a 1% fluctuation will be noticed in a 1 V signal. This is not too demanding on the pickups.

The last possible signal distortion is that due to ineffective magnetic shielding of the passive arm in the projectile sensing coil. The effectiveness of the shield

currently in use is clearly shown in the photos C.1 and C.2. These velocity-time records were made for a projectile in free flight and should theoretically be perfectly horizontal. With no magnetic shield in place, the passive arm of the sensor coil will be passing through an ever decreasing magnetic field and this accounts for the voltage rise in photo C.1. With the shield in place, the improvement in linearity is marked. The slight drop in voltage in this case, is thought to be due to the small mechanical resistances produced by the scratch pickup.

The linear range of the transducer was conveniently found by cutting notches in a commutator bar, which results in a break being produced in the oscilloscope trace. Two such breaks are clearly shown in photos C.1 and C.2.

This method of marking the velocity-time trace was considered as a way of determining the projectile approach velocity. If the notches are placed near the front of the commutator a known distance apart, the breaks in the initial part of the velocity-time trace, before the projectile impacts the target, will give a measure of the projectile's velocity. To attain any accuracy however, the method was found to use up too much of the projectile's linear range, and to restrict the traces to the right hand side of the oscilloscope screen.

Because of these limitations the method described in Sect. 5.2.4 was adopted instead.

C.2 THE TARGET TRANSDUCERS

C.2.1 THE INNER ZONE RADIAL EXPANSION TRANSDUCER

As this transducer operates on a digital rather than analogue principle its transfer function is of secondary importance. The only requirement of the transducer is to accurately locate the switching points of the projectile head segments in the time domain.

Since all components in the circuit are passive, switching times are extremely fast and limited only by the slew rate of the oscilloscope. Generally, the time intervals between segments can be measured with an error of less than 1%.

C.2.2 THE OUTER ZONE TRANSVERSE MOTION TRANSDUCER

Although this transducer operates on the same principle as the projectile transducer, its only source of signal distortion is through its pre-amplifier.

This amplifier is based on the LM 318 H integrated circuit used for the integrator and differentiator and has a frequency response far in excess of that required by the transducer signal. Distortion is therefore negligibly small.

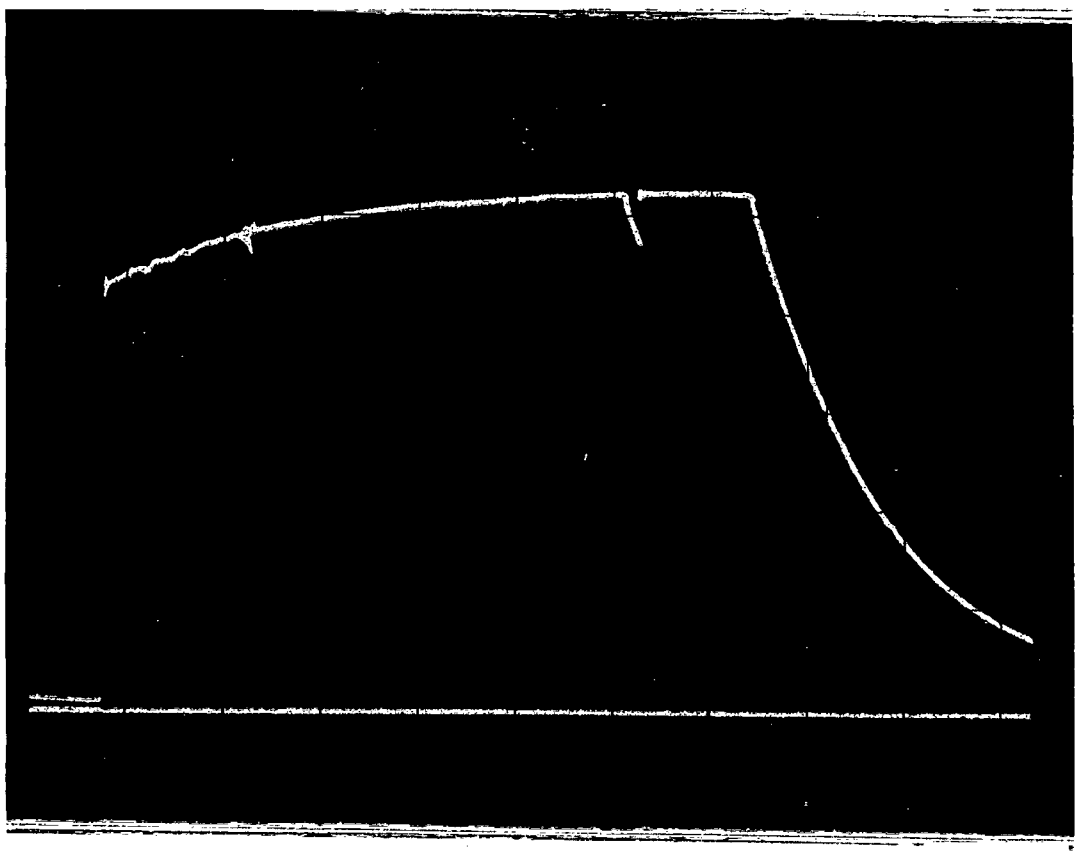

Photo C.1 Free velocity trace without magnetic shield

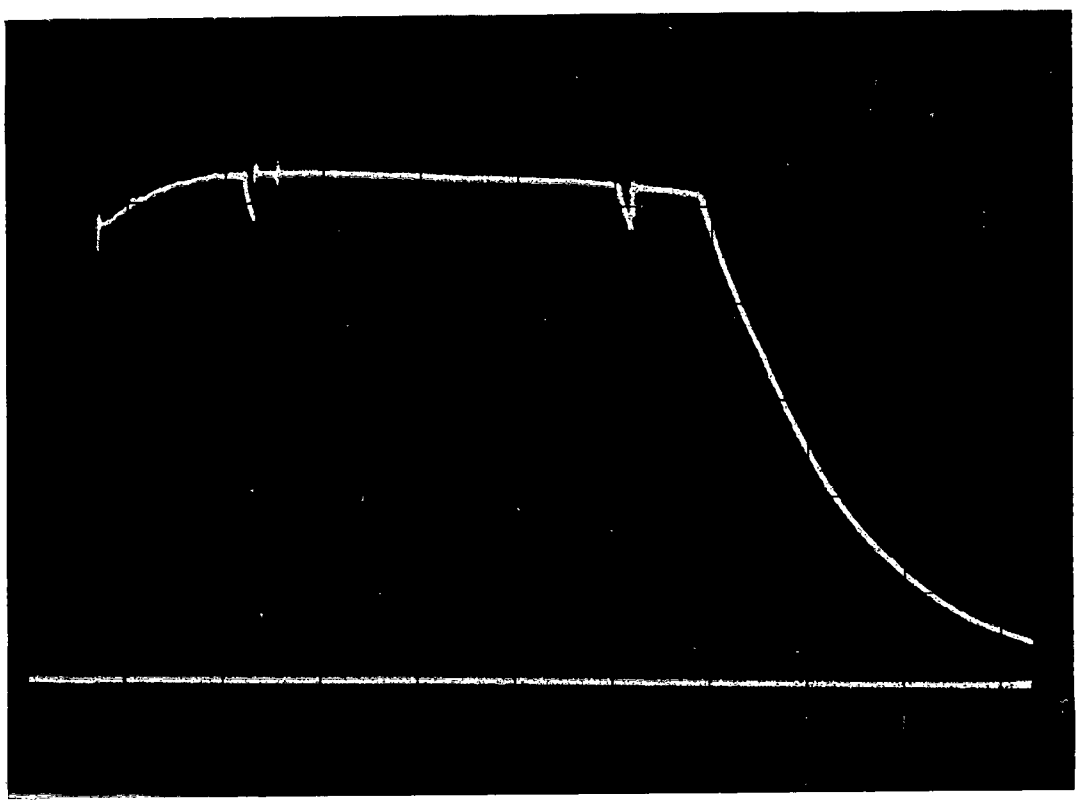

Photo C.2 Free velocity trace with magnetic shield

APPENDIX D

DATA PROCESSING

D.1 PROJECTILE DATA

In conjunction with equation 4.6 two simpifying assumptions are used in the actual data reduction. Firstly, the limits of the integration were initially calculated as shown in Fig. D.1 for an equivalent uniform projectile made of Nylatron. After studying several traces however, it was discovered that the frequency of the projectile vibration was not constant and changed throughout the penetration. Computed values of the natural period agree with the experimentally found value to within 10% and a mean value of the experimental value was used in subsequent data reduction.

The second simplifying assumption made was to assume the term

$$W_{cm}(t - 2d/c) \simeq W_{cm}(t)$$

This is a fair assumption since d is small. The resulting relation becomes:

$$W_{cm}(t) = \frac{c}{2l} \int_{t-(l+d)/c}^{t+(l-d)/c} W(d,t)\, dt \qquad \text{D.1}$$

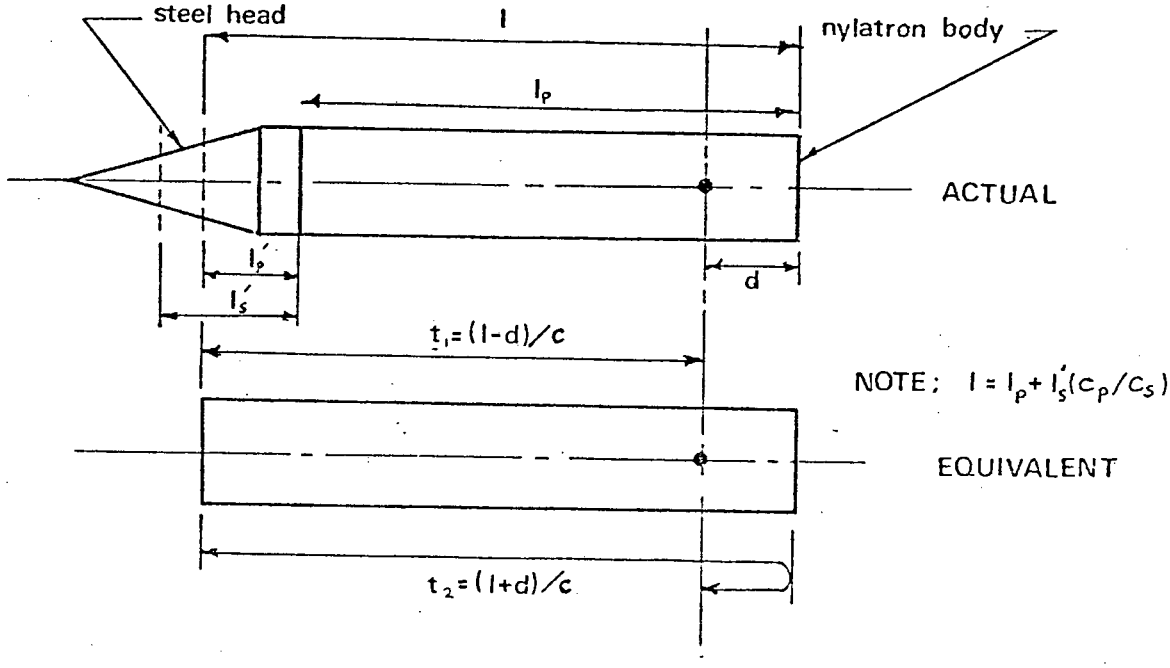

Fig. D.1 The Equivalent Isotropic Projectile

The mechanism of equation D.1 is clearly shown in Fig. D.2. To compute the ordinate $\ddot{X}_{cm}(t)$ at a time t, the area A under the deceleration-time trace is computed between the limits $t + (l - d)/c$ and $t-(l + d)/c$. This value is then divided by the mean period time of the projectile's natural vibration ($c/2l$) to give the mean ordinate $\ddot{X}_{cm}(t)$.

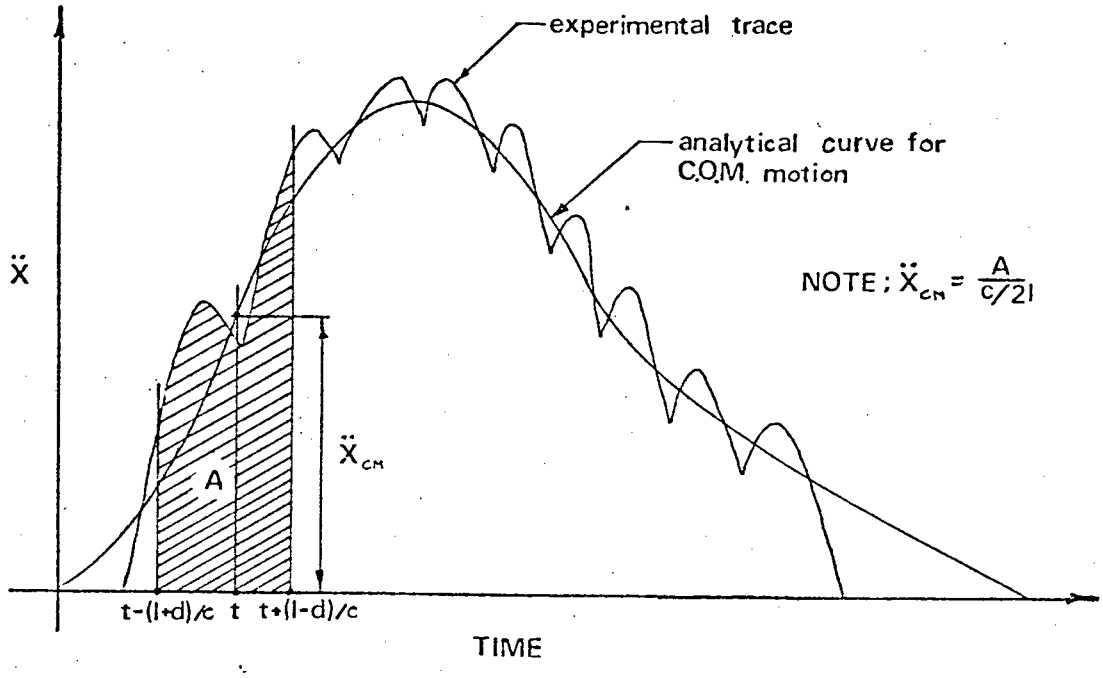

Fig. D.2 Mechanism of analysis

About 60 data points measured from a 35 mm photographic negative of the deceleration-time trace was used as input data for a computer programme. The flow chart for the latter is shown in Fig. D.3, and a sample of the computer graphic output is shown in Fig. D.4.

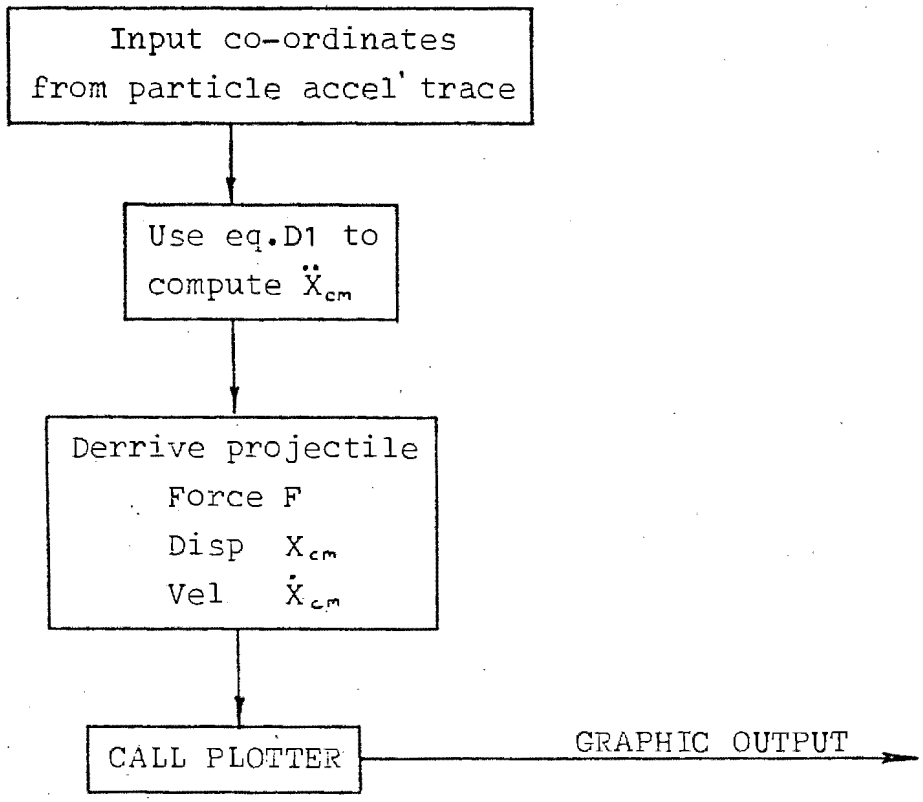

Fig. D3 Flow diagram used to process projectile exptl data

D.2 TARGET DATA

Data obtained from the two target transducers is directly related to the monitored motions and no processing as such is required. To obtain displacement data from the outer zone velocity transducer it is necessary to integrate the primary data once. This has been done numerically.

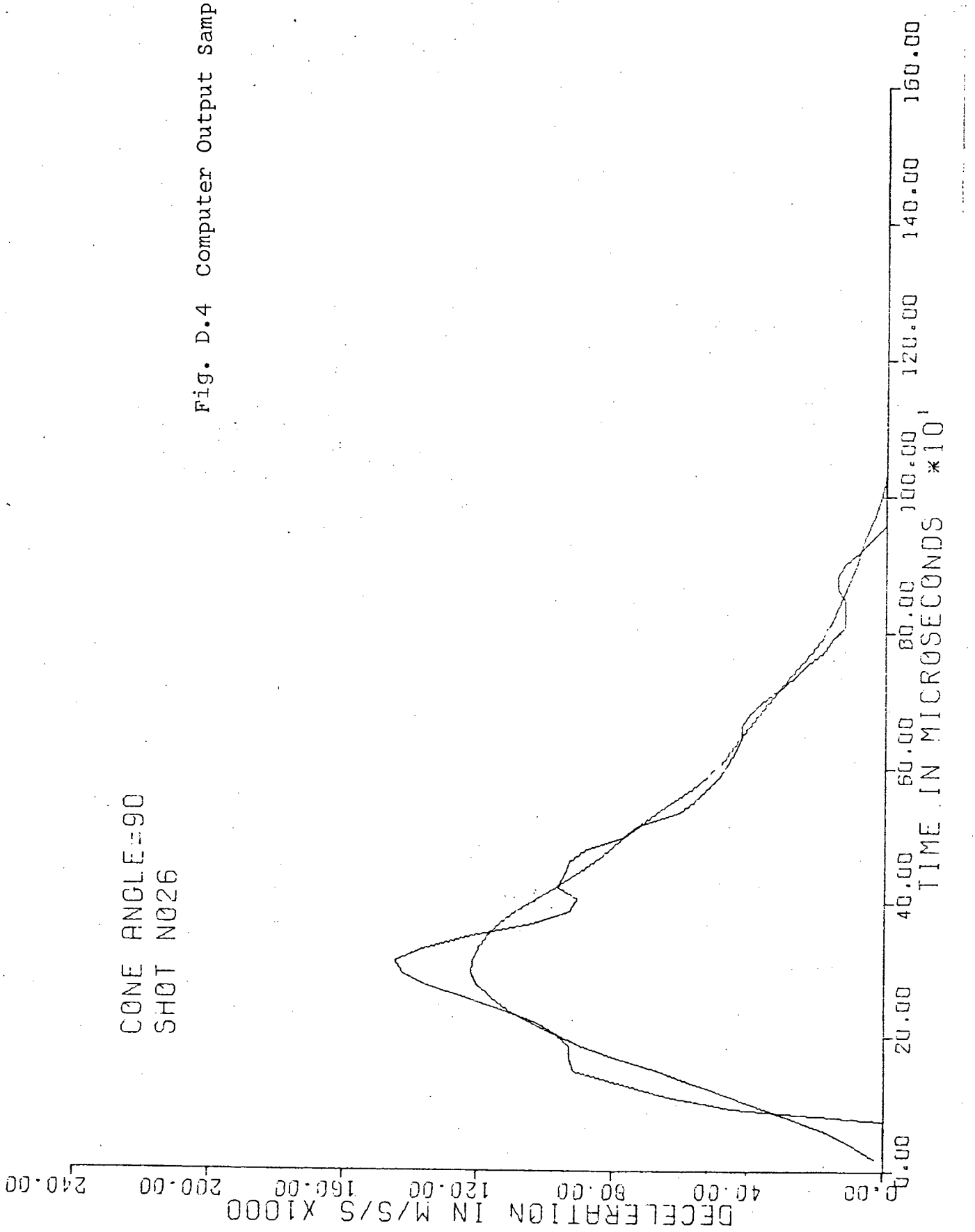

Fig. D.4 Computer Output Sample

NOMENCLATURE

E	energy
E_{Iz}	inner zone energy
E_{oz}	outer zone energy
D	projectile diameter
l	projectile length
L	projectile cone height
d	sensor distance from projectile tail
X	projectile rigid body displacement
u	projectile particle displacement
x	co-ord measured from projectile tail
V_o	projectile striking velocity
V_f	projectile post-penetration velocity
V^*	unspecified intermediate velocity
U	Laplace transform of u
U^*	dummy variable
W	dummy variable
H	undeformed target plate thickness
T	deformed target plate thickness
R	outer limit of plastic deformation
r_o	radial location of inner-outer zone boundary
r_o^*	inner-outer zone boundary radius at which indentation transforms to conic deformation or petalling
r	radial co-ordinate
S	inner zone location parameter measured from the petal tip
S'	radial location corresponding to S
Y	tensile yield stress of target
	target mass density
C_p	plastic deformation wave velocity

M_r	radial bending moment in target
M_t	tangential bending moment in target
M_o	plastic moment of target
P_o	static punching force of target
N_r	membrane force
F	instantaneous penetration force
F^*	maximum value of the penetration force
X_I	indentation transverse displacement
X_I^*	indentation-conic deformation transformation displacement
X_c	transverse displacement due to conic deformation
X_r	inner zone transverse displacement during petalling
X_s	transverse shear separation displacement
X_ϕ	transverse displacement during the terminal phase of petalling
X_d	outer zone transverse displacement
X_{do}	outer zone transverse displacement at the inner-outer zone boundary
C	constant
K_A	slope of empirical 'A' function
K_I	indentation constant
K_p	petalling constant
A	area
e_{IN}	input voltage
e_{out}	output voltage
B	magnetic field intensity
t	time
K_V	projectile transducer transfer constant
K_d	differentiator transfer constant
K_I'	integrator transfer constant

θ	angle between deformed and undeformed target
θ_o	value of θ at the in-out zone boundary
α	projectile semi-cone angle
μ	coefficient of friction
λ	complex variable
ϵ	membrane strain in the generator direction
ϵ_H	membrane hoop strain
ϵ_N	membrane, normal or thickness strain
σ	membrane stress in the generator direction

σ_p	interfacial compressive stress
σ_p^*	the mean pressure of resistance of the target
σ_s	shear stress
σ_s^*	target shear stress at which inner zone separation occurs
ϕ	petal rotation in terminal petalling
ω	circular frequency